Imperial College London

The Ultra-Wideband Pulse

Samuel Benjamin Philip Radnor

February 18, 2008

Thesis submitted in partial fulfilment of the requirements for the degree of

Doctor of Philosophy of

Imperial College London

Quantum Optics and Laser Science Group

Blackett Laboratory

Imperial College London

Prince Consort Road

London SW7 2BW

United Kingdom

I declare that the work contained within this Thesis is my own unless stated otherwise in the text.

Samuel Benjamin Philip Radnor

Diamonds only glitter in the light...

Abstract

Since the birth of mode-locking the temporal duration of optical pulses has radically diminished. In parallel to this, bandwidths have grown so large that almost entire frequency octaves are present in today's few-cycle pulses.

This thesis investigates the character of ultra-wideband pulses in nonlinear environments. Because of the growth in optical bandwidths, traditional definitions and propagation models break down, requiring newer more accurate numerical techniques. A novel approach capturing the uni-directionality of pulses is presented in the form of *G-variables* by combining the electric and magnetic field descriptions. These *G-variables* have the advantage of both an accurate spectral representation and a reduced computational overhead, making them significantly more efficient than existing direct Maxwell solvers. Such approaches are particularly important where large propagation distances and/or transverse dimensions are concerned.

Pseudo-spectral techniques play a key role in the success of these wideband models enabling sub-cycle dynamics to be studied. One such phenomenon is Carrier Wave Shocking (CWS), where the optical carrier undergoes self-steepening in the presence of third-order nonlinearity. This process is carefully studied, focussing on the effect of dispersion and the feasibility of its physical realisation. The process is then generalised to arbitrary nonlinear order, where the quadratic form finds potential applications in High Harmonic Generation (HHG). Shock detection schemes are also developed, and agree with analytical solutions in the dispersionless regime.

To fully characterise few-cycle pulses, the absolute Carrier Envelope Phase (CEP) must be known. A novel $0-f$ self-referencing scheme relying on wideband interference is investigated. By applying robust frequency domain definitions a proposal is made to convert this scheme into one that determines absolute CEP. The scheme maps the level of spectral interference to absolute CEP using numerical simulations.

Acknowledgements

I would like to start by expressing my sincerest thanks to Professor Geoff New for his ongoing support, guidance and assistance throughout this Ph.D. From my very first day, beginning on Level 8 of Blackett until now, he has always had some positive and encouraging words to say. This attitude has certainly kept me going through many a difficult day, especially when one of my illusive 'bugs' could not be found.

Secondly, I would like to thank Dr Paul Kinsler for his constant effort and much needed advice. Were it not for his time and patience, I would not be in this position today. He has had a profound influence on my research over the past three years.

Of the *big four*, I am also indebted to John and Luke for much of their day to day help. John helped me to find my feet during the first year, and Luke has taught me vast amounts ever since taking over John's old desk, significantly contributing to many of my research ideas. I owe all of you months of your time, and can only re-iterate how grateful I am.

Other former group members who I wish to acknowledge are Harris, Jesus and Lucien. They were fortunate enough to leave before I started asking too many questions. I also wish to thank Ara, Shash and Mark for some insightful chats in the union and beyond.

I would like to thank my coffee colleagues too; Rachele, Thomas, Jo, Bosanta, David, Natty and Chris. The latest member of 6M07, 'Little Firenze' must also be added to this list, though his arrival was late, his contribution has been crucial over the last few months. Dr Bates deserves a special mention as we started as coffee colleagues and ended up mates.

Much praise must be given to my fiancee Esther for putting up with the constant drone of my thesis. Thanks also, to my flatmate Matt for enduring a messy flat over the write-up period (not that it was ever tidy before). There are also many other people who I wish to extend a more indirect thanks to.

Finally, I wish to thank my family for their love and support over the years and for always encouraging me to walk on my own path.

Thanks!

Publications

- S. B. P. Radnor, P. Kinsler and G. H. C. New, **Proposal for absolute CEP measurement using 0-to-f self-referencing**, *In preparation* (2008)
- S. B. P. Radnor, L. E. Chipperfield, P. Kinsler and G. H. C. New, **Carrier-wave steepened pulses and gradient-gated high-harmonic generation**, (Accepted) Phys. Rev. A, (2008)
- P. Kinsler, S. B. P. Radnor, J. C. A. Tyrrell and G. H. C. New, **Optical carrier wave shocking: Detection and dispersion**, Phys. Rev. E, **75** (2007) 066603
- P. Kinsler, S. B. P. Radnor, and G. H. C. New, **Directional Pulse Propagation**, Phys. Rev. A, **72** (2005) 063807

Contents

List of Figures

List of Tables

Chapter 1

Introduction

1.1 A brief history of the optical pulse

The history of the LASER (Light Amplification by Stimulated Emission of Radiation) is inextricably linked to the generation of coherent pulses of light. The very first laser realised by Theodore H. Maiman [1] in 1960 (Hughes Research Laboratories), was a pulsed system comprising of a helical xenon flashlamp surrounding a pink ruby rod, the polished ends of which formed a Fabry-Perot cavity. The flashlamp driving the lasing transition had a typical duration of $\simeq 500\mu$s. This system created the first ever laser pulses, which were somewhere between micro and millisecond, and of variable intensity due to relaxation oscillations. The finite temporal structure of any pulse requires a set of frequencies for its description. In other words, the first laser also gave birth to the first coherent pulse, albeit very narrowband. In fact, a millisecond pulse from a 694 nm ruby laser contains within it $\simeq 4 \times 10^{11}$ oscillations!

Rapid progress in generating shorter pulses followed with the development of Q-switching, which enabled high intensity nanosecond pulses to be produced. The technique involves reducing the quality factor or 'Q' of the laser cavity whilst pumping is taking place, causing the population inversion to reach a very high level. This large population inversion would not be possible if a high Q-value existed, as lasing would prevent the population inversion from increasing to such an extent. The Q-value is then returned to its naturally high value, prompting the emission of a giant pulse, accompanied by the abrupt depletion of the inverted population. The high intensities of these giant pulses paved the way to understanding many nonlinear optical phenomena.

Ultra-fast optics then evolved through laser mode-locking, a technique which revolutionised laser physics. In mode-locking, a multitude of axial cavity modes are forced into fixed relative phase relationships. This means that the EM field inside the cavity is

almost zero for most of the time, but for very short intervals, where constructive interference takes place, very high intensity pulses are produced [2], where almost the entire energy of the radiation field is concentrated. The cumulative interference of the cavity modes forms a pulse, and once every round trip the pulse is outcoupled from the cavity via a partially transmitting mirror. In such cases, if the energy per mode is kept constant, the pulse intensity becomes proportional to the number of modes present, whereas the pulse duration is inversely proportional to the number of modes. Because mode-locking is of such great importance to nonlinear optics, and is the only viable route to producing few-cycle pulses, its history will be discussed in slightly more detail.

1.2 Mode-locking

The seeds of active mode-locking were being sown around the year 1964. Gurs and Muller were working on ruby lasers [3, 4], while Statz and Tang were working on He-Ne systems [5]. The literature identifying mode-locking first appeared in 1964 by DeDomenico [6], Hargrove [7], Yariv [8] and Lamb [9]. It was Hargrove *et al.* who succeeded in demonstrating mode-locking for the first time, using acoustic waves to periodically change the refractive index of the active He-Ne lasing medium. The technique of directly modulating the EM field inside the cavity became known as *active* mode-locking. The periodic modulation enforces the necessary phase relationship between the axial cavity modes. Given the narrow gain bandwidth of the medium, the pulses in these systems remained in excess of a nanosecond. Even a He-Ne pulse of nanosecond duration, contains up to 250 000 carrier oscillations.

For the duration of the pulse to fall under a nanosecond, passive mode-locking would have to be developed. This was first achieved by Mocker and Collins in 1965 with a ruby laser and a saturable absorber [10]. In *passive* mode-locking, the fixed phase relationship between the cavity modes is induced by the self-action of the laser field inside the cavity, a process not externally driven. In the case of saturable dye absorbers, the dye preferentially transmits light of a higher intensity, producing a train of mode-locked pulses. The advantage of passive mode-locking is that it far exceeds the time response of any active modulation. In general, saturable absorbers can be further divided into two subcategories; *slow* and *fast*. Initially fast saturable absorbers were used in the form of organic dyes, where *fast* refers to the relaxation time of the absorber being fast with respect to the pulse duration. The limiting factor in the temporal duration of the first He-Ne lasers, was the net gain bandwidth available in the active medium. Lasing over a greater bandwidth was necessary to reduce pulse duration further. This is a direct

consequence of Fourier analysis, where greater bandwidths are needed to describe shorter time intervals. In 1966 DeMaria *et. al* [11] succeeded in producing sub-nanosecond pulses using Nd-glass as the active lasing medium. Their achievement relied on the medium's broader gain spectrum. By the end of the 1960's, Nd-YAG and Nd-glass lasers were consistently producing 10-ps pulses by means of passive mode-locking, making them central to the investigations of nonlinear optics and time-resolved spectroscopy.

A very successful mode-locking technique that became popular in the early 1970s was Mode-Locking by Synchronous Pumping (MLSP) [12]. This involves Amplitude Modulation (AM) mode-locking of a *slave* laser by synchronously pumping it with a *master* laser. Gain saturation is required to modulate the trailing edge of the pulse [13] (making this technique different to loss modulation mechanisms). The gain of the slave laser is controlled by the mode-locked pulses delivered by the master laser, and occurs on a faster timescale than the slower rise time of the pump pulse. This provides a route to shorten the pulses produced by the mode-locked master laser. The master laser that was commonly used in these early systems was Ar^+. The advantages of MLSP include higher efficiencies compared with passive mode-locking, and operating wavelengths that are not restricted by the saturable absorber bandwidth, thus presenting an element of tunability. Their disadvantages however were, longer pulses than passive mode-locking alone, and a pulse structure that is highly sensitive to mismatches and alignment between the respective laser cavities [14].

The next generation of mode-locked lasers was heralded by sub-ps pulses made possible by the combination of tunable broad-gain bandwidth dye lasers and slow saturable dye absorbers. The response time of the saturable absorber was not the limiting factor, as originally thought. This was demonstrated by New in 1974 [15, 16], who showed that the temporal duration of these systems was limited by the dynamic saturable gain. The saturable absorber causes the leading edge of the pulse to experience a loss, whilst the gain has saturated before the tail of the pulse has passed. This preferentially amplifies the centre of the pulse, as long as the recovery time is shorter than the period of the cavity [17]. Following improvements in the cavity and materials available, a new concept was utilised in a ring dye laser system that involved counter propagating pulses being amplified at the point of crossover; Colliding Pulse Mode-locking (CPM). CPM combined with the other conceptual and material advancements of the generation, led to the breaking of the 100 fs barrier [18]. Pulses of 10-100 fs thus became available during the 1980's. For an excellent history of mode-locking the reader is referred to [19].

The final generation of mode-locked lasers and the one we are still currently enjoying is that of Kerr-Lens Mode-locking (KLM) which was discovered in 1991 by Spence, Kean

and Sibbett [20] (St. Andrews). The Ti:sapphire laser now forms the heart of most of today's femtosecond pulse systems, and has been popular from the 1990's. The natural properties of this material are remarkable, and underlie the dominance of Ti:sapphire as an active medium for KLM. The two qualities that set it apart from other lasers are its huge gain bandwidth, spanning almost an octave (680-1130 nm), and its dynamic self mode-locking.

In KLM, the gain medium focuses the more intense regions of the pulse, which in the general case of a transverse Gaussian profile, causes the medium to act like a lens. The lensing effect is caused by the increased index of refraction in the centre of the beam compared with the wings, resulting in self-focussing. If an aperture is correctly placed, selection of the most intense region occurs and the remaining less intense regions become attenuated. Since shorter pulses possess higher peak intensities, they undergo less attenuation, making mode-locking favourable. KLM can be thought of as a special case of a fast passive absorber. Improvements in intra-cavity dispersion compensation and external pulse compression have led this laser to produce sub 3 fs pulses (after SPM broadening) [21]. In fact, today it is possible to purchase commercial lasers that can consistently produce sub 7 fs pulses. These pulses amount to $\simeq 2.5$ optical cycles (Femtolasers produktions GmbH). In theory, if one could phase lock the entire Ti:sapphire bandwidth with the correct spectral distribution, a pulse of $\simeq 2.5$ fs could be produced. At a central wavelength of 800 nm, this represents a single-cycle pulse. In practice, higher order dispersion along with the limited bandwidth of the mirrors prevents this limit from being reached directly. However, externally broadening the pulse through SPM followed by novel compression techniques, provides an indirect route to construct these single-cycle pulses. It remains a humbling thought, that $\simeq 10$ orders of magnitude have been traversed when comparing the first laser pulse durations, to those of today. Fig. 1.1 [22] shows the temporal reduction of the laser pulse since the discovery of mode-locking.

1.3 Frequency domain applications

Frequency metrology is another field that has greatly benefited from today's ultra-wideband pulses, and its importance is evidenced by the award of the 2005 Nobel prize to Roy J. Glauber, John L. Hall, and Theodor W. Hansch for their work on the subject. The spectral gap between optical frequencies and the Cs standard is approximately 600 THz, which meant that until recently only low frequencies could be directly measured. Higher e.g. optical frequencies had to be heterodyned, by means of complex frequency chains, and thus optical frequencies themselves were subject to ambiguity as the stan-

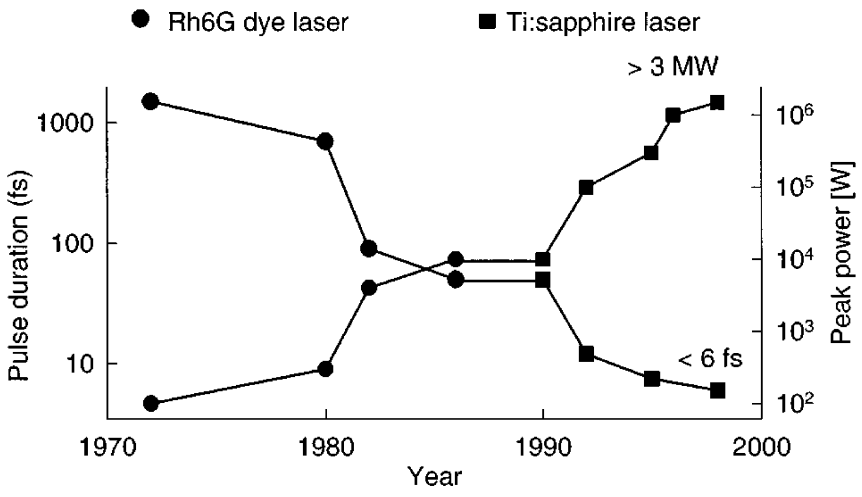

Figure 1.1: Pulse duration and peak power of Ti:sapphire and Dye lasers since 1970.

dard unit of time is the second. The ability of mode-locked lasers to produce octave wide frequency combs provides the perfect bridge between optical and r.f. frequencies [23]. For the first time in 1999, Hansch *et* al. [24] measured the absolute frequency of the Cesium D_1 line, with the help of a mode-locked KLM Ti:S laser. The laser was used to span a frequency range of nearly 20 THz, by connecting a 3.39 μm CH_4 stabilised HeNe laser to a laser locked onto the Cesium D_1 line. This pioneering approach heralded an improvement in accuracy of three orders of magnitude compared to previous measurements [23]. The use of such broad bandwidths has also been fully exploited in Carrier Envelope Phase (CEP) stabilisation, where self-referencing schemes have been used to measure and stabilise CEP slip, the most common being $f-2f$. $f-2f$ self-referencing involves frequency doubling the fundamental spectrum comb (from a train of pulses), and interfering this with the fundamental. A beat between the upper wing of the fundamental and the lower wing of the second harmonic takes place, creating an r.f. signal that can be tracked for phase stabilisation and control (this is investigated in chapter VII). The availability of such methods relies on ultra-wideband light being present in the fundamental spectrum. Thus, new frequency domain techniques exploiting wider bandwidths are being developed in parallel to the temporal reductions of today's few-cycle pulses. Much emphasis is now being placed on pulse measurement and characterisation, as few-cycle effects become much more important.

1.4 Conclusion

The laser might only be 50 years old, but it has enabled remarkable and fundamental breakthroughs within that time. In fact, in the past decade alone, 10 researchers have been awarded the Nobel prize for work relating to laser physics. The temporal reduction of coherent light is not the *only* outstanding achievement of laser science within this time. The increased intensity of laser pulses has been equally astounding and has further accelerated the growth of new science from the combination of both ultrashort *and* extremely intense laser light. The duration of laser pulses has gone from milliseconds to femtoseconds since 1964. Over that time, pulse intensities have soared from 10^2 W/cm^2 to 10^{21} W/cm^2 (see fig. 1.1). These fields are so intense that they far exceed the coulomb field within an atom (typically 10^{15} W/cm^2). Under such intensities, the electric field experienced by the electrons is no longer perturbative but rather enters the strong field regime. One such example of this is High Harmonic Generation (HHG), where the intensity of the electric field is used to tunnel ionise the electrons from inside an atom or molecule. The process involves distorting the potential well of the atom (or molecule) to such an extent that the electrons can pass through the reduced potential barrier. Once ionised, the electrons then follow the electric field profile, recolliding with the nucleus every half-cycle (depending on the polarisation of the electric field), producing attosecond bursts of coherent radiation on each recollision. For HHG, control of the CEP is crucial as the ionised electrons are sensitive to the absolute phase of the laser field. Thus by controlling the phase of the incoming laser field, isolated attosecond radiation can be produced. The potential of controllable attosecond pulses is so far reaching that it affects virtually every field and subfield of science, from chemical reactions, to metrology, and biology, and paves the way to measuring many fundamental processes. For an excellent detailed review of intense few-cycle laser fields, the reader is referred to [13], and [22] or alternatively a summary is provided in [25].

1.5 Thesis overview

The work in this thesis is primarily concerned with accurately modelling and understanding the nature of ultra-wideband pulses. This takes the reader through some early propagation techniques, before developing a new and efficient uni-directional pseudo-spectral method. *Pseudo-spectral* methods are more suitable for dealing with few-cycle pulses, providing a framework for the analysis of some ultrafast phenomenon, such as CWS. Through detailed spectral analysis, CEP effects are studied along with other areas

of coherent control.

- **Chapter II: Describing and Modelling the Ultra-Wideband Pulse**
  Chapter II begins with the standard application of Maxwell's equations to the modelling of laser pulses. This approach involves taking the second-order wave equation, and substituting a carrier-envelope description for the electric field. By separating the evolution of the field into transverse and longitudinal components, a first-order propagation equation can be recovered after making appropriate approximations. This commonly used technique is well documented and has formed the basis of much analysis [26–29].

  The general approach is demonstrated by deriving the Nonlinear Envelope Equation (NEE) [26]. This more sophisticated envelope technique is accurate down to a single-cycle pulse. The historical reason for the popularity of envelope methods has been their ease of computation, and numerical accuracy. The advent of Finite-Difference Time-Domain (FDTD) methods, coupled with the limitations of standard envelope techniques, has led to the growth of direct Maxwell solvers in recent years [30]. Comparisons of envelope methods to direct Maxwell solvers are made, highlighting the advantages and disadvantages of both.

  These differences are accentuated when dealing with few-cycle pulses in the presence of dispersion and nonlinearity. Some alternative approaches to calculating linear dispersion are discussed [30, 31] and the Pseudo-Spectral Spatial Domain (PSSD) technique is also explained [32], focussing on its ability to handle arbitrary linear dispersion.

- **Chapter III: Directional *G-variables***
  Chapter III introduces the directional *G-variables*. These variables allow the EM field to be written in terms of forward (G^+) and backward (G^-) directed fluxes by combining the electric and magnetic fields. They were first described in [33], but unfortunately early definitions were rather primitive being valid only within a dispersionless context.

  These definitions are generalised to handle dispersion, leading to a full derivation of Maxwell's equations. The directional *G-variables* come in pairs, where a reference parameter determines the balance of forward G^+ and backward G^- fluxes necessary to describe the EM field. Adjusting the reference parameter allows different combinations to be used, one of which fully represents the EM field with *just* the forward going G^+. Various $G^\pm$ combinations are used in this chapter to simulate nonlinear pulse propagation in a number of environments. The magnitude of backward-generated fields due to nonlinear propagation are also assessed. *Work*

relating to this chapter was published in [34].

- **Chapter IV: The Forward-Only Approximation**
  Chapter IV follows on from the results of the previous chapter. By selecting a reference parameter that matches the linear dispersion of a medium, the G^- field can be minimised. In almost all cases, nonlinear media do not generate significant backward propagating fields. This means that carefully chosen *reference parameters* combining the electric and magnetic fields can accurately describe the forward propagating G^+ pulse. By discarding the negligible G^- field, *the forward-only approximation* is made, leading to a first-order PDE with all the advantages of a uni-directional method (e.g. moving frame transformation).

  A bandwidth unlimited envelope technique is then developed using the G^+ uni-directional propagation equation. This supports the notion that carrier-envelope descriptions need not be bandwidth limited [35] as long as sufficient care is taken to express all the frequency content. Finally, a transverse dimension is added to the uni-directional model, using a split-step integration method.

- **Chapter V: Carrier Wave Shocking**
  This chapter investigates the nature of Carrier Wave Shocking (CWS) and how it is affected by dispersion. The phenomenon involves the self-steepening of the optical carrier due to third-order nonlinearity, and has a long but largely overlooked history [36]. The growth of FDTD techniques in recent years has led to renewed interest in this area [37, 38], but many questions remain unanswered.

  The chapter begins by explaining the process of CWS in dispersionless media. This allows a shock detection mechanism to be developed, as analytic solutions exist in the dispersionless regime. The shock detection schemes are then tested against fundamental parameters, revealing sensitivity to pulse duration, CEP etc. Using this knowledge, a step-by-step picture of CWS in the presence of dispersion is built up with the help of designer dispersion profiles. These profiles help pinpoint the region of parameter space where CWS may exist. Perhaps the most likely candidate for observing CWS is fused-silica, and the feasibility of realising this is assessed. *Work relating to this chapter was published in [39].*

- **Chapter VI: Carrier Shaping and Applications to HHG**
  Having understood the fundamentals of CWS in $\chi^{(3)}$ media, the phenomenon is then generalised. A formula is derived using the Method Of Characteristics (MOC) predicting shocking in any dispersionless arbitrary nonlinearity. The only other re-

alistic materials with significant nonlinearity are quadratic media, although they contain very different properties to $\chi^{(3)}$ media. Their asymmetric polarisation response, breaks the inversion symmetry of the incoming field, producing a novel type of self-steepening, which depends on the electric field value and not its intensity.

Recently, two-colour fields have been applied to High Harmonic Generation, taking advantage of the asymmetry of the electric field [40]. By making each adjacent half-cycle different, the high harmonics produced during one half-cycle can have a higher frequency content than the next. This helps isolate attosecond pulses, whilst also reducing their duration. Carrier steepened waveforms from quadratic media may improve on existing two-colour schemes, as the gradient of the incoming electric field is vital to harmonic production. This may provide a new parameter in coherent control that is capable of generating shorter attosecond pulses. *Work from this chapter has been submitted to Phy. Rev. A [41].*

- **Chapter VII: CEP Stabilisation and Measurement**
  Chapter VII begins by modelling a novel $0-f$ self-referencing technique described in [42, 43]. The scheme utilises Difference Frequency Generation (DFG) to passively stabilise the CEP slip of a few-cycle laser pulse. The spectral interference between the self-stabilised DFG and the laser pulse (experiencing the CEP slip), can be observed using a photodiode. The robustness of this technique to intensity and CEP variations is studied and explained.

  Absolute CEP must be known to fully characterise a few-cycle pulse. Loose time domain definitions are no longer valid in such cases, and because of this, CEP definitions in the frequency domain are developed. By understanding the phase structure of a pulse in the frequency domain, extensions to the $0-f$ self-referencing scheme are proposed for determining absolute CEP. The proposal is based on a mapping of the spectral interference using numerical simulations to the absolute CEP. *Work from this chapter is in preparation [44].*

- **Chapter VII: General Conclusions**
  Finally, conclusions are presented along with suggestions for further work.

Chapter 2

Describing and Modelling the Ultra-Wideband Pulse

The delicate few-cycle pulses of light emerging from mode-locked lasers are also formidable beasts. Because their intensities are so high, and their bandwidths so vast, a plethora of nonlinear activity can take place in even the most basic materials. This means that not only do the nonlinear interactions become very complicated, but also the description and modelling of such objects becomes ever more challenging. As the temporal duration and peak intensity of laser pulses have evolved, so have their description and numerical solutions. This chapter begins by discussing traditional descriptions of few-cycle pulses, starting with Maxwell's equations. The chapter then continues with more recent numerical methods highlighting their range of applicability. A full derivation of a sophisticated envelope technique is included [26], with an adaptation to the famous Nonlinear Schrodinger Equation (NLSE). The advantages and disadvantages of envelope methods compared to direct Maxwell solvers are considered.

2.1 Maxwell's equations and the second-order wave equation

Maxwell's equations form the starting point for describing a laser pulse. The four source-less Maxwell's equations are:

$$\nabla \cdot \vec{D} = 0 \tag{2.1a}$$

$$\nabla \cdot \vec{B} = 0 \tag{2.1b}$$

$$\nabla \times \vec{E} = -\frac{\partial \vec{B}}{\partial t} \tag{2.1c}$$

$$\nabla \times \vec{H} = \frac{\partial \vec{D}}{\partial t}, \tag{2.1d}$$

where $\vec{E}$, $\vec{D}$, $\vec{H}$ and $\vec{B}$, represent the electric, electric displacement, magnetic and magnetic induction fields respectively. The electric fields discussed in this thesis, fall into category of perturbative nonlinear optics, as their intensities are less than $\simeq 50$ TW/cm^2 [22].[1] This allows the polarisation ($\vec{P}$) to be expanded as a perturbation series, where the following constitutive relations apply:

$$\vec{D} = \epsilon_0 \vec{E} + \vec{P} \tag{2.2}$$

$$\vec{B} = \mu \vec{H} \tag{2.3}$$

$$\vec{P} = \epsilon_0 \chi^{(1)} * \vec{E} + \epsilon_0 \vec{P}_{NL} \tag{2.4}$$

$$\vec{P}_{NL} = \chi^{(2)} \vec{E}^2 + \chi^{(3)} \vec{E}^3 ... \tag{2.5}$$

ϵ and μ are the permittivity and permeability of the medium; $\epsilon = \epsilon_0 \epsilon_r$ and $\mu = \mu_0 \mu_r$. The subscripts "$_0$" and "$_r$" refer to the vacuum, and "relative" permittivity and permeability respectively. As this work will not deal with magneto-optic materials, only electric dispersion will be considered ($\epsilon_r = 1 + \chi^{(1)}$). $\chi^{(1)}$ is the linear susceptibility and refers to the temporal response of the linear polarisation to the incoming electric field. Though $\chi^{(1)}$ is a tensor, the media are assumed to be isotropic (the modelling of dispersion is discussed later in section 2.3.2). Within this work, and in common with other approaches [45], the nonlinear electric susceptibility ($\chi^{(n)}$) is assumed to be instantaneous. This assumption is valid when dealing with pulse durations of several femtoseconds propagating through relatively short bulk crystalline structures, as the nonlinear electronic response is typically less than a femtosecond (in the visible and near infra-red) [22]. Over greater

[1] The only exception is a brief discussion at the end of chapter VI which looks at how the gradient of carrier steepened pulses affects HHG.

distances e.g. fibre optic cables, other terms describing a Raman contribution would have to be added as in [28, 35], where the finite response of the nonlinearity is included. $\vec{P}_{nl}$ is also assumed to isotropic. Though this is not always the case, especially in $\chi^{(2)}$ media, situations where this condition is valid have been selected (e.g. $e + e \rightarrow e$ in LN [46]). Taking the curl of eq(2.1c), and enforcing eq(2.1a), equations (2.1c) and (2.1d) are combined, to arrive at the second order wave equation:

$$\nabla^2 \vec{E} = \mu \frac{\partial^2 \vec{D}}{\partial t^2} = \mu\epsilon \frac{\partial^2 \vec{E}}{\partial t^2} + \mu \frac{\partial^2 \vec{P}_{NL}}{\partial t^2}. \tag{2.6}$$

The above equation (2.6) forms the foundation of much nonlinear analysis, especially when deriving various envelope propagation equations, and is valid for small transverse inhomogeneities of $\vec{P}$

2.2 First-order envelope equations

Looking back over the history of laser pulses, it is not surprising that an envelope description was frequently employed as the theoretical tool for nonlinear analysis. An envelope description consists of three essential ingredients: a complex envelope function, an oscillating carrier, and a Carrier Envelope Phase (CEP). CEP is of little importance for pulses longer than a few cycles. However, for few-cycle pulses CEP becomes important, as light-matter interactions are phase sensitive. Discussions involving CEP stability and measurement are left until chapter VII.

Envelope descriptions and numerical methods have dominated few-cycle pulse propagation over recent decades because of their speed and accuracy. The key characteristics underlying their computational speed-up are

1. **Reduction of Order**. The second-order Partial Differential Equation (PDE) (see eq(2.6) can be reduced to a first-order derivative in the direction of propagation. The fundamental assumption, is that the pulse envelope varies on a much slower timescale than the carrier. This enables the simplification to be made, and is the primary reason for the computational speed-up [26].

2. **Directionality**. Envelope equations generally separate the E field into forward and backward propagating components. By neglecting the backward wave, a moving frame can be incorporated into the forward propagating envelope. Larger computational steps than those permitted in Finite Difference Time Domain methods (FDTD), can thus be made. FDTD methods must satisfy the Courant-Friedrich-

Levy (CFL) bound to guarantee numerical stability [30], placing an upper bound on the propagation step, and making moving frames difficult to incorporate. Thus an additional computational speed-up is possible when using an envelope with a moving frame. [A moving frame has been applied to FDTD [47], but this requires added sophistication, and other complicated stability criteria must then be adhered to.]

3. **Bandwidth constraints**. Generally the very definition of a slowly varying envelope, relies on the envelope not varying much over the period of the carrier. This essentially limits the bandwidth of frequencies used in the pulse description. Normally dispersion can then be included in the model by expanding the permittivity (or the wave vector), around the chosen central frequency (see section 2.2.1). Thus dispersion is handled by adding coefficients to the desired order e.g. the second order Group Velocity Dispersion (GVD). Given that envelope equations can be made to propagate in time, computationally expensive Fourier Transforms (FTs) or time-domain convolutions can be avoided, further increasing the speed of computation. The successes of the Non-Linear Schrodinger Equation (NLSE) is one such example of a time domain envelope model being used for nonlinear pulse propagation. Recently, bandwidth unlimited envelope models have been developed [35], and one such model is demonstrated in chapter IV; however these are not the norm. Furthermore the unlimited bandwidth comes at a price, as the computational demand becomes comparable to more explicit Maxwell solvers.

The accuracy of description coupled with the flexibility and speed of computation, has greatly helped the success of envelope techniques, and are still being developed today [35].

2.2.1 Envelope descriptions

It is essential to define a complex envelope when deriving an envelope propagation equation. This is because carrier-envelope descriptions are not unique [48]. The definitions used in [26] are therefore adopted, where they were successfully used to describe nonlinear pulse propagation down to a single-cycle. The electric field can be written as:

$$E(t) = \tilde{E}(t) + \text{c.c.} \tag{2.7}$$

$$\tilde{E}(t) = A(t)e^{i(k_0 z - \omega_0 t + \phi_0)}, \tag{2.8}$$

where $A(t)$ is the complex envelope, k_0 is the wave vector at the central frequency ($k_0 = \frac{\omega_0}{c} n_0$), and ϕ_0 is the CEP. As carrier-envelope descriptions are not unique, it is therefore possible to choose a carrier frequency, and from this fix the complex envelope. The combination of the carrier and complex envelope, must then retrieve the E field. An intuitive choice for the central frequency [26] is therefore:

$$\omega_0 = \frac{\int_0^\infty \omega |E(\omega)|^2 d\omega}{\int_0^\infty |E(\omega)|^2 d\omega}, \tag{2.9}$$

i.e. the centre of gravity of the frequency spectrum (and this choice is discussed later in chapter VII). In many-cycle pulses there is little difference between the central frequency defined in the time domain ($\omega_0 = \frac{ck_0}{n(\omega_0)}$) and the centre of gravity of the frequency domain eq(2.9). When the pulse duration approaches that of the carrier, a more robust definition is needed, necessitating eq(2.9). Similarly ϕ_0 (in eq(2.7)) only becomes significant with few-cycle pulses, and is defined so that the imaginary part of the complex envelope ($A(t)$) is zero at $t = 0$. $E(\omega)$ is simply the FT of $E(t)$. To demonstrate the effect of CEP, fig. 2.1 shows the change in peak intensity as a function of the number of cycles in the pulse (FWHM).

CEP significantly affects few-cycle pulses, but to have a meaning the complex envelope must be invariant under a change of phase. This ensures that the carrier and envelope remain fixed quantities and only their relative phase varies. Having an envelope or carrier that changes with CEP is counterproductive and completely lacking in any consistency. Another frequently neglected point when describing few-cycle pulses is the net-force condition, stating that any EM pulse must have no dc component when freely propagating [49]; a condition automatically satisfied if E is derived from the vector potential. In most cases, it has also become common practice to define a pulse in the time domain, from an envelope multiplied by the central carrier of choice (assumed to be ω_0). These loose definitions have virtually no effect on pulses containing more than a single cycle and it is therefore not surprising that they are often overlooked. However, as we are currently approaching single-cycle pulses in the visible and sub-cycle in the Terahertz regime [50], it becomes necessary to review many of our previous descriptions and models. Few and single-cycle nonlinear propagation introduce so many new effects and complexities that alternative descriptions and numerical techniques are vital to achieve accurate results. The remainder of this chapter reviews some of the more traditional approaches to nonlinear pulse propagation. The CEP and other fundamental characteristics of sub-cycle pulses are left to chapter VII, where a discussion of the net-force condition and its ramifications on few/sub-cycle pulses is included.

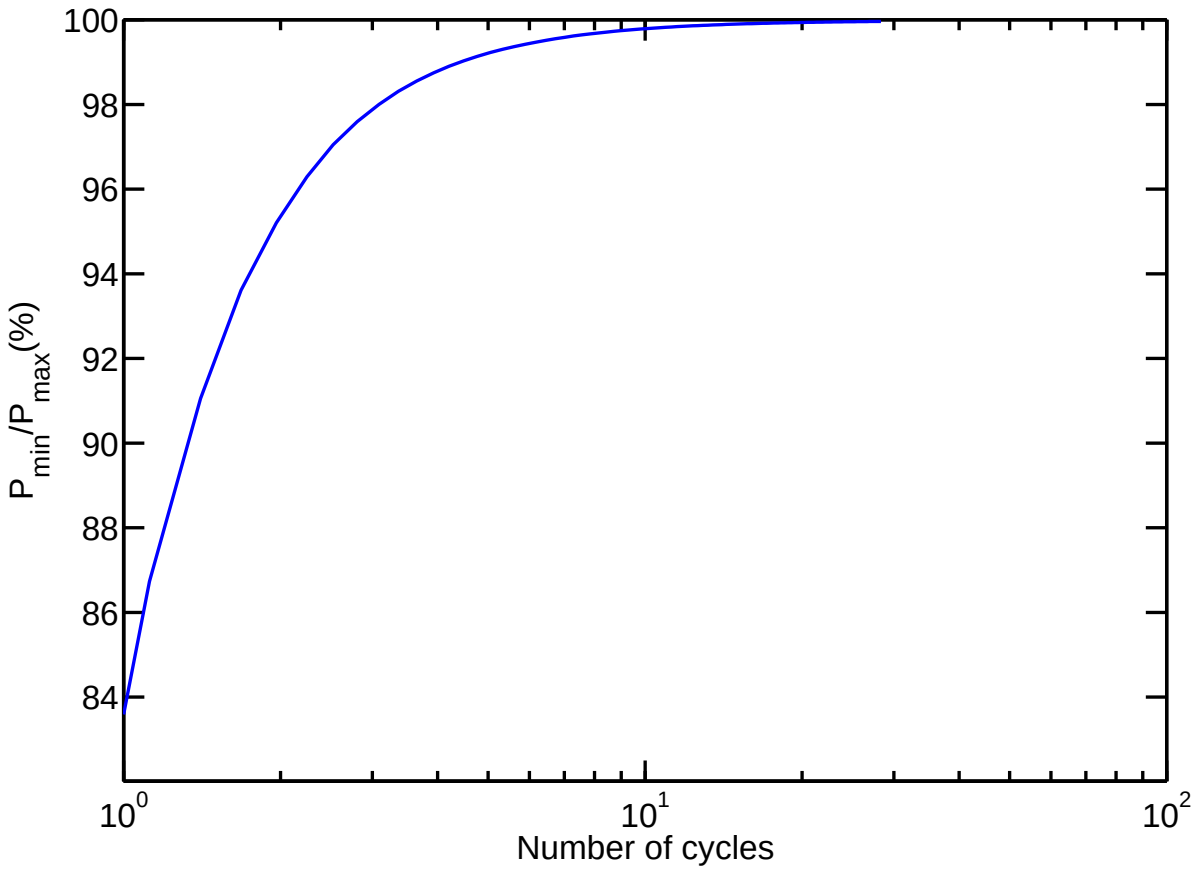

Figure 2.1: Maximum change in peak intensity as a function of pulse length ($\frac{P_{min}}{P_{max}}$). The envelope used was a sech function, and the maximum and minimum peak values refer to cosine and sine carriers respectively. CEP only significantly affects the peak intensity for few-cycle pulses.

To arrive at the first order envelope propagation equation we begin with the following Ansatz, and assume the pulse is linearly polarised and propagating in the z direction

$$E(r,t) = A(r_\perp, z, t)e^{i(k_0 z - \omega_0 t + \phi_0)} + \text{c.c.} \tag{2.10}$$

The E field is separated into transverse and longitudinal components, as is the ∇^2 operator that is applied later. Because eq(2.6) is nonlinear, it is necessary to define another complex envelope $B(r,t)$ describing P_{NL} in a similar fashion,

$$P_{NL} = B(r_\perp, z, t)e^{i(k_0 z - \omega_0 t + \phi_0)} + \text{c.c.} \tag{2.11}$$

Given the number of terms that appear when substituting eq(2.10) and eq(2.11) into eq(2.6), it is split up into three parts and rewritten, separating the second order equation

into transverse and longitudinal components. ($\frac{\partial}{\partial a} \rightarrow \partial_a$ is used as a shorthand for the 'derivative with respect to a' and $\nabla_\perp^2 = \partial_x^2 + \partial_y^2$ is the transverse Laplacian operator.)

$$(\partial_z^2 + \nabla_\perp^2)E(r,t) = \frac{1}{c^2}\partial_t^2 \int_{-\infty}^{t} dt' \epsilon(t-t')E(r,t') + \frac{1}{c^2}\partial_t^2 P_{NL}(r,t) \tag{2.12}$$

The terms on the left of eq(2.12) involve the spatial derivatives of the E field, and are simply

$$(\partial_z^2 + \nabla_\perp^2)E(r,t) = ((\partial_z + ik_0)^2 + \nabla_\perp^2)Ae^{i(k_0 z - \omega_0 t + \phi_0)} + \text{c.c}, \tag{2.13}$$

where the arguments of A have been dropped for brevity. The integral term on the right of eq(2.12) is the most complicated and involves linear dispersion. In the time domain the linear dispersion represents a convolution, namely

$$\int_{-\infty}^{t} dt' \epsilon(t-t')E(r,t') = \epsilon(t) * E. \tag{2.14}$$

A variety of ways exist to calculate linear dispersion, but a common method that is applied here, is to expand the dispersion around ω_0. In this case a FT is applied to eq(2.14), followed by the second-order time derivative

$$\int_{-\infty}^{+\infty} dt e^{-i\omega t} \frac{1}{c^2}\frac{\partial^2}{\partial t^2} \int_{-\infty}^{t} dt' \epsilon(t-t')E(r,t'). \tag{2.15}$$

The upper limit of the integral in eq(2.14) is extended to $+\infty$ to allow a convolution in the frequency domain. This is acceptable as $t > t' = 0$ for the integral to be causal [51]. The time derivative $\partial_t \rightarrow i\omega$ in the frequency domain. Eq(2.15) then becomes:

$$\begin{aligned} &\frac{1}{c^2}\int_{-\infty}^{+\infty} dt \quad e^{-i\omega t}\partial_t^2 \int_{-\infty}^{+\infty} dt' \epsilon(t-t')E(r_\perp, z, t') \\ &= \frac{(i\omega)^2}{c^2}\left(\int_{-\infty}^{+\infty} dt \quad e^{-i\omega t}\epsilon(t)\right)\left(\int_{-\infty}^{+\infty} dt e^{-i\omega t}E(r_\perp, z, t)\right) \\ &= -\frac{\omega^2}{c^2}\tilde{\epsilon}(\omega)\tilde{E}(r_\perp, z, \omega). \end{aligned} \tag{2.16}$$

Before the back FT (neglecting the $\frac{1}{2\pi}$ prefactors as they cancel out on successive FTs), the permittivity is rewritten in terms of the wave vector $k(\omega) = \frac{\sqrt{\epsilon(\omega)\omega}}{c}$, which can be

expressed as a Taylor expansion around ω_0 (or any arbitrary carrier)

$$-\frac{\omega^2}{c^2}\tilde{\epsilon}(\omega)\tilde{E}(r_\perp,z,t) = -k^2(\omega)\tilde{E}(r_\perp,z,\omega). \tag{2.17}$$

$$k(\omega) = \sum_{n=0}^{\infty}\frac{\gamma_n(\omega-\omega_0)^n}{n!}; \quad \gamma_n = \partial_\omega^n k(\omega)\mid_{\omega_0} = k_n + i\sigma_n. \tag{2.18}$$

where k and σ refer to the dispersion and absorption respectively. Eq(2.17) is now expanded using eq(2.18). This allows the extraction of the lower order terms referring to phase velocity, group velocity and absorption. Thus,

$$-k^2(\omega)E(r_\perp,z,\omega) \quad = -(k_0 + i\sigma_0 + k_1\omega + \hat{D_\omega})^2 E(r_\perp,z,\omega) \tag{2.19}$$

where

$$\hat{D_\omega} = \sum_{n=2}^{\infty}\sigma_1 + \frac{\gamma_n(\omega-\omega_0)^n}{n!}. \tag{2.20}$$

A final FT returns us to the time domain, where the second term can now be written as:

$$\frac{1}{c^2}\partial_t^2\int_{-\infty}^{t} dt'\epsilon(t-t')E(r,t') = -(k_0 + i\sigma_0 + ik_1\partial_t + \hat{D})^2 A e^{i(k_0 z-\omega_0 t+\phi_0)} \tag{2.21}$$
$$+\text{c.c.}$$

Finally, the last term on the right hand side of eq(2.6) yields:

$$\begin{aligned}\frac{1}{c^2}\frac{\partial^2 P_{NL}}{\partial t^2} &= \frac{1}{c^2}(\partial_t - i\omega_0)^2 B e^{i(k_0 z-\omega_0 t+\phi_0)} \\ &= \frac{\omega_0^2}{c^2}(1+\frac{i}{\omega_0}\partial_t)^2 B e^{i(k_0 z-\omega_0 t+\phi_0)} + \text{c.c.}\end{aligned} \tag{2.22}$$

Re-combining eqs.(2.13),(2.21) and (2.22), the second-order wave equation (2.12) can be re-expressed as:

$$((\partial_z + ik_0)^2 + \nabla_\perp^2)A + (k_0 + i\sigma_0 + ik_1\partial_t + \hat{D})^2 A = \frac{\omega_0^2}{c^2}(1+\frac{i}{\omega_0}\partial_t)^2 B, \tag{2.23}$$

where the equation has been separated into its conjugate parts and the common exponential (relating to the carrier frequency) has been removed. If desired, the E field can be retrieved by inserting the extracted carrier, followed by a summation with the conjugate solution. This technique is very common in nonlinear optics, the most famous example being the Non-Linear Schrodinger Equation (NLSE) [45]. In the following section (2.2.2)

the Nonlinear Envelope Equation is derived, as is the NLSE.

2.2.2 The Nonlinear Envelope Equation (NEE)

In this section the Nonlinear Envelope Equation (NEE) (see [26]) is derived, to demonstrate the assumptions and general approach taken when producing an envelope propagation model. The Non-Linear Schrodinger Equation (NLSE) is also included, as it describes one of the most famous equations of nonlinear optics. In general, envelope methods discard any backward propagating components (assumed to be zero), before transforming into a moving frame. These simple steps, along with the removal of the carrier can be used to calculate nonlinear propagation, where an inherent uni-directional assumption is present. The validity of the above assumption i.e. 'no backward propagating pulse' is discussed in chapter III when dealing with the directional *G-variables*.

The advantages of a moving frame transformation have already been stated. A variety of different transformations are possible, but common choices are the phase velocity of ω_0, and the group velocity of the pulse. Moving at the phase velocity of the central frequency 'freezes' the carrier oscillations, but if GVD is present the pulse will walk across the frame at the group velocity. In this case the following moving frame transformation is made

$$\begin{aligned} \tau &= t - k_1 z \\ \zeta &= z \\ \partial_t &\rightarrow \partial_\tau \\ \partial_z &\rightarrow \partial_\zeta - k_1 \partial_\tau, \end{aligned} \tag{2.24}$$

which is a transformation into the group velocity moving frame (τ and ζ are the moving frame time and spatial coordinates respectively). Applying eq(2.24) to eq(2.23) yields new terms wherever ∂_z was present in the stationary frame:

$$\begin{aligned} &(-k_0^2 + 2ik_0\partial_\zeta - 2ik_0k_1\partial_\tau + \partial_\zeta^2 - 2k_1\partial_\zeta\partial_\tau + k_1^2\partial_\tau^2 + \nabla_\perp^2)A \\ &+ (k_0^2 - \sigma_0^2 - k_1^2\partial_\tau^2 + \hat{D}^2)A \\ &+ (2ik_0\sigma_0 + 2ik_0k_1\partial_\tau + 2k_0\hat{D} - 2\sigma_0k_1\partial_\tau + 2i\sigma_0\hat{D} + 2ik_1\partial_\tau\hat{D})A = \frac{\omega_0^2}{c^2}\left(1 + \frac{i}{\omega_0}\partial_\tau\right)^2 B. \end{aligned} \tag{2.25}$$

The next step is to divide through by $2ik_0$, cancelling the relevent terms. This gives

$$\left(\partial_\zeta + \frac{\partial_\zeta^2}{2ik_0} + \frac{ik_1}{k_0}\partial_\zeta\partial_\tau + \frac{\nabla_\perp^2}{2ik_0}\right)A + \frac{1}{2ik_0}(-\sigma_0^2 + \hat{D}^2)A \tag{2.26}$$
$$+ \left(\sigma_0 - i\hat{D} + \frac{i\sigma_0 k_1}{k_0}\partial_\tau + \frac{\sigma_0}{k_0}\hat{D} + \frac{k_1}{k_0}\partial_\tau\hat{D}\right)A = \frac{\omega_0^2}{c^2}\left(1 + \frac{i}{\omega_0}\partial_\tau\right)^2 B.$$

Eq(2.26) is now re-arranged into a form, facilitating a later approximation into the NEE:

$$\left(1 + \frac{i}{\omega_0}\partial_\tau\right)\left[(\partial_\zeta + \sigma_0 - i\hat{D})A + \frac{k_0}{2in_0^2}(1 + \frac{i}{\omega_0}\partial_\tau)B\right] + \frac{1}{2ik_0}\nabla_\perp^2 A \tag{2.27}$$
$$= \left(\frac{k_0 - \omega_0 k_1}{k_0}\right)\frac{i}{\omega_0}\partial_\tau(\partial_\zeta + \sigma_0 - i\hat{D})A - \frac{1}{2ik_0}(\partial_\zeta^2 + \hat{D}^2 - \sigma_0^2 - 2i\sigma_0\hat{D})A,$$

using

$$i\frac{k_1}{k_0}\partial_\tau\partial_\zeta = \frac{i}{\omega_0}\partial_\tau\partial_\zeta - \left(\frac{k_0 - \omega_0 k_1}{k_0}\right)\frac{i}{\omega_0}\partial_\tau\partial_\zeta. \tag{2.28}$$

[26] and [27] discuss the approximation of $k_1/k_0 \rightarrow 1/\omega_0$, when the phase velocity is similar to the group velocity. If the following condition (2.29a) and either (2.29b) or (2.29c) are satisfied

$$| \partial_\zeta A | << k_0 | A | \tag{2.29a}$$
$$| \partial_\tau A | << \omega_0 | A | \tag{2.29b}$$
$$| \frac{k_0 - \omega_0 k_1}{k_0} | << 1 \tag{2.29c}$$

we arrive at the NEE of Brabec and Krausz [26]

$$\partial_\zeta A = -\sigma_0 A + i\hat{D}A + \frac{i}{2k_0}\left(1 + \frac{i}{\omega_0}\partial_\tau\right)^{-1}\nabla_\perp^2 A + \frac{ik_0}{2n_0^2}(1 + \frac{i}{\omega_0}\partial_\tau)B. \tag{2.30}$$

Eq(2.30) is valid down to a single-cycle, and explains why envelope equations have been the primary means for calculating long distance nonlinear propagation. Ignoring the diffraction ($\nabla_\perp^2$) and absorption term (σ_0) and taking $\hat{D} = -(k_2/2)\partial_\tau^2$ (i.e. dispersion up to GVD is included), yields the famous nonlinear Schrodinger equation (NLSE)

$$\partial_\zeta A = \frac{ik_2}{2}\partial_\tau^2 A + \frac{ik_0}{2n_0^2}\left(1 + \frac{i}{\omega_0}\partial_\tau\right)B. \tag{2.31}$$

The NLSE has been extensively used, especially in the case of nonlinear propaga-

tion through optical fibers [45], as diffraction can be disregarded. Variants of the NLSE (eq(2.31)) have appeared in the literature, including varying orders of disperion, nonlinearity and Stimulated Ramman Scattering [26–29]. The computational advantages of envelope equations coupled with their simplicity and accuracy has led to their dominance in many nonlinear pulse propagation models. Even today envelope techniques are being developed [35]. However, as pulses become shorter with ever increasing bandwidths, envelope descriptions either break down or become increasingly computationally expensive - involving bandwidths, and discretisations as demanding as direct Maxwell solvers.

2.3 Direct Maxwell solvers

Direct Maxwell solvers have been steadily evolving since World War II [30]. The growing use of radar technology and the desire to understand the effects of an Electro-Magnetic Pulse (EMP) triggered military defence programs into investing heavily in solving these equations. The advent of the Finite-Difference Time-Domain method (FDTD) introduced by Yee (though the name was later coined by Taflove) in 1966 [52] along with the growing use of computers caused a surge in direct Maxwell solvers. Yee's algorithm provided a powerful and efficient framework in which to solve Maxwell's curl equations. Since then, FDTD has undergone continuous development. The accuracy of FDTD is solely limited by volumetric sampling as no approximations are made. The initial and boundary conditions are set-up, and the discretisation of space and time allows the evolution of Maxwell's equations in that region to proceed.

The fundamental difference between direct Maxwell solvers and envelope techniques lies in the system of equations being solved. Envelope techniques assume an envelope and develop a first-order wave equation with respect to that envelope, whereas FDTD solves Maxwell's coupled equations in order to evolve the EM field. Because FDTD is only constrained by numerical resolution, it has become especially important with the arrival of Terahertz sub-cycle pulses. The accuracy however comes at a cost; explicit solutions are computationally very demanding, meaning that for long distances and multiple dimensions, direct Maxwell solvers are cumbersome and slow. The reason for the slowness lies principally in the convergence criteria. The Courant-Friedrich-Levy (CFL) bound must be obeyed to ensure stable integration, setting a bound on the time (or marching) step, relative to the spatial grid (see [30] for a detailed analysis of the CFL stability criterion).

2.3.1 Yee's algorithm-FDTD

To demonstrate Yee's FDTD scheme, we begin from Maxwell's curl equations. Though a 3-dimensional FDTD algorithm is possible, the 1D version is sufficient here. E_x and H_y are plane waves polarised in the x and y directions respectively, both propagating in the z direction. Beginning from eq(2.1c) and (2.1d) in section 2.1, yields:

$$\begin{aligned} \frac{\partial D_x}{\partial t} &= -\frac{\partial H_y}{\partial z} \\ \mu_0 \frac{\partial H_y}{\partial t} &= -\frac{\partial E_x}{\partial z}. \end{aligned} \tag{2.32}$$

Yee's discretisation scheme uses central differencing in time and space to calculate new second order accurate field values [52]. This is achieved with both a staggered grid and staggered initial conditions (e.g. $E(t = 0)$ and $H(t = 1/2\Delta t)$). By offsetting the E and H fields at half grid points in space and time, the following leap-frog scheme is possible:

$$\begin{aligned} H_y|_{i+1/2}^{n+1/2} &= H_y|_{i+1/2}^{n-1/2} - \frac{\Delta t}{\mu \Delta z}(E_x|_{i+1}^{n} - E_x|_{i}^{n}) \\ D_x|_{i}^{n+1} &= D_x|_{i}^{n} - \frac{\Delta t}{\Delta x}(H_y|_{i+1/2}^{n+1/2} - H_y|_{i-1/2}^{n+1/2}) \\ E_x|_{i}^{n+1} &= \epsilon_i^{-1} f(D_x|_{i}^{n+1}, D_x|_{i}^{n} ...) \end{aligned} \tag{2.33}$$

where '$_i$' and '^{n}' refer to space and time respectively, and f is a function to be determined e.g. using recursive-convolution methods [31]. The simplest FDTD scheme (eq(2.33) above) is second-order accurate in space and time. A schematic diagram of a staggered FDTD grid can be seen in fig. 2.2.

In general, computationally demanding and relatively inflexible methods are needed to calculate D. This is because there is no longer a simple relationship between D and E but rather, $D = \epsilon * E$ representing a convolution in time (of the permittivity with E). This convolution is avoided using Tyrrell's Pseudo-Spectral Spatial Domain (PSSD) method [32] which is discussed in the next section.

2.3.2 Incorporating dispersion

Within the context of bulk crystalline materials, linear dispersion describes the finite response time of the dielectric to the driving E field. Common models for this temporal

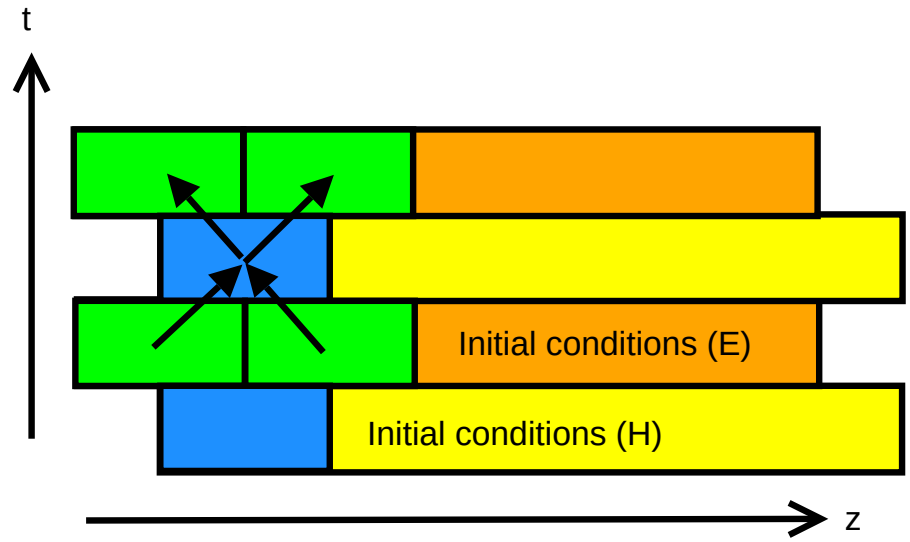

Figure 2.2: Schematic diagram of an FDTD grid, staggered in both space and time. Note the initial conditions are also offset in space and time by half grid points.

response are Debye and Lorentz dispersion [30]. For narrowband pulses being modelled with an envelope technique, the dispersion calculation is simply an expansion around the central frequency to the desired dispersive order (see eq(2.17)). A simple multiplication of the coefficient(s) with the E field, thus obviates the need for a convolution. The nonlinearity is then calculated, either with a single PDE (e.g. NLSE) or by coupling two first order PDEs together. For example in the case of Second Harmonic Generation (SHG), two coupled equations are simultaneously solved using a split-step method, where each equation describes the evolution of a different envelope (ω_0 and $2\omega_0$).

Directly solving Maxwell's equations for few-cycle pulses brings with it an additional challenge. Few-cycle pulses contain huge bandwidths, potentially exposing the pulse to a larger range of dispersion. To make matters worse, when the system is nonlinear e.g. SHG, each frequency in the vast bandwidth undergoes frequency mixing. The abundance of parametric processes simultaneously taking place in a relatively simple wideband nonlinear problem is staggering. For these reasons, the characteristics of wideband nonlinear pulse propagation remain vastly different to their narrowband counterparts.

Since dispersion plays such a crucial role in nonlinear optics, it is of paramount importance to accurately model it. As the linear response is much slower than the nonlinear for the cases presented (see [22] for a discussion of the nonlinear response within the perturbative limit), the finite response of the nonlinearity is ignored. In FDTD, the two main methods to calculate linear dispersion are: recursive-convolution and direct time

integration methods [31]. Both of these approaches use auxiliary equations to calculate dispersion. The complication stems from dispersion being more natural to the frequency domain and thus awkward convolutions must be calculated in the time domain. The Pseudo-Spectral Spatial-Domain (PSSD) technique elegantly avoids these burdensome convolutions by making use of the Fourier domain, but before describing this approach, it is instructive to look at some related techniques.

The Pseudo-Spectral Time-Domain (PSTD) method is another direct Maxwell solver founded on Yee's FDTD scheme. In FDTD, time and space are staggered and the simulation proceeds from a spatially defined initial condition by marching forward in time (see fig. 2.2). Any derivative is dealt with in the pre-defined domain (time in this case) where, depending on the level of accuracy desired, a 2^{nd} or higher order derivative (e.g. 4^{th} order Runga-Kutta) can be calculated.

Like FDTD, the initial conditions in PSTD are specified in space, but the method of calculating the derivative is different. Instead of calculating spatial derivatives through central differencing schemes, a Fourier convolution theorem is used, where $\frac{\partial Q(x,t)}{\partial x} \rightarrow \mathcal{F}^{-1}[-ik_xQ(k_x,t)]$. These spatial derivatives are N^{th} order accurate (where N depends on the number of grid points), significantly improving the efficiency of problems involving wideband dispersion, or other nonlinear processes that demand a high level of spatial resolution. The linear polarisation however is calculated in time and remains a challenging part of the problem. If FDTD is a 'tz' method then PSTD is 'tk', where 't' refers to the direction the iteration marches forward, and 'k' refers to the domain of the derivative (i.e. the spatial Fourier domain).

The PSSD technique is the natural progression from PSTD, but contains additional advantages. The initial conditions are stored in time (as opposed to space) and the algorithm iterates forward in space (z). Using a Fast Fourier Transform (FFT) the derivatives in time are calculated using the Fourier convolution theorem, extending the advantages of PSTD. Not only does it allow an N^{th} order accurate derivative (in time) to be calculated but also simplifies dispersion. Because the derivative of the D vector is with respect to time ($\partial_t D$), a simple multiplication of the permittivity $\epsilon_0\epsilon(\omega)$ and an N^{th} order accurate derivative ($i\omega$) can be applied simultaneously. The PSSD algorithm is laid out as follows:

$$\begin{aligned} E_x(t)|_i^n &= E_x(t)|_{i-1}^n - \mu_0\Delta z\mathcal{F}^{-1}[i\omega\mathcal{F}[H_y(t)|_{i-1/2}]] \\ H_y(t)|_{i+1/2}^n &= H_y(t)|_{i-1/2}^n - \epsilon_0\triangle z\mathcal{F}^{-1}[i\omega D_x(\omega)|_i] \\ D_x(\omega)|_i &= \epsilon_0\epsilon(\omega)\mathcal{F}[E(t)|_i] + P^{nl}, \end{aligned} \tag{2.34}$$

where the nonlinear polarisation is again assumed to be instantaneous, and can be added linearly (in the frequency domain) after calculating the dispersive contribution namely $\epsilon * D = \mathcal{F}^{-1}\left[\epsilon_0\epsilon(\omega)E(\omega)\right] + P^{nl}$. A backwards FT is then applied to the sum of the derivatives. In a similar manner to PSTD, and for identical reasons, PSSD's E and H are not staggered in time (but remain staggered in space). PSSD allows dispersion to be handled in the frequency domain and run times are at least equivalent to FDTD models. PSSD's flexibility in dispersion management is the key to its success when modelling ultra-wideband pulses. It is later used to understand the broadband dispersive characteristics of Carrier Wave Shocking (CWS), and forms the backbone of the dispersion management applied to directional *G-variables* [34] in the next chapter.

2.4 Conclusion

This chapter began with envelope descriptions based on Maxwell's equations. When envelopes are applied to the second-order wave equation, various propagation models (describing the complex envelope), naturally arise. These equations have the advantage of being both directional and first-order with respect to the direction of integration. Various approximations lead to a variety of alternatives, all of which contain some underlying assumptions. In this chapter, the NEE and the more famous NLSE were derived from Maxwell's equations, to demonstrate the more traditional approach to nonlinear pulse propagation. The advantages of envelope equations lie in their simplicity and speed of computation.

Shorter pulses require more robust descriptions, and have encouraged the development of different Maxwell solvers. One of the challenges faced by few-cycle pulses, is how to accurately model dispersion. An assortment of methods exist to meet this need, but they are not always efficient, especially when the modelling of exotic dispersion is required. PSSD is an efficient technique, which can be easily adapted into other numerical approaches and forms an important part of *G-variables* in the following chapter.

The following dilemma exists when choosing a method to calculate nonlinear pulse propagation: Is it better to improve faster envelope calculations, that are being pushed to their effective limits, slowing them down in the process, or is it preferable to explicitly solve Maxwell's equations, paying the price of restrictively slow calculations?

As we shall see later, for most dielectric materials, envelope equations can be developed to be sufficiently accurate so as to handle a diverse range of nonlinear propagation.

Chapter 3

Directional *G-variables*

3.1 Introduction

3.1.1 Brief history and motivation

At the start of a paper titled 'Ultrashort-Pulse Generation by Q-Switched Lasers' (1970), J. A. Fleck introduced a pair of directional field variables by re-arranging Maxwell's equations [33]. A brief analysis followed, where these variables were used to separate an EM beam into forward and backward propagating components by combining the electric and magnetic fields. The idea was not developed further. A similar concept did however arise in [53, 54], where projection operators were used for directional pulse propagation. Another construction involving spatially varying permittivities was developed in [55, 56], describing propagation through gratings, where the fields in both forward and backward directions were retained.

The need to accurately model few-cycle pulses is more pertinent now than ever. As standard envelope techniques are stretched to their effective limits, the use of direct Maxwell solvers is becoming more widespread [31, 32, 45]. Despite the increase in computational power available, the resources necessary to solve large multi-dimensional nonlinear problems remains restrictive. This either limits the number of dimensions included, or reduces the distance of propagation possible. The application of directional variables to these problems may provide a solution.

The advantages, and the motivation for their development are as follows:

1. **Computational speed-up.** If the EM field can be separated into forward (G^+) and backward (G^-) propagating components, it is usually possible to select a direction in which most of the EM energy travels. In such cases, if the backward propagating field is small enough to be ignored, Maxwell's curl equations can be

reduced to a single first order PDE. A moving frame can then be incorporated providing further computational gains.

2. **Measurement of backward reflected fields.** It is common in nonlinear optics to ignore small backward propagating components. Recently, claims of generating backward-propagating second harmonic fields were made [57] (another example of envelope equations breaking down). Directional *G-variables* enable the magnitude of any backward propagating components to be calculated. Thus, the validity of discarding the initial backward component can be assessed, or the magnitude of any other subsequently generated field determined.

3. **Additional insight.** *G-variables* provide additional insight into nonlinear problems and simulations. Furthermore, their application does not demand their use throughout a simulation, since they can be constructed at any stage from E and H fields if desired.

In this chapter the *G-variables* are first introduced and the original definitions are then generalised to parameterise dispersive media. A re-derivation of Maxwell's equations with *G-variables* is included to highlight the fidelity of these directional variables to EM theory. As we shall show, the precise definition of the directional variables depends on the choice of the so-called "reference parameters". These reference parameters play a key role, when considering the forward and backward field contributions.

The directional aspect of *G-variables* is rather subtle, as *direction* refers to the energy flux, not necessarily the direction of propagation. Most cases in this chapter consider forward propagating G^- fields that arise from linear dispersion. There are however some exceptional cases where, backward-propagating fields can be generated.

The chapter includes simulation results, to demonstrate the application of *G-variables* to nonlinear pulse propagation and the effect different reference parameters have. Results showing backward propagating pulses are also illustrated explaining their magnitude and nature. By reducing the amount of backward waves present in a $G^{\pm}$ pair, the forward only field can be exclusively used in the calculation. This chapter lays down the foundations for the *forward-only approximation*; an approximation that is necessary to capitalise on the uni-directional nature of typical pulse propagation problems. [Section *3.3 is a re-derivation of Maxwell's equations that can be skipped over at first reading.]

3.1.2 $G^{\pm}$: Early definitions

The original $G^{\pm}$ definitions introduced for a plane polarised pulse ($E_x(t)$ and $H_y(t)$), propagating in the $+z$ direction of a non-dispersive medium [33] were:

$$G^{\pm}(t) = \epsilon^{1/2} E_x(t) \quad \pm \quad \mu^{1/2} H_y(t). \tag{3.1}$$

The substitution of eq(3.1) into the coupled, sourceless Maxwell equations, enables the EM field to be rewritten into forward ($+z$) and backward ($-z$) components. Maxwell's equations therefore appear as

$$\begin{aligned} \sqrt{\epsilon\mu}\partial_t G^+ + \partial_z G^+ &= 0 \\ G^- &= 0, \end{aligned} \tag{3.2}$$

where the permittivity ϵ and permeability μ are constants. The EM fields are now in directional form, with no loss of generality for a *simple non-dispersive case*.

3.2 Generalising the model

3.2.1 Dispersive references

As mentioned in chapter II, modelling dispersion is essential in any realistic nonlinear problem. The original definitions of $G^{\pm}$ are dispersionless and are therefore very limited in their potential application. By incorporating dispersion into the permittivity (ϵ), and permeability (μ) of eq(3.1) it is possible to generalise $G^{\pm}$ to include dispersion. The $G^{\pm}$ definitions can be generalised in the time and frequency domains so that

$$\vec{G}(t)^{\pm} = \alpha_R(t) * \vec{E}(t) \pm \vec{u} \times \beta_R(t) * \vec{H}(t) \tag{3.3}$$

$$G^o(t) = \vec{u} \cdot [\beta_R(t)\vec{H}(t)] \tag{3.4}$$

and

$$\vec{G}(\omega)^{\pm} = \tilde{\alpha}_R(\omega)\vec{E}(\omega) \pm \vec{u} \times \tilde{\beta}_R(\omega)\vec{H}(\omega) \tag{3.5}$$

$$G^o(\omega) = \vec{u} \cdot [\tilde{\beta}_R(\omega)\vec{H}(\omega)]. \tag{3.6}$$

Here " $\tilde{}$ " indicates the frequency domain, and the subscript "$_R$" means **Reference**. $\tilde{\alpha}_R = \sqrt{\tilde{\epsilon}_R}$, and $\tilde{\beta}_R = \sqrt{\tilde{\mu}_R}$, are referred to as 'reference parameters', as are their Fourier back transforms $\alpha_R(t)$ and $\beta_R(t)$ (respectively). In all simulations $\beta_R = \beta_0 = \sqrt{\mu_0}$, and

ϵ_0 and μ_0, are included in ϵ_R and μ_R respectively. $\vec{u}$ is a unit vector in the direction of propagation, and "$*$" denotes a convolution in time. The superscript "^{o}" represents the longitudinal part of the EM field that has not been picked out by the "$\times$" term.

The choice of $\tilde{\epsilon}_R(\omega)$ in the construction of $G^{\pm}$ is completely arbitrary and can be chosen to be a constant or a function of frequency, providing enormous flexibility in the choice of reference. However, in general there are three common choices for the reference parameters:

1. $\tilde{\alpha}_R(\omega) = \sqrt{\epsilon_0}$. The most basic construction of $G^{\pm}$, where the reference permittivity is chosen from the vacuum permittivity.

2. $\tilde{\alpha}_R(\omega) = \kappa\sqrt{\epsilon_0}$. In this case, a constant reference permittivity κ is chosen to partially match the dispersive medium. For example, in a medium where the refractive index ranges between 1.4-1.6, $\kappa = 1.5$ might be chosen as a compromise.

3. $\tilde{\alpha}_R(\omega) = \sqrt{\epsilon_0\tilde{\epsilon}(\omega)}$. In this case $\tilde{\alpha}_R(\omega)$ fully matches the permittivity of the medium $\tilde{\epsilon}(\omega)$.

The choice of reference permittivity ($\tilde{\alpha}_R(\omega)$) has a large effect on the magnitude of G^{-}. An example (of case 2 above) that will be used later, is the average of $\tilde{\epsilon}_r(\omega)$ over the pulse bandwidth, namely

$$\epsilon_{av} = \frac{1}{N}\sum_{i=1}^{N}\tilde{\epsilon}_r(\omega_i), \tag{3.7}$$

which in the case of fused silica is $\simeq 2.70$ ($\alpha_{av} = \sqrt{\epsilon_{av}\epsilon_0}$).

These reference parameters represent the most practical choices, but in theory there is an infinite number of $G^{\pm}$ pairs that can be used to construct the $\vec{E}$ and $\vec{H}$ fields. It is possible to decompose $\tilde{\epsilon}$ into correction ("$_C$") and reference("$_R$") components, and this is necessary for cases where $\tilde{\alpha}_R^2$ does not match $\tilde{\epsilon}$, namely

$$\tilde{\epsilon} = \tilde{\alpha}^2 = \tilde{\alpha}_R^2 + \tilde{\alpha}_R\tilde{\alpha}_C \tag{3.8}$$

$$\tilde{\mu} = \tilde{\beta}^2 = \tilde{\beta}_R^2 + \tilde{\beta}_R\tilde{\beta}_C. \tag{3.9}$$

As we shall see later, the magnitude of G^{-} is very important when considering a G^{+} *only* description. Inverting the $G^{\pm}$ definitions enables the reconstruction of $\vec{E}$ and $\vec{H}$ as

follows:

$$\vec{E}(\omega) = \frac{1}{2\tilde{\alpha}_R(\omega)}[\vec{G}^+(\omega) + \vec{G}^-(\omega)] \tag{3.10}$$

$$\vec{H}(\omega) = \frac{1}{2\tilde{\beta}_R(\omega)}\vec{u} \times [\vec{G}^+(\omega) - \vec{G}^-(\omega)] + \frac{\vec{u}G^o(\omega)}{\tilde{\beta}_R(\omega)}. \tag{3.11}$$

3.2.2 Energy density and Poynting vector

The Poynting vector ($\vec{S}$) reveals some directional aspects of the *G-variables*. In the general case, $\vec{S}$ takes on a complicated form (because the cross product in time turns into a convolved cross product in frequency space):

$$\begin{aligned} \vec{S} &= \vec{E} \times \vec{H} \\ \vec{S} &= \frac{1}{4}\{(\mathcal{F}^{-1}[\tilde{\alpha}_R^{-1}] * \vec{G}^+) \cdot (\mathcal{F}^{-1}[\tilde{\beta}_R^{-1}] * \vec{G}^+) \\ &\quad - (\mathcal{F}^{-1}[\tilde{\alpha}_R^{-1}] * \vec{G}^+) \cdot (\mathcal{F}^{-1}[\tilde{\beta}_R^{-1}] * \vec{G}^+)\}\vec{u}, \end{aligned} \tag{3.12}$$

but in the simpler case of dispersionless reference parameters, yields

$$\vec{S} = \frac{1}{4\sqrt{\alpha_R\beta_R}}\left[\left(\vec{G^+} \cdot \vec{G^+}\right) - \left(\vec{G^-} \cdot \vec{G^-}\right)\right]\vec{u}. \tag{3.13}$$

Eq.(3.13) highlights the directional flux of $G^{\pm}$. The dot product ensures that $\left(\vec{G}^{\pm} \cdot \vec{G}^{\pm}\right)$ is positive, and is therefore directed in either the positive or negative direction ($\pm\vec{u}$).

In general EM theory the energy density appears as:

$$U = \frac{1}{2}(\vec{D} \cdot \vec{E} + \vec{B} \cdot \vec{H}), \tag{3.14}$$

but with $G^{\pm}$ a rather complicated form arises. For the special case of a non-dispersive reference, the result is

$$\begin{aligned} U = &\frac{1}{8}\left(\left[\frac{\epsilon}{\epsilon_R} + \frac{\mu}{\mu_R}\right] * \vec{G}^+\right) \cdot \vec{G}^+ + \frac{1}{8}\left(\left[\frac{\epsilon}{\epsilon_R} + \frac{\mu}{\mu_R}\right] * \vec{G}^-\right) \cdot \vec{G}^- \\ &+\frac{1}{8}\left(\left[\frac{\epsilon}{\epsilon_R} - \frac{\mu}{\mu_R}\right] * \vec{G}^+\right) \cdot \vec{G}^- + \frac{1}{8}\left(\left[\frac{\epsilon}{\epsilon_R} + \frac{\mu}{\mu_R}\right] * \vec{G}^+\right) \cdot \vec{G}^-, \end{aligned} \tag{3.15}$$

(a fuller description can be found in [51]).

3.3 *Re-deriving Maxwell's equations

[1] In order to demonstrate the generality of *G-variables*, Maxwell's equations are now re-derived in terms of $G^{\pm}$ as presented in [34]. The two sourceless curl equations are

$$\nabla \times \vec{E} = -i\omega\tilde{\beta}^2\vec{H} \tag{3.16}$$

$$\nabla \times \vec{H} = +i\omega\tilde{\alpha}^2\vec{E}, \tag{3.17}$$

in frequency space. Multiplying eq(3.16) by "$\tilde{\alpha}_r$" and eq(3.17) by "$\tilde{\beta}_r\vec{u}\times$", followed by taking their sums and differences, yields

$$\nabla \times \tilde{\alpha}_R\vec{E} \pm \vec{u} \times (\nabla \times \tilde{\beta}_R\vec{H}) = -i\omega\tilde{\alpha}_R\tilde{\beta}^2\vec{H} \pm i\omega\tilde{\beta}_R\tilde{\alpha}^2\vec{u} \times \vec{E}. \tag{3.18}$$

The left hand side of eq(3.18) can be re-arranged to form the $\vec{G}^{\pm}$ of eq(3.5) using $\vec{u} \times (\nabla \times \vec{H}) = \nabla \times (\vec{u} \times \vec{H}) + \nabla(\vec{u} \cdot \vec{H})$:

$$\nabla \times \vec{G}^{\pm} = -i\omega\tilde{\alpha_R}\tilde{\beta}^2\vec{H} \pm i\omega\tilde{\beta_R}\tilde{\alpha}^2\vec{u} \times \vec{E} \mp \nabla(\vec{u} \cdot \tilde{\beta}_R\vec{H}). \tag{3.19}$$

At this point it is useful to manipulate the right hand side of eq(3.19) so that all the terms can be replaced by $\vec{G}^{\pm}$. Using the vector identity

$$\vec{H} = \vec{u} \times (\vec{u} \times \vec{H}) - (\vec{u} \cdot \vec{H})\vec{u} \tag{3.20}$$

eq(3.19) gives

$$\nabla \times \vec{G}^{\pm} = -i\omega(\tilde{\alpha}_R\tilde{\beta}^2\vec{u} \times (\vec{u} \times \vec{H}) - \tilde{\alpha_R}\tilde{\beta}^2(\vec{u} \cdot \vec{H})\vec{u} \mp \tilde{\alpha}^2\tilde{\beta}_R(\vec{u} \times \vec{E})) \mp \nabla G^o. \tag{3.21}$$

Using eq(3.8) and eq(3.9), eq(3.21) can be re-written as

$$\nabla \times \vec{G}^{\pm} = \mp i\omega\tilde{\alpha}_R\tilde{\beta}_R\vec{u} \times \vec{G}^{\pm} \mp \frac{i\omega\tilde{\alpha}_C\tilde{\beta}_R}{2}\vec{u} \times [\vec{G}^{+} + \vec{G}^{-}] - \frac{i\omega\tilde{\alpha}_R\tilde{\beta}_C}{2}\vec{u} \times [\vec{G}^{+} - \vec{G}^{-}] \tag{3.22}$$

where the following transverse components have been decoupled

$$\nabla G^o = \pm i\omega\tilde{\alpha}_R\tilde{\beta}_R\vec{u}G^o \pm i\omega\tilde{\alpha}_R\tilde{\beta}_C\vec{u}G^o. \tag{3.23}$$

To fully represent Maxwell's equations the transverse part of the time evolution of $\vec{E}$ must also be included, to correct for the cross-product "$\tilde{\beta} \quad \vec{u}\times$" applied to eq(3.17). For

[1] This re-derivation of Maxwell's equations can be omitted at first reading. A fuller version can be found in [51].

this reason $\nabla \cdot (\vec{u} \times \vec{H}) = \vec{u} \cdot (\nabla \times \vec{H})$ is added [34], where the correction term is

$$\nabla \cdot [\vec{G}^+ - \vec{G}^-] = -i\omega\tilde{\alpha}^2\tilde{\beta}_R\vec{u} \cdot [\vec{G}^+ + \vec{G}^-]. \tag{3.24}$$

Thus eq(3.22), eq(3.23) and eq(3.24) are Maxwell's equations (eq(3.16) and eq(3.17)) re-written in terms of *G-variables*.

Moving frame

As computational efficiency remains one of the key motivations for applying *G-variables*, a moving frame transformation is now applied. A number of choices are possible

- **Phase velocity of central frequency**. This has the advantage of freezing the carrier oscillations, allowing coarser sampling. The pulse will however walk away from the centre of the time window because of the difference in group velocity.
- **Group velocity**. This choice has the advantage of retaining the pulse in the centre of the window, but the carrier oscillations move in this frame of reference.
- **Dispersive frame**. This choice is composed of a set of reference frames, where each frequency component has its own respective reference frame (moving at its phase velocity).

The following represents a moving frame transformation:

$$t' = t - \gamma/c_f \tag{3.25}$$

$$\vec{r}' = \vec{r}, \tag{3.26}$$

where γ is the distance travelled in the direction of $\vec{u}$, and $c_f = 1/\alpha_f\beta_f$ is the speed of the moving frame at a particular frequency. (α_f and β_f are the moving frame parameters at a particular frequency which can be made to be dispersive.) The partial derivatives now become

$$\partial_t = \partial_{t'} \tag{3.27}$$

$$\nabla = \nabla' - \frac{\vec{u}}{c_f}\partial_t.$$

Transforming eq(3.22) into a moving frame gives

$$\nabla' \times \vec{G}^{\pm} = \tag{3.28}$$
$$\mp i\omega\tilde{\alpha}_R\tilde{\beta}_R(1-\zeta)\vec{u}\times\vec{G}^{\pm} \mp \frac{i\omega\tilde{\alpha}_C\tilde{\beta}_R}{2}\vec{u}\times[\vec{G}^{+}+\vec{G}^{-}] - \frac{i\omega\tilde{\alpha}_R\tilde{\beta}_C}{2}\vec{u}\times[\vec{G}^{+}-\vec{G}^{-}],$$

where

$$\zeta = \frac{\alpha_f\beta_f}{\alpha_R\beta_R}. \tag{3.29}$$

A particularly compact choice for the moving frame velocity is $\alpha_R\beta_R$, as it removes the first term on the right hand side of eq(3.28). However, making the moving frame dispersive can be problematic in nonlinear environments because of nonlinear dispersion. Dispersive moving frames are also less intuitive and less computationally stable than simpler moving frames. It is important to note the trade off in efficiency here; though a co-moving frame assists the integration of G^{+}, it impedes it for a backward propagating G^{-}, as the field travels at twice the speed in the opposite direction. A speed-up is therefore attainable if only G^{+} fields are used.

3.4 Coupled $G^{\pm}$

Having re-derived Maxwell's equations in the previous section, the use of $G^{\pm}$ as an alternative direct Maxwell solver now forms the focus of the remainder of the chapter. To begin, we consider the case of plane polarised fields travelling in the $+z$ direction of a non-magnetic material. Eq(3.22) can now be written as

$$\partial_z G^{\pm} = \mp i\omega\tilde{\alpha}_R\tilde{\beta}_R(1-\zeta)G^{\pm} \mp \frac{i\omega\tilde{\alpha}_C\tilde{\beta}_R}{2}[G^{+}+G^{-}]. \tag{3.30}$$

3.4.1 Vacuum reference

To illustrate the use of $G^{\pm}$, a vacuum reference $\alpha_R = \sqrt{\epsilon_0}$ is chosen for a general case of linear dispersion and arbitrary instantaneous nonlinearity. The choice of a vacuum reference does not match the permittivity of the material, producing a significant co-propagating G^{-}. The correctional part of the permittivity can be separated into linear

and nonlinear components. Thus

$$\begin{aligned}\tilde{\epsilon}(\omega) &= \tilde{\epsilon}_R(\omega) + \tilde{\epsilon}_L(\omega) + \tilde{\epsilon}_{NL}(\omega) \\ &= \tilde{\alpha}_R^2 + \tilde{\alpha}_R\tilde{\alpha}_L + \tilde{\alpha}_R\tilde{\alpha}_{NL},\end{aligned} \tag{3.31}$$

results in the following nonlinear propagation terms

$$\partial_z G^{\pm} = \mp\alpha_0\beta_0 \left(\partial_t G^{\pm} + \frac{\chi^{(1)}}{2}[G^+ + G^-] + \frac{\chi^{(2)}}{4\alpha_0}[G^+ + G^-]^2 + \frac{\chi^{(3)}}{8\alpha_0^2}[G^+ + G^-]^3 + ... \right). \tag{3.32}$$

The advantage of using dispersionless reference parameters lies in the simplicity of the integration method. In order to calculate the nonlinearity, E must somehow be retrieved from $G^{\pm}$. If $G^{\pm}$ was constructed from dispersionless reference parameters, this is simply: $E(t) = \frac{G(t)^+ + G(t)^-}{2\alpha_R}$. On the other hand, if a dispersive reference was used, either some approximation or a deconvolution becomes necessary. Unfortunately, the disadvantage of using a dispersionless reference (especially a vacuum) is that the magnitude of the co-propagating G^- can be too large to ignore. To illustrate the effect of the reference, assume the following pulse:

$$E(t) = E_0 \cos(\omega_0 t + \phi)\,\mathrm{sech}(0.15\omega_0 t) \tag{3.33}$$

where $\omega_0 = 1.52 \times 10^{15}$ rad s^{-1} (1240 nm wavelength). A vacuum reference $\alpha_R = \sqrt{\epsilon_0}$ produces the $G^{\pm}$ combination in fused silica and can be seen in fig 3.1, highlighting the significance of the G^- field.

A compromise for α_R that substantially reduces G^- without the complications of dispersion, is the partially matched reference described in the next section.

3.4.2 Partially matched reference

Indeed a number of choices exist to partially match the material dispersion. One of these is the average permittivity of the host medium over the spectral domain of interest (see eq(3.7)). In order to ensure numerical stability in the simulations, the relative permittivity $\epsilon_r(\omega)$ was held in the range $(1 \leqslant \epsilon_r < 7)$. Though in general the Kramers-Kronig relationship describing the real and imaginary parts of the linear response should enforce this, we found that a permittivity of more than $\simeq 7$ led to numerical instability even when including the imaginary component. The real part of the permittivity was thus bounded, and the imaginary component set to zero. The average $\epsilon_r(\omega)$ over the

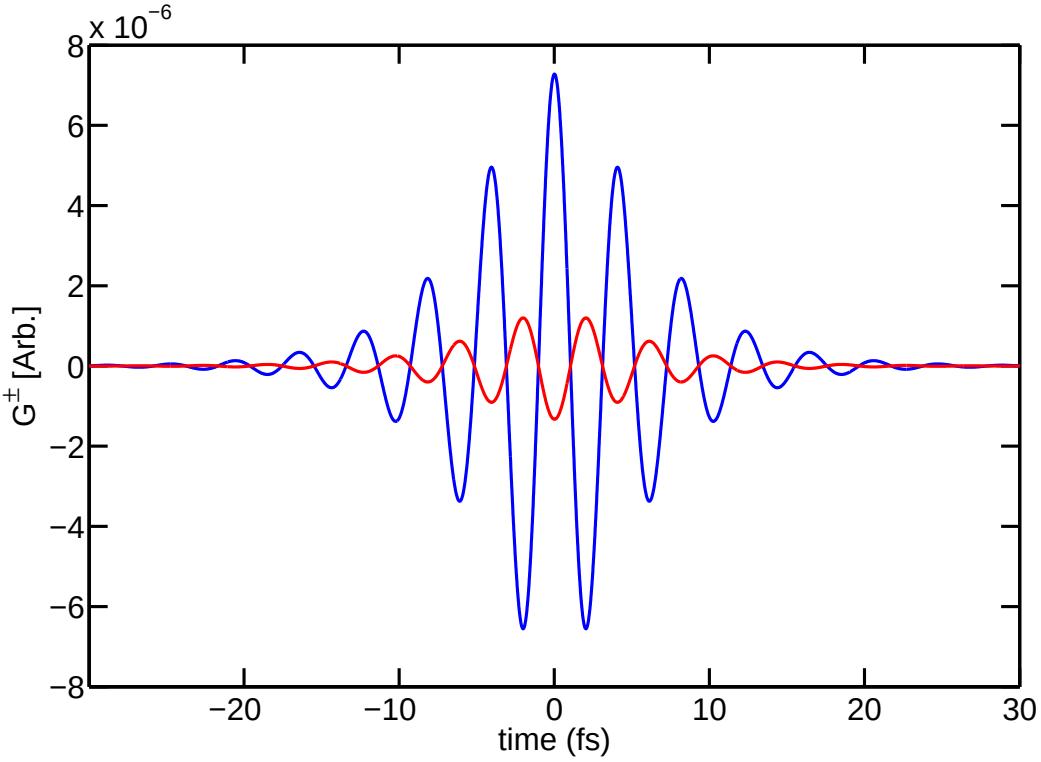

Figure 3.1: $\alpha_R = \sqrt{\epsilon_0}$. Vacuum reference in fused silica. The blue and red pulses represent G^+ and G^- respectively. The large G^- can clearly be seen in the figure.

entire frequency domain was used to determine ϵ_{av}. For fused silica $\epsilon_{av} \approx 2.7\epsilon_0$. This choice significantly reduced G^-, but a noticeable co-propagating G^- still remained. Fig 3.2 shows, $G^{\pm}$ for $\alpha_R = \alpha_{av} = \sqrt{\epsilon_{av}}$

Though α_{av} undoubtedly reduces the co-propagating G^-, it does not adequately weigh the contributions of the relative permittivity, because most of the pulse energy is contained in the region closest to the central frequency. Fig 3.3 plots the Sellmeier equation of fused silica $\epsilon_r(\omega)$, across the pulse bandwidth.

An improved choice for α_R, is $\alpha_R = \sqrt{\epsilon_0\epsilon_r(\omega_0)}$, reducing the magnitude of the co-propagating G^- further still. In such a case (fused silica), perhaps the size of G^- is small enough to be ignored? Later we discuss the contexts in which this assumption is valid. Fig. 3.4 shows $G^{\pm}$ for $\alpha_R = \sqrt{\epsilon_0\epsilon_r(\omega_0)}$.

In this case, the terms arising during propagation from a dispersionless reference are

$$\partial_z G^{\pm} = \mp\alpha_R\beta_0\left(\partial_t G^{\pm} + \left(\frac{\epsilon_0\epsilon_r}{\epsilon_R} - 1\right)\frac{[G^+ + G^-]}{2} + \sum_n \frac{\epsilon_0\chi^{(n)}}{2^n\alpha_R^{n+1}}[G^+ + G^-]^n\right). \quad (3.34)$$

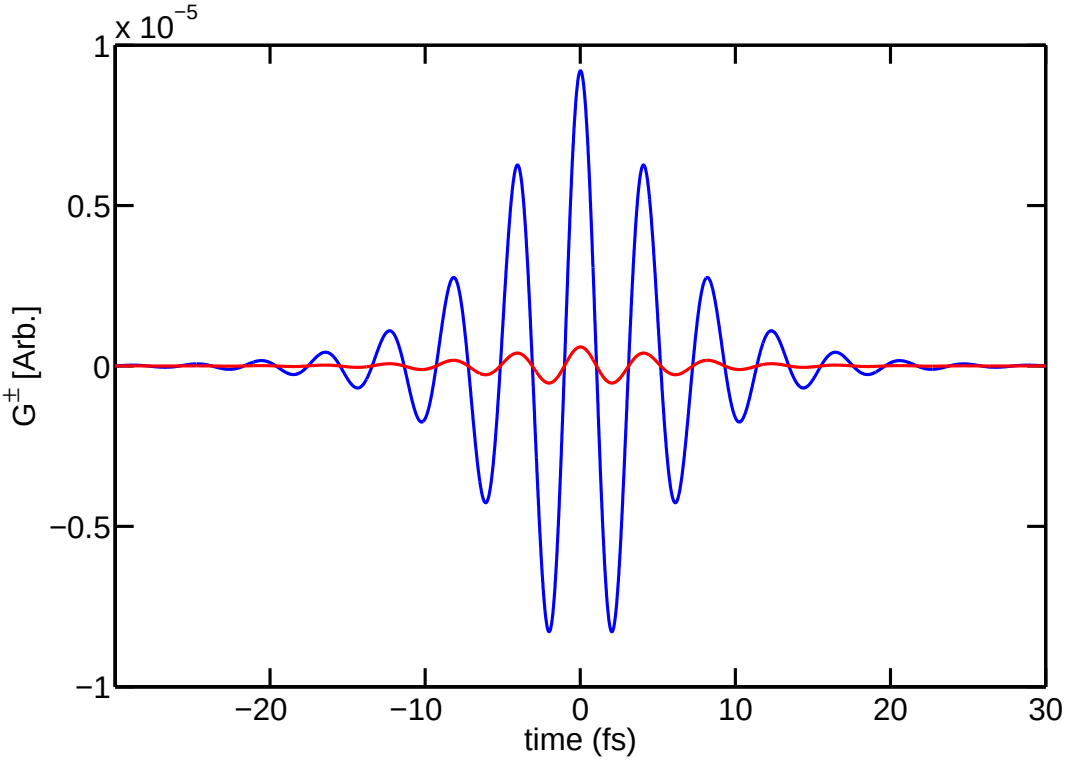

Figure 3.2: $\alpha_{av} = \sqrt{\epsilon_{av}\epsilon_0} = \sqrt{2.70\epsilon_0}$. G^- has been significantly reduced, but remains visibly present. Note that the G^- in this case is in phase with G^+.

3.4.3 Dispersive reference

Though in some cases a well chosen dispersionless reference may suffice, to completely match $\epsilon_r(\omega)$, the full dispersion must be included. Fig 3.5 shows how a perfectly matched reference permittivity completely removes the co-propagating G^- field.

The result of using dispersion to construct $G^{\pm}$ is that the linear correction term in eq(3.34) goes to zero, leaving only the nonlinear correction terms. Because G^- is initially zero, a forward only approximation can be justified as long as no significant amount of G^- is produced during a simulation. The forward-only approximation uses *only* G^+ to describe the nonlinear propagation.

There are however some disadvantages of using a dispersive reference. In the case of a dispersionless reference, the nonlinearity can simply be calculated in time: $E^n \rightarrow (\frac{G^+(t)+G(t)^-}{2\alpha_R})^n$. However, in the case of a dispersive reference, any time domain nonlinearity is no longer trivial as $\alpha_R * E(t)$ is a convolution in time. An FT is then needed to deconvolve $\alpha_R(\omega)$ from $\tilde{G}(\omega)$, before performing another FT: $E(t)^n \rightarrow (\mathcal{F}^{-1}[\mathcal{F}[G^+(t) + G(t)^-] \cdot \frac{1}{2\tilde{\alpha}_R(\omega)}])^n$. This procedure adds an extra FT to the integration, which increases

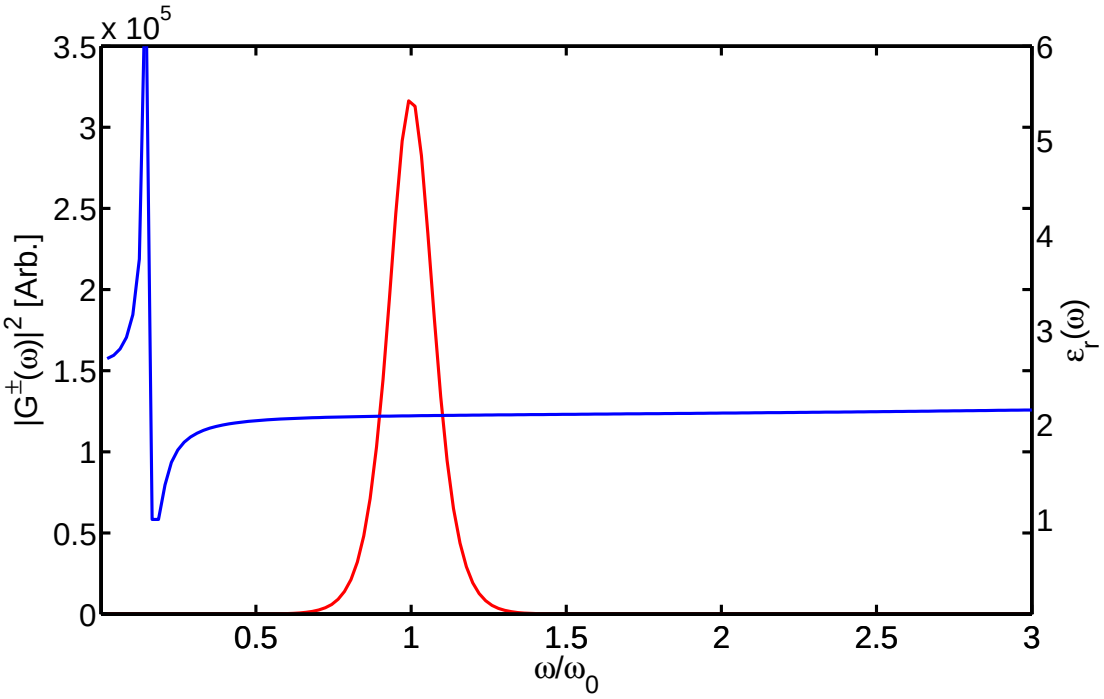

Figure 3.3: Sellmeier equation plotted for fused silica, as a function of frequency (blue). The initial pulse bandwidth, and permittivity have also been plotted (red) for comparison.

the simulation run time by at least a third after making a forward-only approximation.

3.5 Numerical approach

The practicalities of using *G-variables* as a numerical method are now compared to the PSSD method. In PSSD [32], initial conditions are stored in time and the simulation marches forward in space. The two-fold advantage of PSSD lies in the combination of both the natural application of linear dispersion and the N^{th} order accurate derivative taking place within the same computational operation (namely $\partial_t P$). The nonlinear response is assumed to be instantaneous, and is therefore calculated in time. Fig 3.6 describes the PSSD method with a flow diagram, where the standard PSSD simulation requires five F.T.s.

The *G-variables* method shares many similarities with PSSD, since they exploit the same time saving steps. Like PSSD, the initial conditions are defined in time and the simulation marches forward in space. The combination of a pseudo-spectral derivative with the linear dispersion calculation also takes place. Unlike PSSD however, the simulation

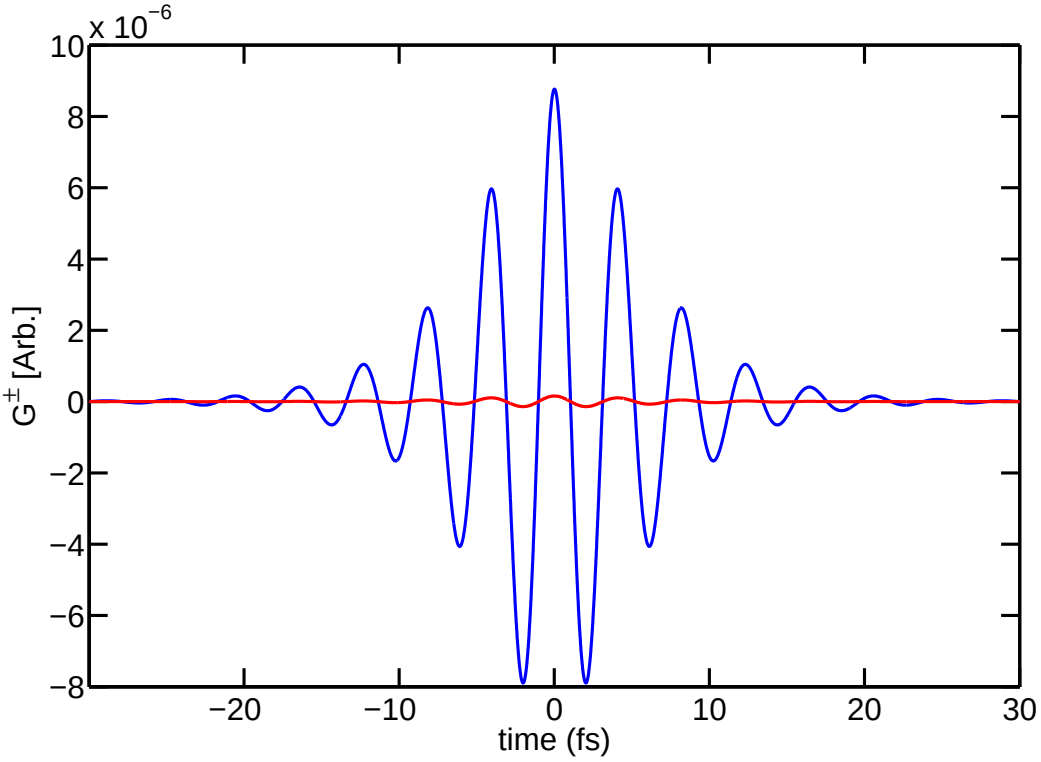

Figure 3.4: $\alpha_R = \sqrt{\epsilon_0 \epsilon_r(\omega_0)}$ for fused silica. A very significant reduction of G^- can be seen, even with the application of a dispersionless reference parameter.

uses the co-located G^+ and G^- fields to integrate forward in space using a staggered leap frog method. Fig 3.7 describes the computational steps involved in a coupled *G-variables* simulation, where a dispersive reference has been used.

The PDE used to calculate the propagation of $G^\pm$ using dispersive references is the same as eq(3.34), except that an extra FT is necessary to deconvolve the dispersive reference. The choice of reference parameters greatly influences the approximations that can be applied. Table 3.1 summarises the differences between various parameter choices, and how they affect the computation.

No approximations have been made at this stage, meaning that the coupled *G-variables* method is comparable in computational speed to PSSD. The forward only approximation must be invoked in order to exercise any computational advantage, and this is the topic of chapter IV.

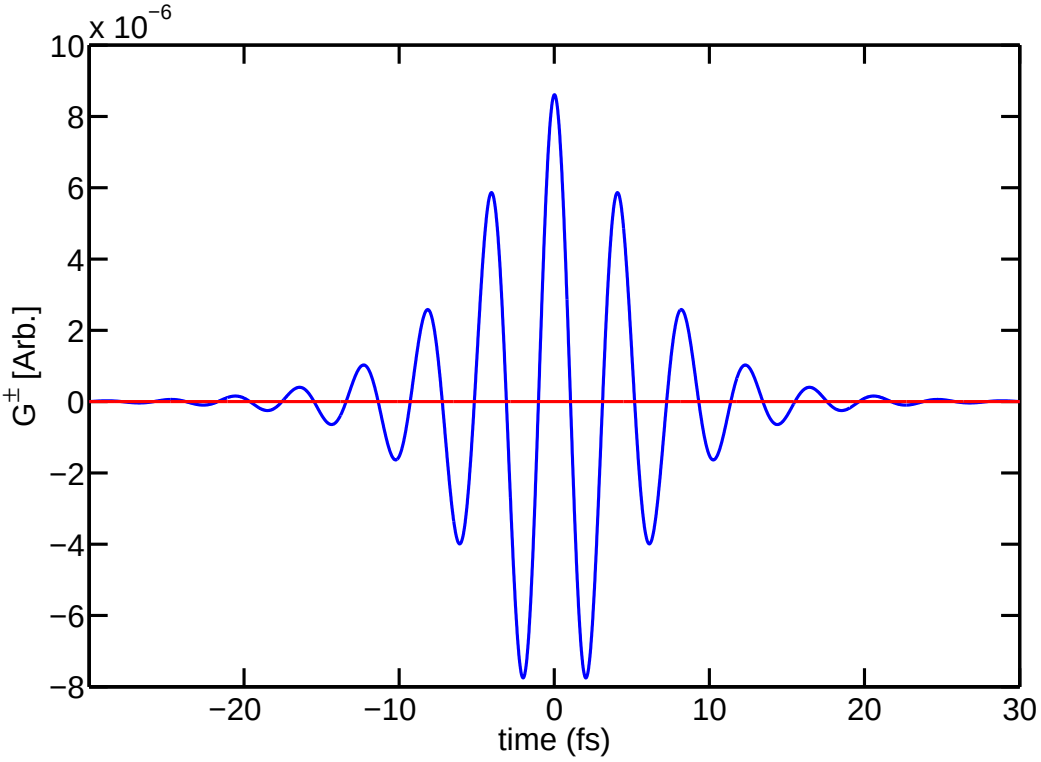

Figure 3.5: $\alpha_R = \sqrt{\epsilon_0 \epsilon_r(\omega)}$. G^- is now zero (red) with a perfectly matched reference permittivity. The G^+ field (blue) fully describes the pulse in this case.

Table 3.1: Comparison of reference parameters (α_R)

Reference	Vacuum reference $\alpha_R = \sqrt{\epsilon_0}$	Partially matched reference $\alpha_R = \kappa\sqrt{\epsilon_0}$	Dispersive reference $\alpha_R = \sqrt{\epsilon_0 \epsilon_r(\omega)}$
$G^{\pm}$ Definitions	Dispersionless	Dispersionless	Dispersive
G^- :	Significant	Sometimes significant	Negligible
Nonlinearity:	No deconvolution req.	No deconvolution req.	Deconvolution req.
Number of FTs req.:	5	5	6
Possibility of G^+	No	Under certain conditions	Yes

Initial conditions

Initial conditions play an important role in the definition and computation of $G^{\pm}$. The information present at the beginning of a simulation is $E(t)$ and the material dispersion $\tilde{\epsilon}(\omega)$. For any EM pulse to propagate forward, E and H must be accurately matched to each other. If not, a backward propagating pulse emerges, analogous to a reflection from

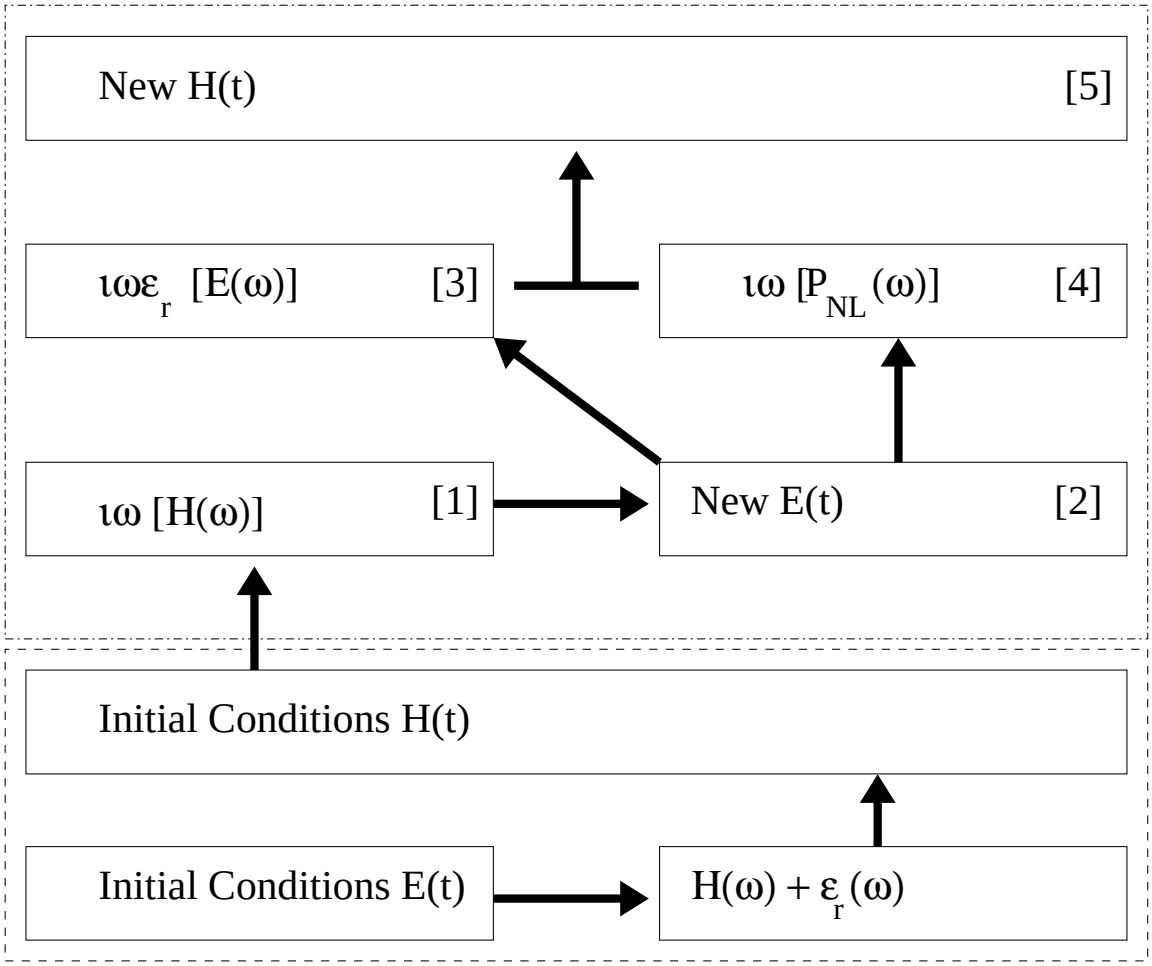

Figure 3.6: Flow diagram of the computational steps in a standard PSSD calculation. Starting from $E(t)$ and $\epsilon_r(\omega)$ (bottom), $H(t)$ can be constructed. The initial conditions are in the dashed box at the bottom of the figure. Note the square brackets '[ ]', indicate the number of Fourier Transforms used in the iteration step.

an interface. To avoid this, the following relationship is used

$$H(t) = \mathcal{F}^{-1}\left[\sqrt{\frac{\epsilon_0 \tilde{\epsilon}_r(\omega)}{\mu_0}} \quad \mathcal{F}[E(t)]\right], \tag{3.35}$$

where $\tilde{\epsilon}_r(\omega)$ is the material dispersion [32], and the initial conditions have been chosen to describe a forward only propagating pulse. Backward-propagating G^- waves only arise from mismatched initial conditions, interfaces or very strong nonlinearity. (This contrasts to co-propagating G^- waves that occur in cases where reference parameters are not well suited to the linear dispersion.) After deriving H, the choice of reference (parameter)

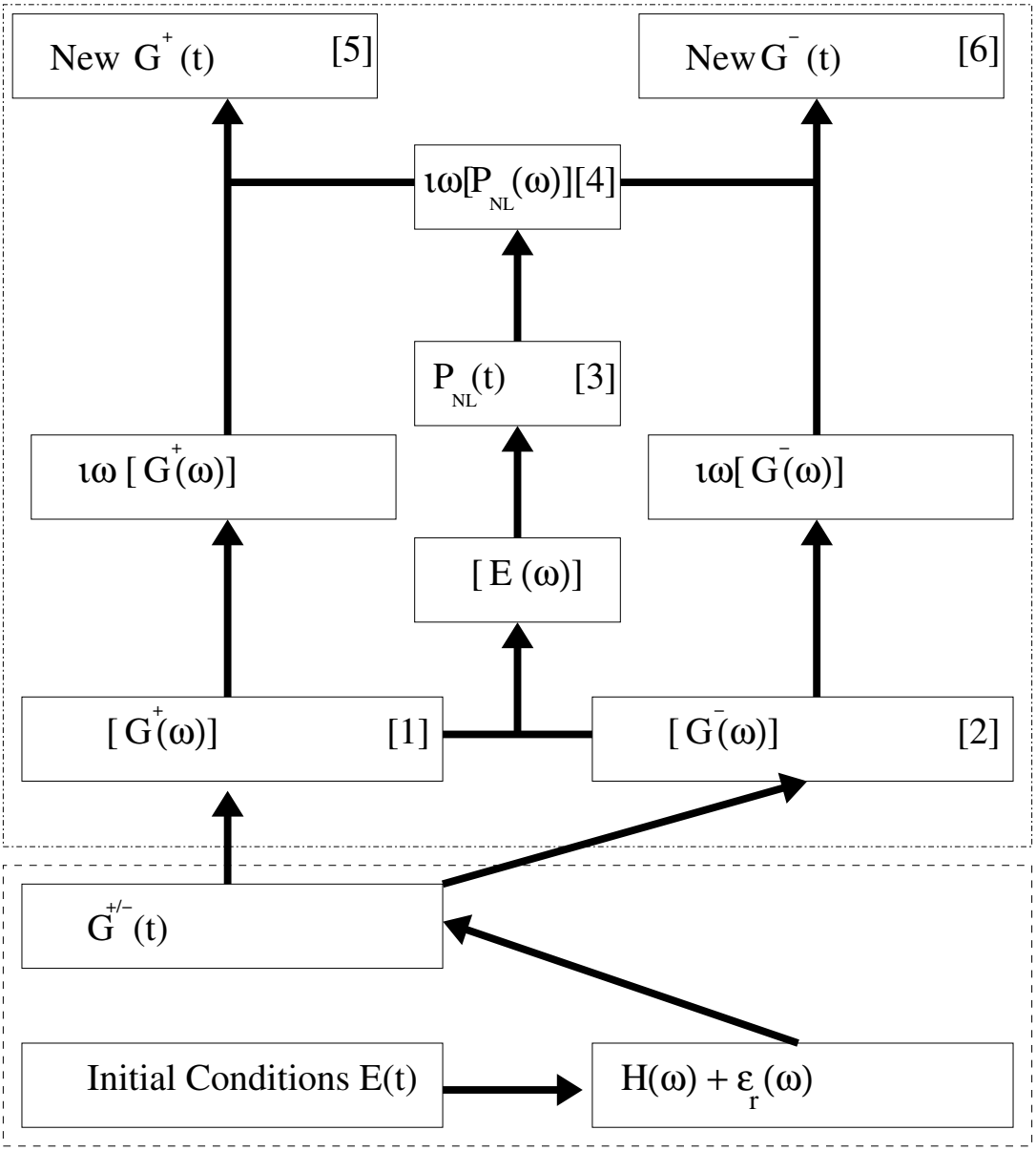

Figure 3.7: Flow diagram of the computational steps involved in a coupled $G^{\pm}$ simulation. Starting from $E(t)$, and $\epsilon_r(\omega)$, $G^{\pm}$ can be constructed. The initial conditions are in the dashed box at the bottom of the figure. Note the square brackets '[ ]', indicate the number of Fourier Transforms used.

permittivity is made. A dispersionless reference is applied in time, as follows:

$$G(t)^{\pm} = \sqrt{\epsilon_R}E(t) \pm \sqrt{\mu_R}H(t), \tag{3.36}$$

whereas a dispersive reference is applied in the frequency domain

$$G(t)^{\pm} = \mathcal{F}^{-1}\left[\sqrt{\tilde{\epsilon}_R(\omega)}\mathcal{F}[E(t)] \pm \sqrt{\tilde{\mu}_R(\omega)}\mathcal{F}[H(t)]\right]. \tag{3.37}$$

3.6 Results

This section presents results from simulations involving $G^{\pm}$. Two examples are included to demonstrate the application of *G-variables* to nonlinear problems; nonlinear propagation in fused silica, and SHG in periodically poled lithium niobate. This emphasises the importance of reference parameters, and their effect on the magnitude of G^{-}. In these cases the G^{-} field that is produced is mostly co-propagating, and occurs from mismatches between α_R and the material dispersion.

3.6.1 Propagation in fused silica: $\chi^{(3)}$

The first example involves a $\sim$ 6 fs pulse propagating in fused silica over a distance of 40 microns ($\lambda_0 = 1240$ nm) in the presence of a $\chi^{(3)}$ nonlinearity ($\chi^{(3)}E_0^2 = 0.02$). Fig. 3.8 shows the initial pulse where a perfectly matched reference has been used for clarity (only G^{+} is present). It is useful to refer to the dispersion profile of fused silica (fig. 3.3), when considering a choice for α_R.

The various $G^{\pm}$ combinations at the end of the propagation can be seen in fig. 3.8, where the following reference parameters were used: $\alpha_R = \sqrt{\epsilon_0}$, $\alpha_R = 1.5\sqrt{\epsilon_0}$, $\alpha_R = \sqrt{\epsilon_0\epsilon_r(\omega_0)}$, and $\alpha_R = \sqrt{\epsilon_0\epsilon_r(\omega)}$. $\alpha_R = \sqrt{\epsilon_0}$ produces the largest G^{-}, due to it having the largest difference with the material dispersion, especially at the central frequency (ω_0). $\alpha_R = 1.5\sqrt{\epsilon_0}$ reduces G^{-} considerably, because its reference partially matches that of the medium. $\alpha_R = \sqrt{\epsilon_0\epsilon_r(\omega_0)}$ almost completely removes G^{-} as does $\alpha_R = \sqrt{\epsilon_0\epsilon_r(\omega)}$.

Surprisingly there is little difference between $\alpha_R = \sqrt{\epsilon_0\epsilon_r(\omega_0)}$, and $\alpha_R = \sqrt{\epsilon_0\epsilon_r(\omega)}$. This is because most of the energy is present around the central frequency, and thus any discrepancy between α_R and $\sqrt{\epsilon_0\epsilon_r(\omega)}$ corresponds to a very small energy contribution. The minuscule G^{-} in the case $\alpha_R = \sqrt{\epsilon_0\epsilon_r(\omega)}$, arises during the propagation, and is generated from the nonlinear driving term; the coupling of G^{+} with G^{-}. Though it is easy to factorise linear dispersion into α_R, it is impossible to do so for nonlinear dispersion. This is not generally a problem given the trivial size of G^{-}.

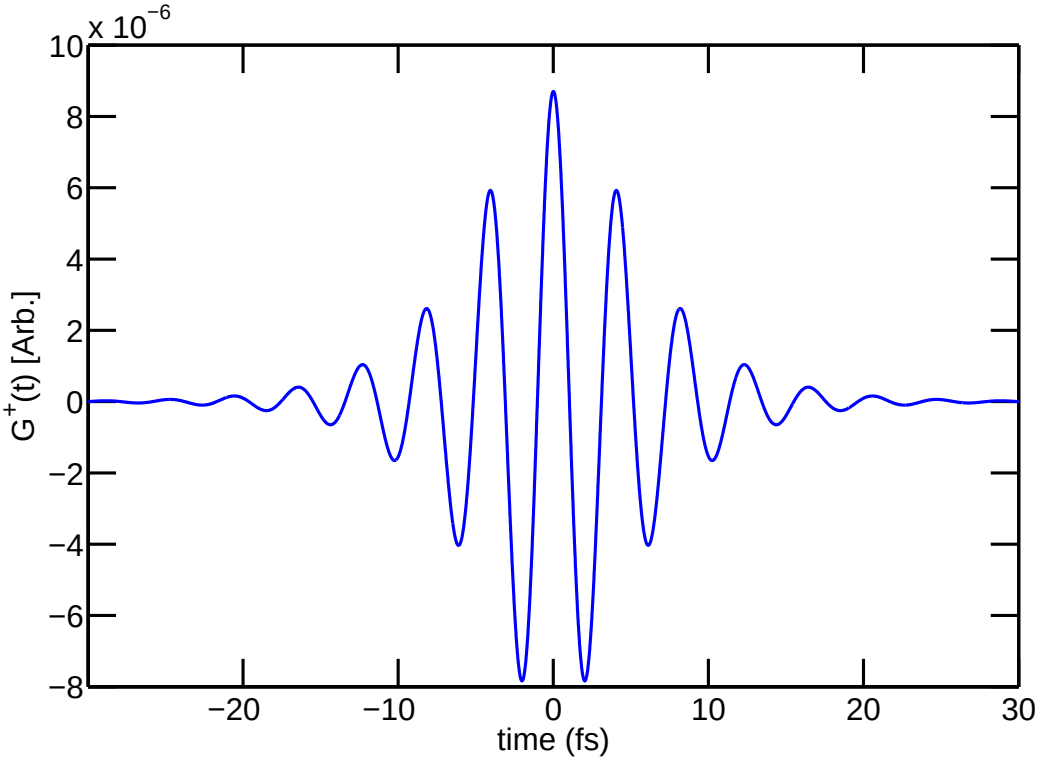

Figure 3.8: Initial pulse used in the propagation, where $\alpha_R = \sqrt{\epsilon_0 \epsilon_r(\omega)}$.

3.6.2 SHG in lithium niobate: $\chi^{(2)}$

Results from the propagation of *G-variables* in periodically poled lithium niobate are now presented, where a plane polarised field is assumed. The polarisation of the second harmonic is the same as the driving field, as lithium niobate supports $e + e \rightarrow e$ interactions [46]. The initial pulse has a ∼10 fs duration at a central wavelength of $\lambda_0 = 1400$ nm.

During the 100 micron propagation, a second harmonic field was generated through Quasi-Phase Matching (QPM). Fig. 3.10 shows the growth of the second harmonic during the propagation, and the final spectrum ($\alpha_R = \sqrt{\epsilon_0 \epsilon_r(\omega)}$ ensures no G^- present).

The final pulse contains a significant amount of second harmonic and is illustrated in fig. 3.11, where it has travelled slower than the fundamental because of normal dispersion. The reference parameter choices used here were $\alpha_R = \sqrt{\epsilon_0}$, $\alpha_R = \sqrt{\epsilon_0 \epsilon_r(\omega_0)}$, and $\alpha_R = \sqrt{\epsilon_0 \epsilon_r(\omega)}$.

As expected, the results show that using a vacuum reference produces the largest co-propagating G^-, whilst using a partially or fully matched reference parameter reduces it.

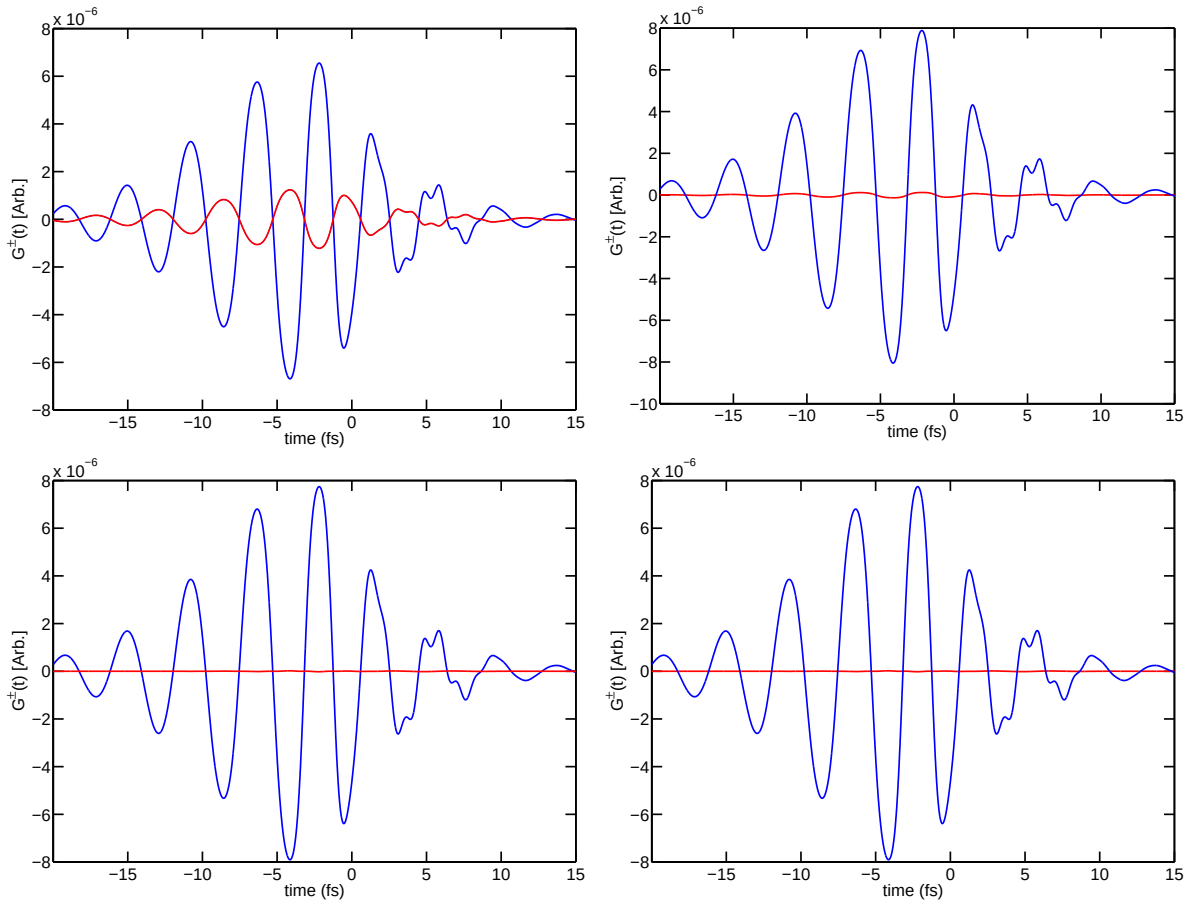

Figure 3.9: 40 micron propagation through fused silica with different reference parameters.(top-left) $\alpha_R = \sqrt{\epsilon_0}$ produces the largest G^- field. (top-right) $\alpha_R = 1.5\sqrt{\epsilon_0}$ reduces G^- significantly. (bottom-left) $\alpha_R = \sqrt{\epsilon_0\epsilon_r(\omega_0)}$ almost completely removes G^-, by matching the medium at the central frequency. (bottom-right) $\alpha_R = \sqrt{\epsilon_0\epsilon_r(\omega)}$ almost completely removes G^-. The minuscule quantity remaining arises from the nonlinear propagation itself, and is impossible to remove.

Like the case of fused silica, choosing $\alpha_R = \sqrt{\epsilon_0\epsilon_r(\omega_0)}$ almost completely removes G^-. This is surprising at first, because the dispersion profile of lithium niobate varies more than fused silica. However, looking at $\epsilon_r(\omega)$ in the vicinity of ω_0 (see fig. 3.12), suggests that choosing $\alpha_R = \sqrt{\epsilon_0\epsilon_r(\omega_0)}$ will provide a good match, as the profile there is relatively flat.

These results demonstrate that *G-variables* can be as versatile as more traditional direct Maxwell solvers (PSSD) when applied to nonlinear pulse propagation. They also strongly suggest that well chosen dispersionless reference parameters reduce the co-propagating G^- almost as much as dispersive references. This leads to the potential computational gains of applying a dispersionless reference to a forward-only approxima-

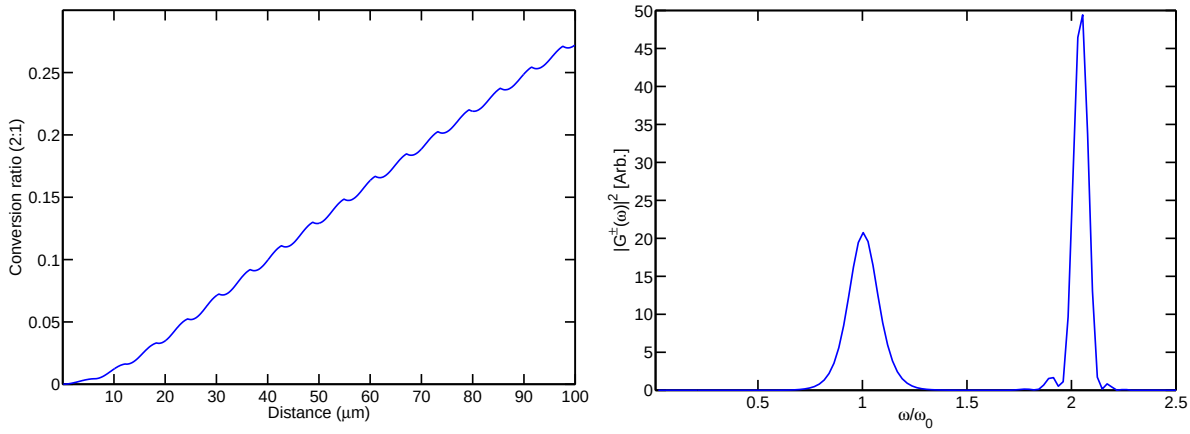

Figure 3.10: QPM in periodically poled lithium niobate where the poling period is 12.2 microns (effective nonlinear strength $bE_0 = 0.01$). (left) Generation of second harmonic during propagation. (right) Final intensity spectrum for G^+, where a significant amount of second harmonic can be seen.

tion.

3.7 Backward-propagating G^-

So far, the G^- fields considered have been co-propagating. These fields move with the forward going G^+ pulse, and are present in order to describe the E and H fields. They are G^-, by virtue of their flux being directed in the $-z$ direction. We have shown that through a careful choice of reference parameters, the co-propagating G^- fields can be almost completely removed. It is also clear from section 3.6 that under normal conditions, no significant backward propagating G^- fields are generated over the course of a simulation.

There are however G^- fields, that not only point, but also travel in the $-z$ direction. These fields are commonly discarded in simulations or removed with the assumptions underlying a uni-directional model. By using *G-variables* it is possible to evaluate their magnitude. There are two ways in which a backward travelling wave may be produced:

- **Boundary conditions**. If the E and H fields are not properly matched a backwards travelling wave will be generated. This commonly occurs in the first steps of a simulation, or when a pulse strikes a boundary.

- **Strong nonlinearity**. Even if a pulse is well constructed (i.e. E and H are perfectly matched to the medium at the outset), a G^- field can be generated through the nonlinear coupling of G^+ with G^-. This is claimed in [57] where backward generated second harmonic fields are predicted under certain conditions (see section

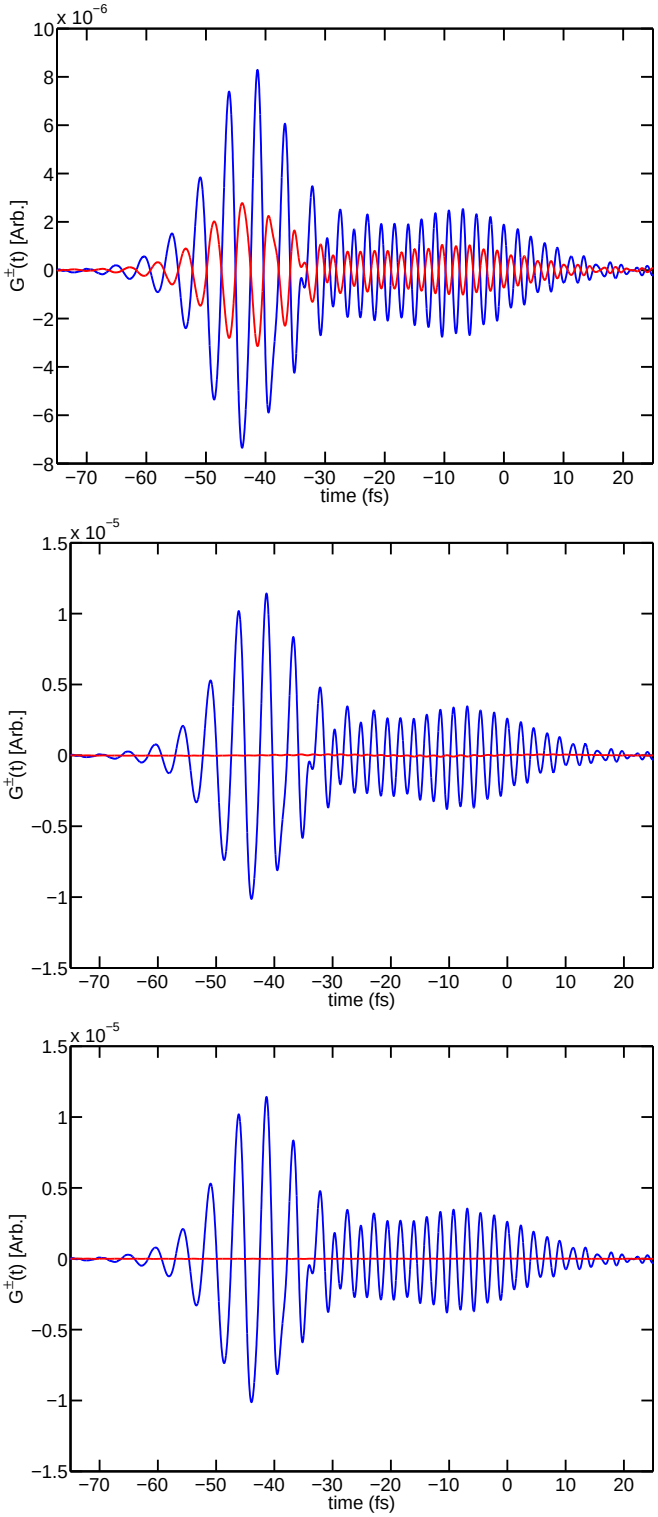

Figure 3.11: $G^{\pm}$ after 100 micron propagation in periodically poled lithium niobate. (top) $\alpha_R = \sqrt{\epsilon_0}$ produces the largest G^{-}. (middle) and (bottom) $\alpha_R = \sqrt{\epsilon_0 \epsilon_r(\omega_0)}$ and $\alpha_R = \sqrt{\epsilon_0 \epsilon_r(\omega)}$ (respectively), almost completely remove G^{-}. The results qualitatively agree with those from fused silica.

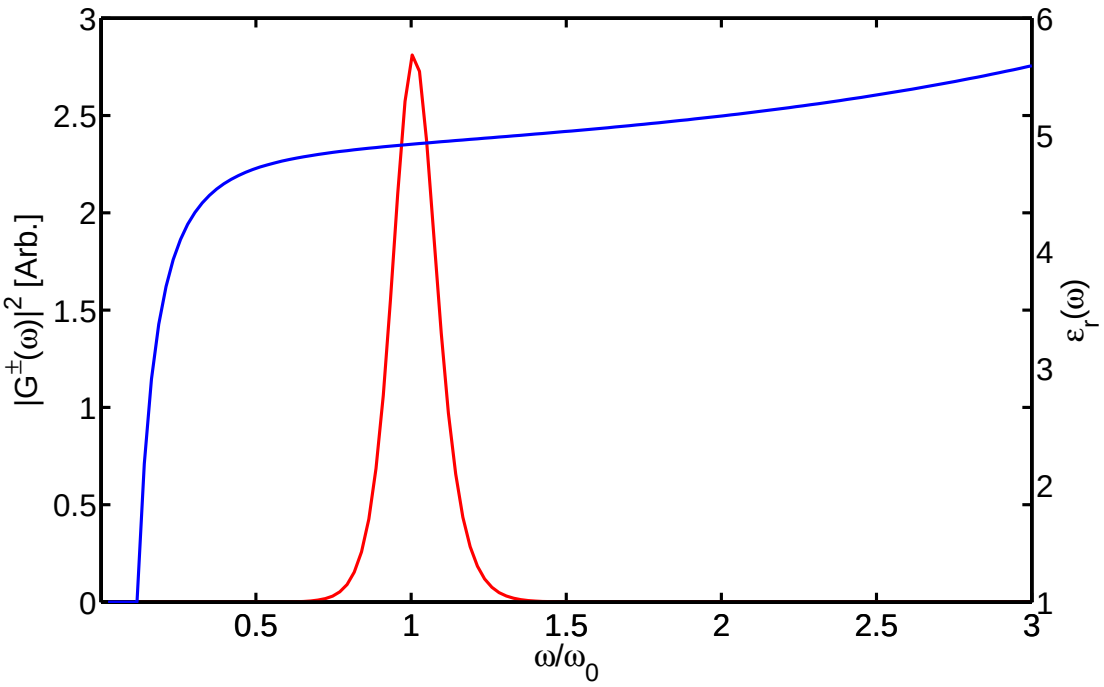

Figure 3.12: Sellmeier equation for lithium niobate ($\epsilon_r(\omega)$). The bandwidth of the initial pulse can be seen in the figure (red).

3.7.2 below).

3.7.1 Boundary conditions

To demonstrate the effects of backward propagating fields (from an interface), a pulse striking a refractive index boundary ($\epsilon_r = 1.5$) was modelled. Fig. 3.13 shows the $G^{\pm}$ fields generated in this situation where a sudden change in ϵ_r, has produced a backward propagating G^{-} field.

Mis-matched initial E and H fields produce the same effect. By carefully deriving the H field from the E field and avoiding interfaces, the production of this type of backward propagating G^{-} field can be avoided.

3.7.2 Nonlinearly generated G^{-}

It was claimed in [57] that under certain conditions, Second Harmonic Generation (SHG) in the backward direction is possible. These conditions attempt to quasi phase-match the second harmonic in the backward direction. Following the parameters outlined in [57],

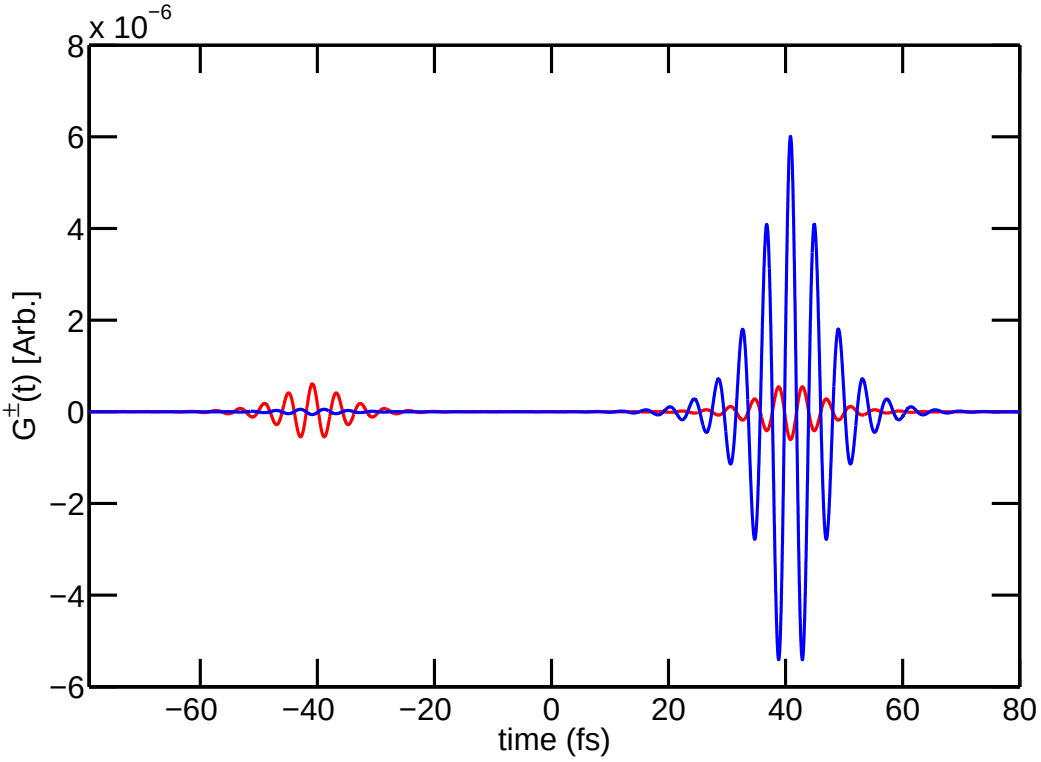

Figure 3.13: Partial reflection produced by a pulse striking an interface ($\epsilon_r = 1.5$).

simulations using PSSD were carried out. A pulse with a peak intensity of 10^{12} W/cm^2 and a central wavelength of 800 nm was used for driving the backwards SHG. The $\chi^{(2)}$ medium was lithium niobate with a poling period of 0.19 μm. During the simulation, the pulse propagated 6 microns experiencing QPM, followed by a further 30 microns without any second-order nonlinearity. The latter part of the propagation was performed to produce well separated $G^{\pm}$ fields. In this case, $G^{\pm}$ were artificially reconstructed at the end of the simulation using dispersive references and can be seen in fig. 3.14.

The nonlinearity in any propagation drives both the G^+ and G^- fields, since it depends on E, which contains both G^+ and G^-. Due to the lack of phase-matching in the backward direction, the magnitude of backward propagating G^- fields remain close to zero (typically one part in 10^6). Only in exceptional cases such as [57], can any significant field be generated.

The results of this chapter clearly indicate that in nearly all cases, G^- can be forced to play a small part. This applies to both backward propagating G^- fields, and those that are co-propagating. Backward-propagating fields can be avoided by matching E to H and avoiding interfaces, whereas co-propagating G^- fields can be eliminated by matching the reference parameters to the linear dispersion of the medium. The only exception being

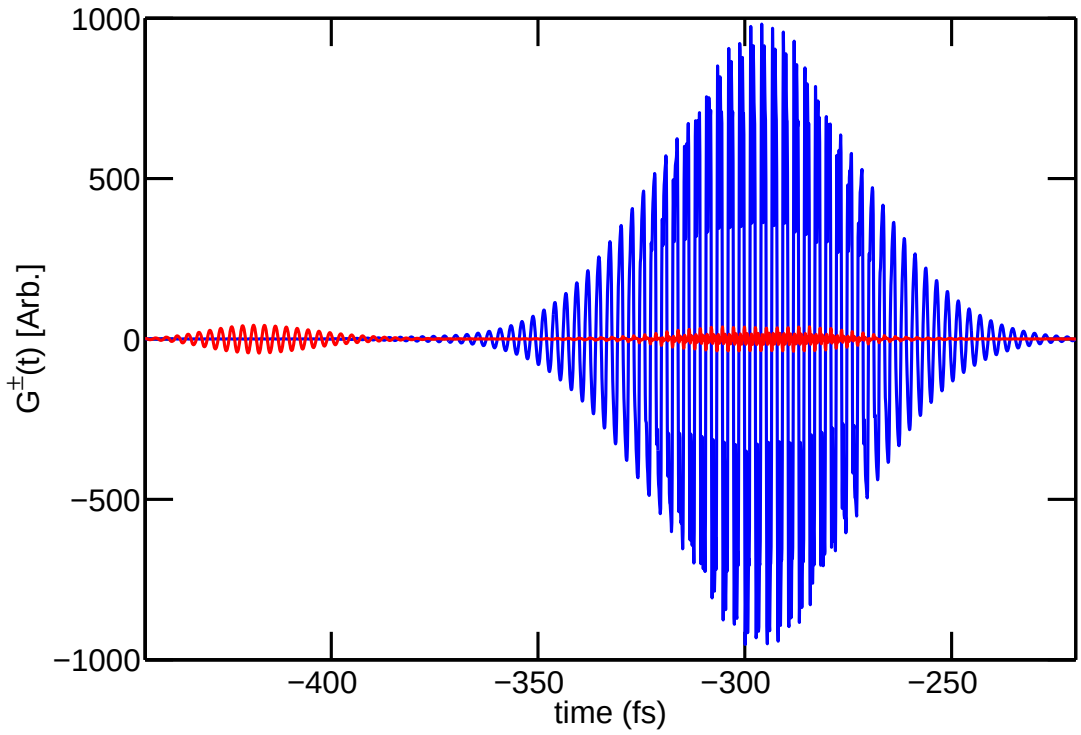

Figure 3.14: Backward generated fields. The poling period (lithium niobate) was optimised for QPM in the backwards direction, and has generated a backward propagating G^- field containing some second-harmonic.

the highly unusual case of QPM in the backward direction. As this is more of an anomaly than a general result, a forward-only approximation appears possible, and is the topic of the next chapter.

It is also worthwhile noting that the lack of backward propagating G^- fields also circumvents any problems arising from waves travelling in the 'wrong' temporal direction. As the initial conditions of any 'tk' or 'tz' simulations are stored in time, any backward propagating wave appears to travel backwards in time [34]. This is merely the way the simulation represents a wave travelling in the $(-z)$ direction, but should nonetheless be noted.

3.8 Conclusion

The directional *G-variables* have been introduced in this chapter. They allow an EM field to be separated into forward and backward components, where *forward* and *backward* refer to the direction of the EM flux. By generalising the $G^\pm$ definitions, Maxwell's

equations can be re-derived, and a variety of different reference parameters become possible, which can either be dispersive or dispersionless. These reference parameters control the relative magnitudes of any co-propagating $G^{\pm}$ pair. The co-propagating G^{-} field can therefore be minimised by choosing appropriate reference parameters. Incorporating the entire linear dispersion profile into the $G^{\pm}$ definitions is the surest way to reduce the magnitude of any co-propagating G^{-} field. On the other hand, results show that well chosen *dispersionless* reference parameters are almost as efficient (at reducing G^{-}), where the phase-velocity at the central frequency is used to construct the $G^{\pm}$ fields.

The nature of counter-propagating G^{-} fields has also been discussed. Unless some contrived situation exists (e.g. QPM in the backwards direction), the lack of phase-matching in the backwards direction ensures that there is no generation of G^{-} fields. Of course, interfaces are an exception, and may produce backward propagating G^{-} fields as expected. These results strongly suggest that under certain circumstances nonlinear propagation can be modelled using only G^{+}, making a forward-only approximation. The validity of this assumption is discussed in the next chapter.

Chapter 4

The Forward-Only Approximation

Chapter III showed how a direct Maxwell solver can be written in the form of *G-variables*. The directionality of *G-variables* allows the flux of the EM field to be separated into forward and backward components. In the vast majority of cases G^- fields can be reduced to insignificance through a careful choice of initial conditions and reference parameters; moreover the amount of G^- produced during the course of a simulation is minuscule unless some exotic nonlinearity (QPM in the backwards direction), or interface is involved. As these conditions rarely hold or can be avoided, a forward-only approximation can be adopted yielding all the computational advantages offered by reducing a bi-directional problem to a uni-directional one.

This chapter follows on from the last, examining the accuracy and feasibility of the forward-only approximation. We now show how the G^- field can be carefully factored out of the propagation model under certain conditions. To achieve significant computational gains, the dispersion contained within the reference parameters must somehow be approximated. By applying these ideas, a general approach using only the G^+ field is devised, that may be extended to a number of alternative propagation models. The first model is simply the application of the forward-only *G-variables*, and is termed *G-Maxwell*. The second model involves a bandwidth unlimited envelope method and is termed *G-envelope*. Finally, a model based on *G-Maxwell* and a transverse dimension is developed. These alternatives are discussed and compared to results from the PSSD method [32].

4.1 Forward-only approximation

4.1.1 Linear or nonlinear approximation

Any nonlinear term dependent on E, couples the forward and backward $G^{\pm}$ components together. This is because the derivative of the polarisation drives both the G^{+} and G^{-} fields. If we assume that there is no (counter or co-propagating) G^{-} initially, its generation may only arise from the nonlinear polarisation (in the absence of interfaces). Since the driving field is in phase with the nonlinear G^{+} field, it has the opportunity to grow in the forward direction. In the backward direction however, the G^{-} field generated from the nonlinearity is out of phase with the G^{+} field, and is therefore cancelled out. This is analogous to Huygens principle, where the forward propagating wavefront is a consequence of constructive interference, and the absence of a backward wave is because of the cancellation in phase of the secondary wavefronts in the reverse direction. This explains why an insignificant amount of backward-propagating G^{-} is generated. The only exception being QPM in the backward direction, where phase-matching forces the backward-propagating G^{-} to be non-trivial.

Having shown that the backward-propagating G^{-} field (generated) is trivially small, and that carefully chosen reference parameters remove any co-propagating G^{-} a forward-only approximation is applied. In order to maximise the computational gains, there are two dispersive approximations that can be made:

1. **Type I: Approximating the nonlinearity**. This approach uses a dispersive reference to perfectly match any linear dispersion ($\alpha_R = \sqrt{\epsilon_0 \epsilon_r(\omega)}$), reducing any (initial) co-propagating G^{-} field to zero. The approximation is then applied to the nonlinear term, by dividing out the permittivity at the central frequency: $\chi^{(n)}(\mathcal{F}^{-1}[E(\omega)/\epsilon_r(\omega)])^n \approx \chi^{(n)}(E(t)/\epsilon_r(\omega_0))^n$. This follows on from the results demonstrated in chapter III, that a dispersionless reference parameter at the central frequency almost perfectly matches the medium. Thus, to calculate the nonlinearity a dispersive G^{+} field is used, with the central dispersion removed.

2. **Type II: Approximating the dispersion**. This approach approximates the linear dispersion by constructing G^{+} using $\alpha_R = \sqrt{\epsilon_0 \epsilon_r(\omega_0)}$, namely: $\mathcal{F}^{-1}[\epsilon_r(\omega)E(\omega)] \approx \epsilon_r(\omega_0)E(t)$. The nonlinearity can then be simply calculated by dividing out α_R as it is dispersionless. Whereas the type I approximation uses a dispersionless reference to calculate the nonlinearity, here it is applied to the linear dispersion. This can be justified following the results in chapter III, where a well chosen reference parameter almost perfectly matches the material dispersion.

Applying either type I or type II approximations to *G-variables*, produces models requiring only three Fourier transforms, presenting a significant improvement over PSSD [32] (in itself a very efficient technique when complicated dispersion is involved). The benefits can be further enhanced by applying a moving frame transformation. Because both the linear and nonlinear responses are derived from the perturbation expansion of the polarisation, the linear dispersion is at least one order of magnitude greater than the nonlinear polarisation. The quantum theory describing the ratio of successive susceptibility terms within the polarisation expansion states

$$\frac{\chi^{(m+1)}E^{m+1}}{\chi^{(m)}E^{m}} \simeq \frac{eE_a a_B}{\hbar\Delta} = \alpha_{bb}, \tag{4.1}$$

where $\hbar$ is Planck's constant, a_B is the Bohr radius, and $\Delta = |\omega_{ik} - \omega_0|$ describes the transition frequency from the ground state i to some excited state k [22]. For the polarisation expansion to converge (see eq(2.4) Chapter II), the ratio $\alpha_{bb} << 1$. (For a detailed quantum mechanical approach to calculating the linear and nonlinear susceptibilities see [58].) For this reason, the type I approximation was made as it inherently approximates a lesser term when considering perturbative nonlinear optics. More specifically, a type I approximation represents a more reliable choice, since even the widest bandwidths combined with the most exotic linear dispersion can be perfectly matched (linearly).

To evaluate the effect of a type I approximation, the pseudo-spectral derivative of the nonlinearity of a fully deconvolved G^+ was compared to a partially deconvolved G^+. Fig. 4.1 compares the two cases for the derivative of $\chi^{(3)}E(t)^3$ (across the pulse shown in fig. 3.8 of chapter III)

Fig. 4.1 shows the agreement between $i\omega\mathcal{F}[\frac{G^+(t)}{2\sqrt{\epsilon_0\epsilon_r(\omega_0)}}]^3$ (blue "+"), and $i\omega\mathcal{F}|\mathcal{F}^{-1}[\frac{\mathcal{F}[G(t)]}{2\sqrt{\epsilon_0\epsilon_r(\omega)}}]|^3$ (red "·"). It is clear that the derivatives are almost identical in these cases justifying a type I approximation.

4.1.2 *G-Maxwell*

Now that the dispersive type I approximation has been justified, the equation of motion for the forward-only G^+ field is derived. The coupled $G^\pm$ equation from chapter III was:

$$\partial_z G^\pm = \mp i\omega\alpha_R\beta_0(1 \mp \zeta)G^\pm \mp \left(\frac{i\omega\epsilon_0\epsilon_r}{\epsilon_R} - 1\right)\frac{[G^+ + G^-]}{2} \mp \frac{i\omega\alpha_{NL}\beta_0}{2}[G^+ + G^-],$$

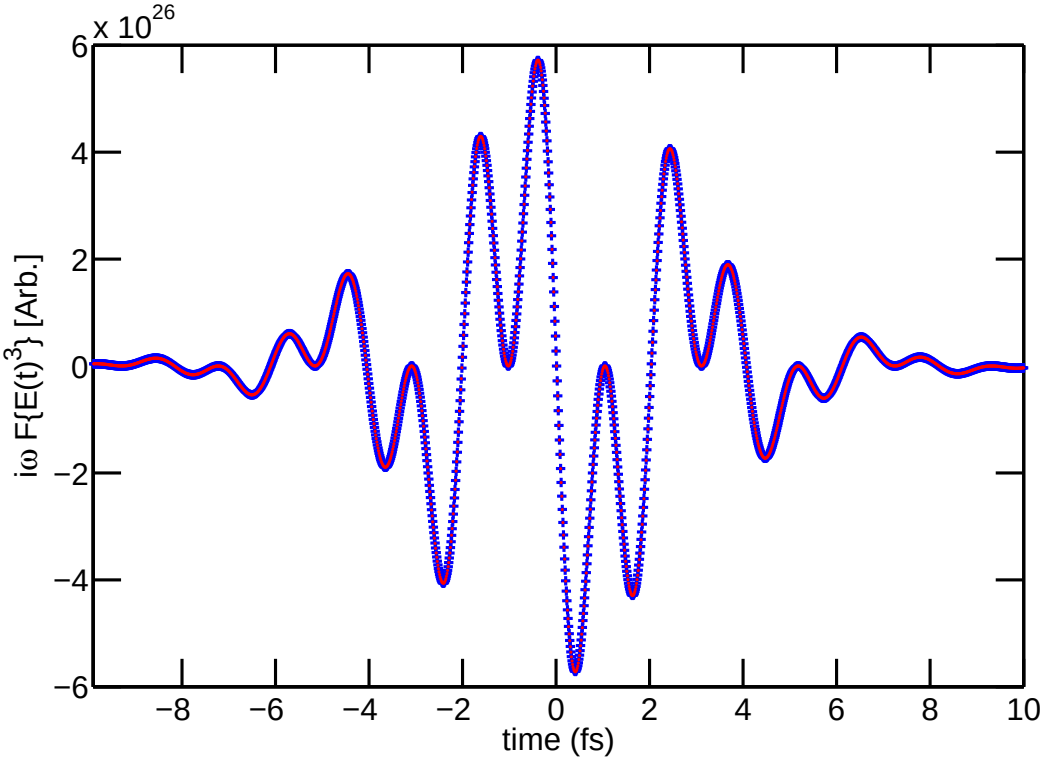

Figure 4.1: The blue "+" represent the derivative of the partially deconvolved $E(t)^3$, whereas the red "·" represents the derivative of the fully deconvolved $E(t)^3$. The difference is virtually indistinguishable, supporting the type I approximation.

making a forward-only approximation sets $G^- = 0$, and leaves the following terms

$$\partial_z G^+ = -i\omega\alpha_R\beta_0(1-\zeta)G^+ - i\omega\epsilon_0\beta_0\sum_{n>1}\chi^{(n)}\left(\frac{G^+}{2\alpha_R}\right)^n. \tag{4.2}$$

Applying a type I approximation in the case of a third order nonlinearity, yields

$$\partial_z G^+ = -i\omega\alpha_R\beta_0(1-\zeta)G^+ - i\omega\alpha_R\beta_0\frac{\epsilon_0\chi^{(3)}(G^+)^3}{8\epsilon_r^2(\omega_0)}. \tag{4.3}$$

The following algorithm can now be used to discretise the integration of the propagation equation

$$G^+|_{n+1} = G^+|_{n-1} - 2\Delta z\left(i\omega\alpha_R\beta_0(1-\zeta)G^+ - \alpha_R\beta_0\frac{\epsilon_0\chi^{(3)}(i\omega G^+)^3}{8\epsilon_r^2(\omega_0)}\right)\Bigg|_n. \tag{4.4}$$

In the above model, the dispersive reference perfectly matches the linear dispersion, and the deconvolution of the nonlinearity has been approximated by dividing out $2\alpha_R =$

$\sqrt{\epsilon_0 \epsilon_r(\omega_0)}$ from G^+.

4.1.3 *G-envelope*

Though the bandwidth limitations of envelope techniques have been severely tested over recent years, several attempts have been made by adding correction terms, to extend the range of applicability of these models. Blow and Wood extended the bandwidth limitations of the NLSE to a third of the underlying carrier [28]. Brabec and Krausz developed the Nonlinear Envelope Equation (NEE), which was derived in chapter II and is valid down to an impressive single cycle [26]. Porras [27] included transverse correction terms to the NEE, arriving at the Slowly Evolving Envelope Approximation (SEEA). More recently, Kinsler and New [29] developed the Generalised Few-cycle Envelope Approximation (GFEA), which is more general than all of the above, making no approximation until the final step of the analysis.

A recent paper by Genty *et al.* [35] demonstrated that it is possible to extend a carrier envelope description to any arbitrary bandwidth, using Green's functions to factorise the wave equation into forward and backward components. In their paper, comparative simulations between PSSD (direct Maxwell solver) and the Generalised Nonlinear Envelope Equation (GNEE) revealed a near perfect agreement between the two models. Thus, for the first time, a bandwidth unlimited envelope was successfully applied to the ultra-wideband problem of Carrier Wave Shocking, a very sensitive process involving multiple harmonics.

Motivated by the forward-only approximation described in section 4.1.1 and [35], a bandwidth unlimited G^+ envelope model was developed using *G-variables*. The model can accurately handle ultra-wideband pulses, where multiple harmonics are involved (e.g. Carrier Wave Shocking). In fact, solving the conjugate equation covers twice the computational domain than if the equation was solved directly.

To begin, we apply the envelope representation of the electric field from chapter II to the G^+ field, separating it into a complex envelope ($A(t,z)$) and carrier:

$$G^+_{z,t}(t) = A(t,z)e^{i(k_0 z - \omega_0 t + \phi_0)} + \text{c.c.} \tag{4.5}$$

(definitions for ω_0 can be found in chapter II, and are more extensively discussed in chapter VII). Eq(4.5) is substituted into eq(4.3), leading to:

$$\begin{aligned} &\partial_z A e^{i(k_0 z - \omega_0 t + \phi_0)} = -i\omega(\alpha_R \beta_0) A e^{i(k_0 z - \omega_0 t + \phi_0)} \\ &- i\omega(\alpha_R \beta_0)\Lambda \left(A^2 e^{2i(k_0 z - \omega_0 t + \phi_0)} + 3AA^*\right) A e^{i(k_0 z - \omega_0 t + \phi_0)} + \text{c.c.} \end{aligned} \tag{4.6}$$

where $\Lambda = \frac{\epsilon_0 \chi^{(3)}}{8\epsilon_r^2(\omega_0)}$, $k_0 = \frac{\omega_0 n_0}{c}$, and the arguments of A have been dropped for simplicity. The conjugate equation can now be solved after factoring out the carrier oscillations. Re-writing $i\omega\alpha_R\beta_0 = ik$, yields

$$\partial_z A = -i(k - k_0 - \zeta)A - i\omega(\alpha_R\beta_0)\Lambda\left(A^2 e^{2i(k_0 z - \omega_0 t + \phi_0)} + 3AA^*\right)A. \tag{4.7}$$

The algorithm used to calculate eq(4.7) is similar to eq(4.4), involving the same second-order accurate leap-frog method as *G-Maxwell*

$$A|_{n+1} = A|_{n-1} - 2\Delta z\left(i(k - k_0 - \zeta)A + \alpha_R\beta_0\Lambda i\omega\left(A^2 e^{2i(k_0 z - \omega_0 t + \phi_0)} + 3AA^*\right)A\right)\Big|_n, \tag{4.8}$$

and was chosen here because it enabled easy comparisons to be made between other direct Maxwell solvers, in particular PSSD. More accurate numerical integration schemes such as the Runge-Kutta method [59], would however be generally recommended as they can provide increased accuracy without compromising computational speed. It is common at this point to apply further approximations to eq(4.8), but this constrains the bandwidth, and is therefore not administered here. *G-envelope* and *G-Maxwell* are in fact almost identical, except that one is solved using a complex envelope (*G-envelope*) and the other (*G-Maxwell*), by explicitly using the field. Because the carrier has been removed (from *G-envelope*), all the information e.g. chirp, harmonic content etc is contained within the complex envelope. To fully appreciate the vast bandwidth that can be accurately supported by the envelope, a study of Carrier Wave Shocking (CWS) is necessary. As this remains the topic of chapters V and VI, its demonstration is left until then.

4.1.4 Simulations

The envelope simulations presented here involve pulse propagation through fused silica. The distance of propagation is 20 microns, and the strength of the nonlinearity has been increased to the damage threshold (50 TW/cm^2 [38]). The initial (transform limited) pulse, has the same characteristics as those in chapter III (fused silica). As the pulse propagates and undergoes linear and nonlinear dispersion, it becomes chirped. In an envelope picture, this information is stored on the complex envelope as phase. Fig. 4.2 shows the magnitude and phase of the complex envelope, after a 20 micron propagation

The nonlinear terms associated with the third-order nonlinearity are

$$(A^2 e^{2i(k_0 z - \omega_0 t + \phi_0)} + 3AA^*)A.$$

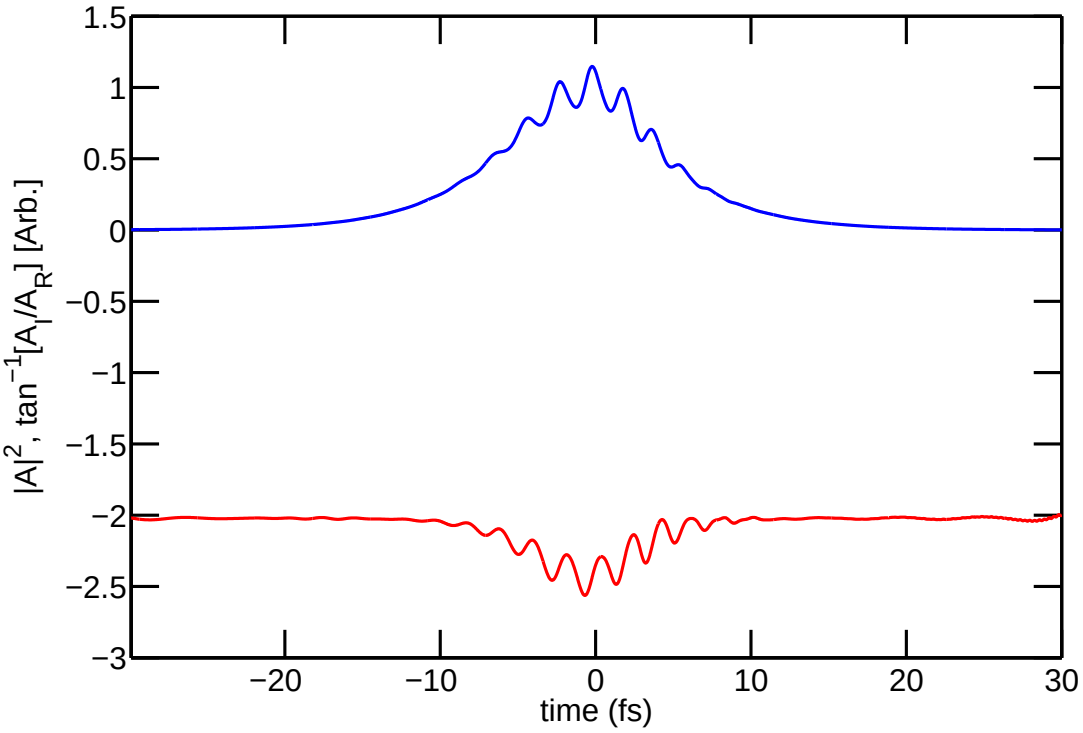

Figure 4.2: *G-envelope* representations of the forward-only approximation. The blue line represents the magnitude of the complex envelope, whilst the red line represents the phase. The oscillations on the complex envelope describe the electric field profile.

A common approximation in many-cycle pulses, is to remove nonresonant terms, leaving just $3AA^*A$ as the third order nonlinear term [45]. This approach is valid within a narrowband limit, and describes Self-Phase Modulation (SPM), where an intensity dependent phase is imparted onto the envelope. This approximation is no longer accurate when non-resonant nonlinear effects are considered.

The frequency content of the complex envelope can be seen in fig. 4.3. In this case, a large bandwidth is present, 'tilting' the carrier oscillations. Exclusion of non-resonant terms would merely distort the envelope, having little effect on the carrier.

4.2 Numerical comparisons

Numerical comparisons using the forward-only approximation are now made, to demonstrate the accuracy of the forward-only approximation with respect to direct Maxwell solvers. The section also agrees with results in [35], suggesting that envelope techniques can support arbitrary bandwidths. The simulation in fig. 4.3 (section 4.1.4) is now

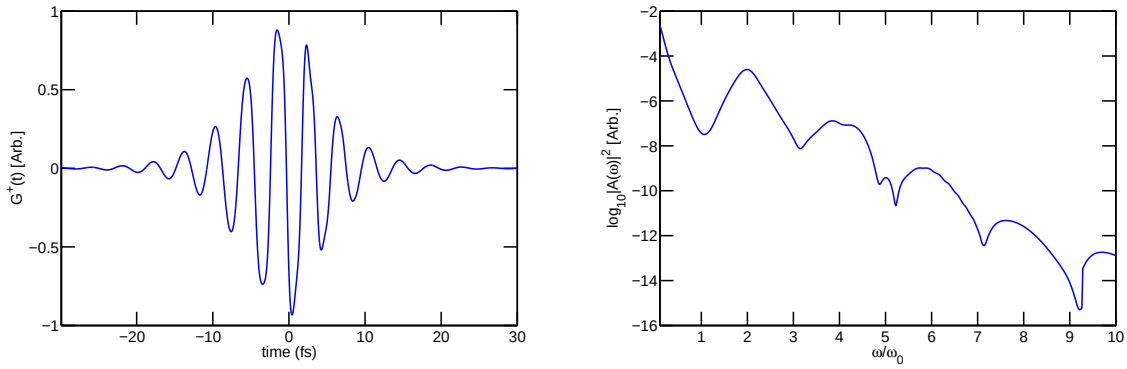

Figure 4.3: (left) Reconstructed G^+ field from envelope. The carrier oscillations have been affected by nonresonant terms. (right) Log plot of the envelope spectrum displaying a significant amount of frequency content, which is necessary to distort the carrier. Note the presence of the dc component on removal of the carrier.

reproduced using *G-Maxwell* and PSSD.

Fig. 4.4 reveals that the three methods are all in excellent agreement, especially *G-Maxwell* and *G-envelope*, whose differences would not be visible had solid lines been plotted. To fully appreciate the conformity of the different methods, a logarithmic plot of the spectra from the three approaches is shown in fig. 4.5. All three spectra share almost identical spectral features even on a log scale.

The agreement between PSSD, *G-Maxwell* and *G-envelope* highlights the following properties:

- By carefully choosing reference parameters (and initial conditions) it is possible to describe a forward propagating pulse using a combination of E and H fields.
- The nonlinear driving field produces negligible amounts of G^- during propagation, supporting the forward-only approximation where $G^- \rightarrow 0$.
- Instead of a full deconvolution, the nonlinearity can be approximated using a reference parameter centred on $\epsilon_r(\omega_0)$.
- A wideband envelope can be developed in place of any uni-directional approximation, but care is needed to allocate sufficient bandwidth to describe the higher frequencies.
- Directional *G-variables* converge with bandwidth unlimited envelope techniques. A suite of propagation techniques span the gap between direct Maxwell solvers and narrowband envelopes. A schematic of this spectrum can be seen in fig. 4.6.

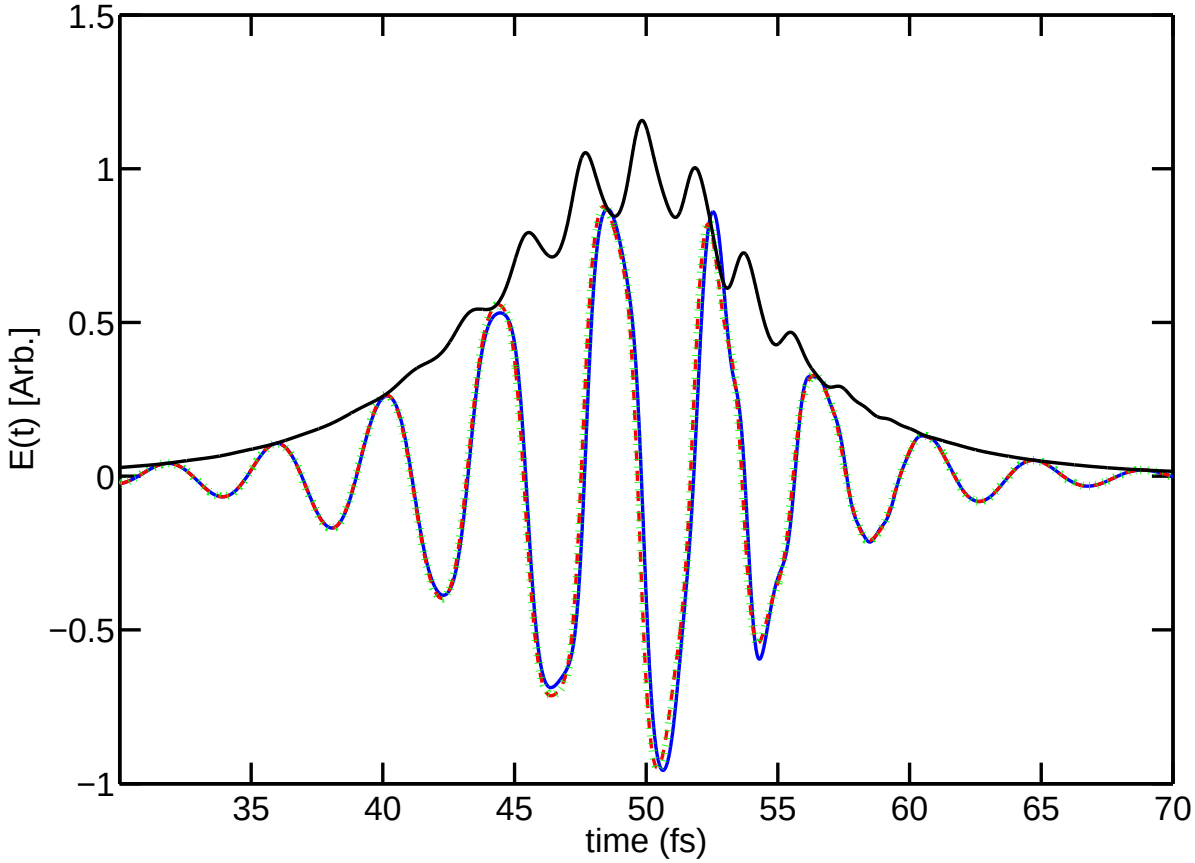

Figure 4.4: Reconstructed E field using three different numerical methods for a 10 micron propagation: PSSD (blue-solid), *G-Maxwell* (red-dashed) and *G-envelope* (green-dots). The black curve shows the magnitude of complex envelope, where high frequency oscillations can be seen. All three methods are in excellent agreement.

4.3 Diffraction

To exploit the advantages of *G-variables*, a transverse dimension was added to *G-Maxwell*. This section is included as 'proof-of-principle', of a transverse wideband propagation model based on *G-variables*. Transverse beam effects are generally treated within the quasi-monochromatic limit but here they can be included as part of a wideband propagation model (*G-Maxwell*). Though in general *two* transverse dimensions are needed to describe diffraction, Bessel functions can be used to reduce this to *one* transverse dimension, when there is some form of circular geometry. Unfortunately, using fast Fourier transforms for these calculations produces a non-uniform mapping between the spatial wave vector (k_r) and the radius (r). To avoid this problem, and because the motivation here is 'proof-of-principle' a Cartesian transverse dimension was added.

Diffraction is one of the most fundamental phenomena associated with waves. Any

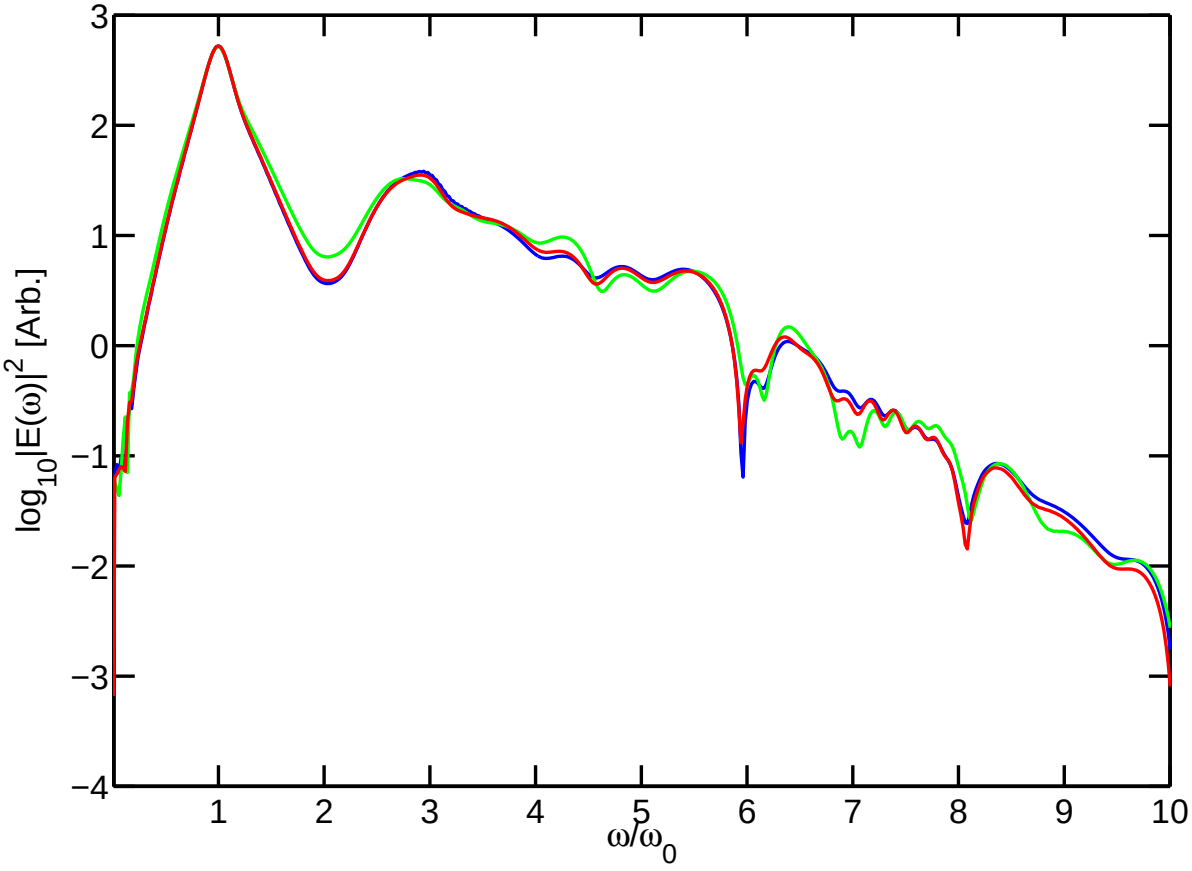

Figure 4.5: Spectra of the different numerical methods presented in fig. 4.4: PSSD (blue), *G-Maxwell* (red) and *G-envelope* (green).

non-planar wave diffracts, where the wavefront can be decomposed into a set of plane waves, all travelling at different angles (analogous to the decomposition of a temporal pulse into its frequency constituents). The equation describing scalar diffraction of an EM field in free space is

$$[\nabla^2 + k^2]\tilde{E}(x, y, z) = 0 \tag{4.9}$$

where $\tilde{E}$ is the complex amplitude of a field distribution consisting of monochromatic waves. Making the substitution $\tilde{E} = \tilde{a}(x, y, z)e^{-ikz}$ into eq(4.9), and factoring out the exponential leaves:

$$\frac{\partial^2 \tilde{a}}{\partial x^2} + \frac{\partial^2 \tilde{a}}{\partial y^2} + \frac{\partial^2 \tilde{a}}{\partial z^2} - 2ik\frac{\partial \tilde{a}}{\partial z} = 0 \tag{4.10}$$

Because $\frac{\partial^2 \tilde{a}}{\partial z^2}$ varies much more slowly than the other terms, it can be discarded, leaving

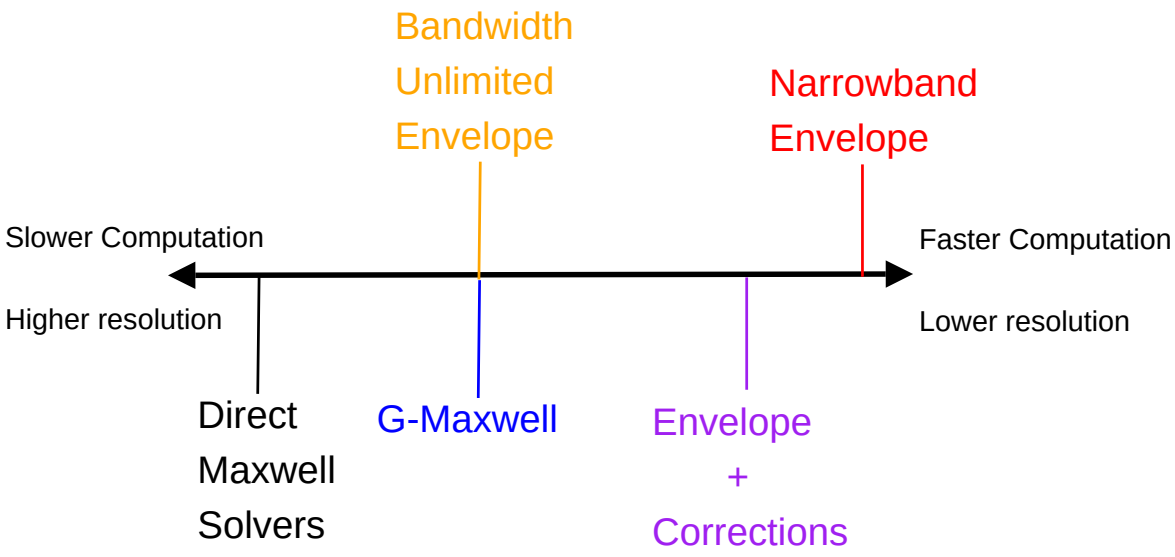

Figure 4.6: Schematic diagram describing nonlinear propagation techniques. A range of methods span the gap between narrowband and ultra-wideband pulses. Bandwidth unlimited envelopes converge with more explicit 'uni-directional' Maxwell solvers.

the paraxial wave equation

$$\frac{\partial^2 \tilde{a}}{\partial x^2} + \frac{\partial^2 \tilde{a}}{\partial y^2} = \nabla_\perp^2 \tilde{a} = 2ik\frac{\partial \tilde{a}}{\partial z}. \tag{4.11}$$

This approximation is valid in nearly all cases of optical pulse propagation, and only breaks down when a significant portion of the pulse travels at an angle of more than $\pi/6$ (30^o) [60] to the axis of propagation. As we are concerned with uni-directional pulse propagation, these assumptions can be easily satisfied in a *G-Maxwell* model.

4.3.1 Modelling diffraction

The famous Huygens principle states:

"Every point on a primary wavefront serves as the source of a spherical secondary wavelet, such that the primary wavefront at some later time is the envelope of these wavelets. Moreover, the wavelets advance with a speed and frequency equal to that of the primary wave at each point in space."

Fresnel modified this principle to explain why no wave is observed travelling in the backward direction. In fact, the explanation is very similar to the lack of backward-

propagating wave in general nonlinear models. This is because constructive phase matching takes place in the forward direction, as opposed to the backwards direction, where the individual phase contributions cancel each other out.

Diffraction can either occur in the near or far field, and is described by the dimensionless Fresnel number (F). F describes the relationship between wavelength (λ), beam waist (q) and propagation distance (L), in the following manner

$$F = \frac{q^2}{L\lambda}. \tag{4.12}$$

$F \geq 1$ is termed the near-field and is described by Fresnel diffraction, whereas $F << 1$ is classed as the far-field, where Fraunhofer diffraction applies. The type of diffraction modelled here is near-field diffraction, based on the Fresnel approximation; $\lambda = 1240$ nm, $q = 15$ and $L = 100$ microns.

Huygens integral in the near field can be thought of as a multiplication of the FT of the wavefront with a spherical wavefront [60]. As the frequency domain is already being used for the application of dispersion, this approach can be easily built into *G-Maxwell*. Scalar diffraction can be understood with some simple geometry in k-space. It is possible to represent an infinite set of plane waves ($W(x, y, z)$), as follows:

$$W(x, y, z) = e^{-ik\cdot r} = e^{-i(k_x x + k_y y + k_z z)}. \tag{4.13}$$

Making the paraxial approximation it is possible to rewrite the k_z propagation vector in terms of its longitudinal and transverse components. The longitudinal contribution can now be written as:

$$k_z = k\cos(\theta) = \sqrt{k^2 - k_x^2 - k_y^2} \simeq k\left(1 - \frac{\kappa^2}{2k^2}\right) \tag{4.14}$$

where $\kappa^2 = k_x^2 + k_y^2$, and θ is the off-axis angle. Using eq(4.14), the contribution of an off-axis plane wave vector (k) arriving at a distance L from a previous wavefront position can now be calculated. Diffracting the $G^+(x, y, z)$ field leads to

$$G^+(x, y, z) = \mathcal{F}^{-1}[\mathcal{F}[G^+(x, y, z = 0)]e^{-ikL(1-\frac{\kappa^2}{2k^2})}]. \tag{4.15}$$

Thus eq(4.15) describes diffraction in free space of an arbitrary G^+ wavefront over a distance L. In our *G-Maxwell* model, diffraction is limited to one transverse dimension, so that now $\kappa^2 = k_x^2$.

Eq(4.15) does not include nonlinearity, and therefore the entire diffraction process

could be taken in a single step. Indeed it is also possible to incorporate dispersion into the above argument and propagate the entire distance L in a single step. In a dispersive medium, the wave-vector adopts a scaled length that is dependent on the refractive index. For simplicity, the refractive index is assumed to be isotropic. Thus the longitudinal k-vector component (k_z), describing the evolution of a particular angular frequency (over a distance L), with only one transverse dimension can be written in operator form as

$$\hat{Q} = e^{-ik_z L} = e^{-in(\omega)kL(1-\frac{k_x^2}{k^2})}. \tag{4.16}$$

Applying $\hat{Q}$ to each k-vector component, diffraction and dispersion can be simultaneously calculated.

In the transverse *G-Maxwell* model, a split-step method is used in the nonlinear propagation. The split-step method applies scalar diffraction and dispersion over a small z step, followed by the nonlinear evolution of the field. The nonlinear step is calculated using a series of pseudo-spectral derivatives, applied to the recently diffracted and dispersed G^+ field; a schematic diagram of the process can be seen in fig. 4.7. The philosophy of a split-step method is that the linear and nonlinear parts of the propagation can be separately calculated over small steps. The Fourier split-step method was therefore used with a moving frame transformation, providing an efficient, second-order accurate solution. For a detailed analysis of the split-step method see [45].

4.3.2 Preliminary results

To demonstrate the scheme, transverse wideband nonlinear propagation was simulated in fused silica, over a distance of 100 microns ($w_0 \simeq 20\mu$m). Fig. 4.8 shows the transverse profile of the pulse at the end of the propagation. The initially flat wavefronts have become curved during the propagation because of diffraction. The intensity dependent refractive index has also caused the on-axis wavefront in the more intense regions, to move to higher times.

To understand the effect of diffraction, the on-axis G^+ field is compared to a plane wave simulation in fig. 4.9 revealing some interesting differences. The plane-wave (red) profile has a higher peak intensity than the transverse pulse (blue) because of diffraction. This does not significantly affect the leading edge of the pulse, but does influence the central and trailing edges of it. The change in the peak intensity also appears to affect the amount of third harmonic produced.

The transverse behaviour of ultra-wideband pulses is a vast topic that requires more extensive investigation. Its introduction here is merely meant to demonstrate the feasibil-

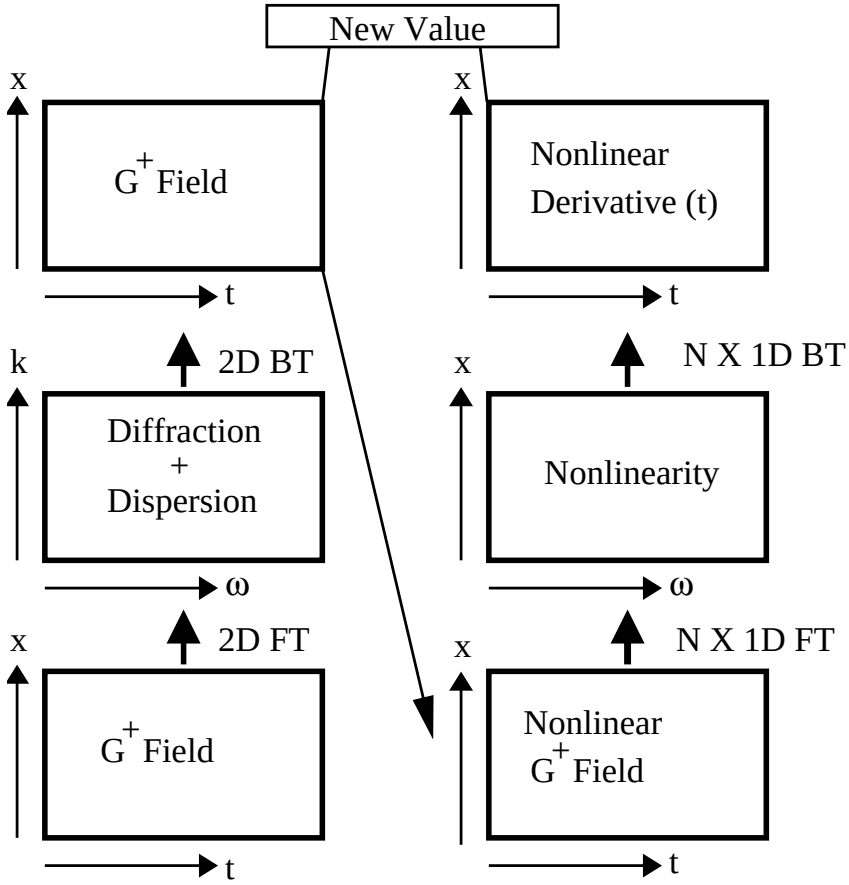

Figure 4.7: Schematic diagram of the split-step method, where 'FT' and 'BT' correspond to Fourier Transform and Back Fourier Transform respectively.

ity of wideband, transverse propagation using *G-variables*. The approach offers a faster alternative to FDTD, without enforcing bandwidth limitations. Though one might argue that bandwidth unlimited envelope approaches afford the same speed-up, it is ultimately the uni-directionality of both methods that is exploited. The more explicit *G-Maxwell* method, makes the incorporation of a transverse dimension simpler because of the clarity and mapping of the wavelengths involved.

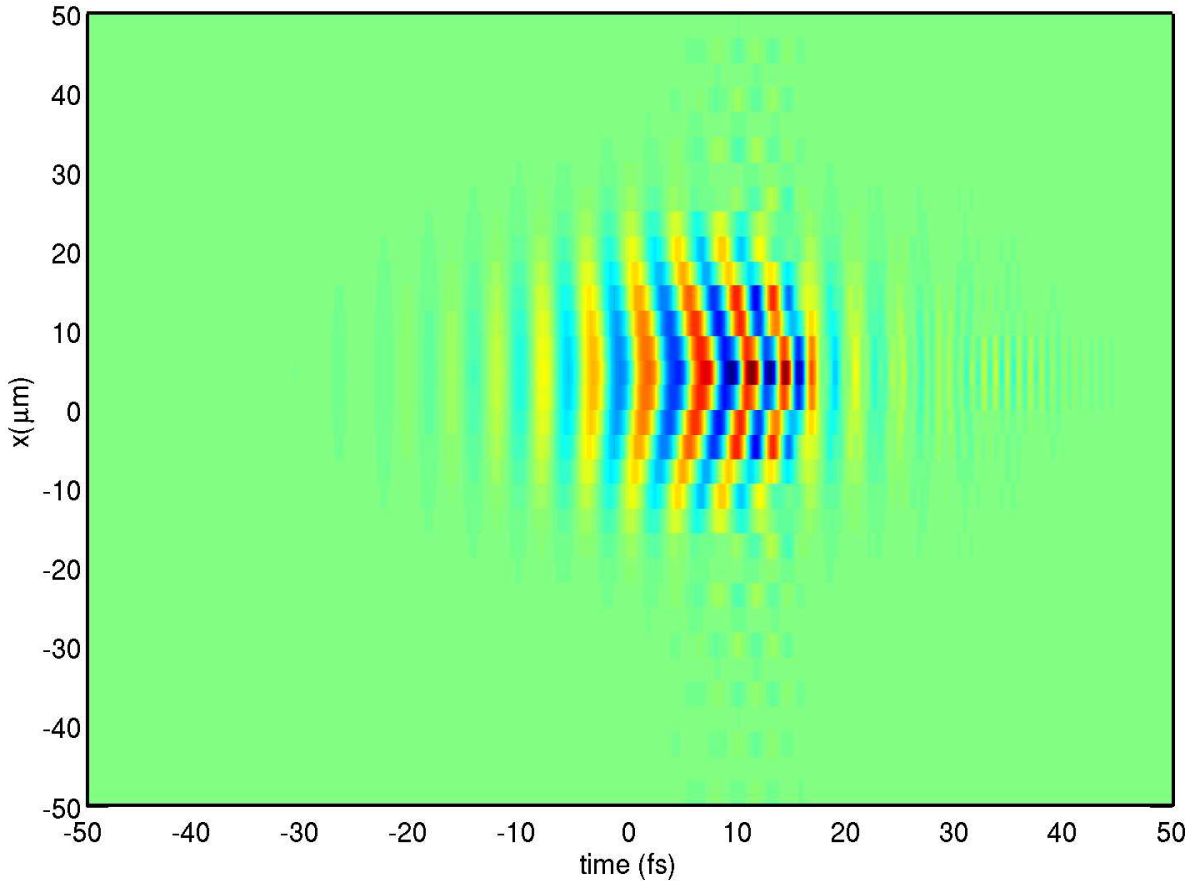

Figure 4.8: Wideband *G-Maxwell* simulation with added transverse dimension. The initial pulse has propagated 100 microns at the damage threshold of fused silica. The initially flat wavefronts have become curved from the intensity dependent refractive index and diffraction.

4.4 Conclusion

- Careful choice of reference parameters and initial conditions can almost completely eliminate G^-.
- The nonlinear driving field produces negligible amounts of G^- during propagation, supporting the forward-only approximation where $G^- \rightarrow 0$.
- A forward-only approximation can reduce a bi-directional problem into a uni-directional one, making nonlinear propagation far less demanding in terms of computational time.
- A bandwidth unlimited envelope is developed (*G-envelope*) from the forward-only

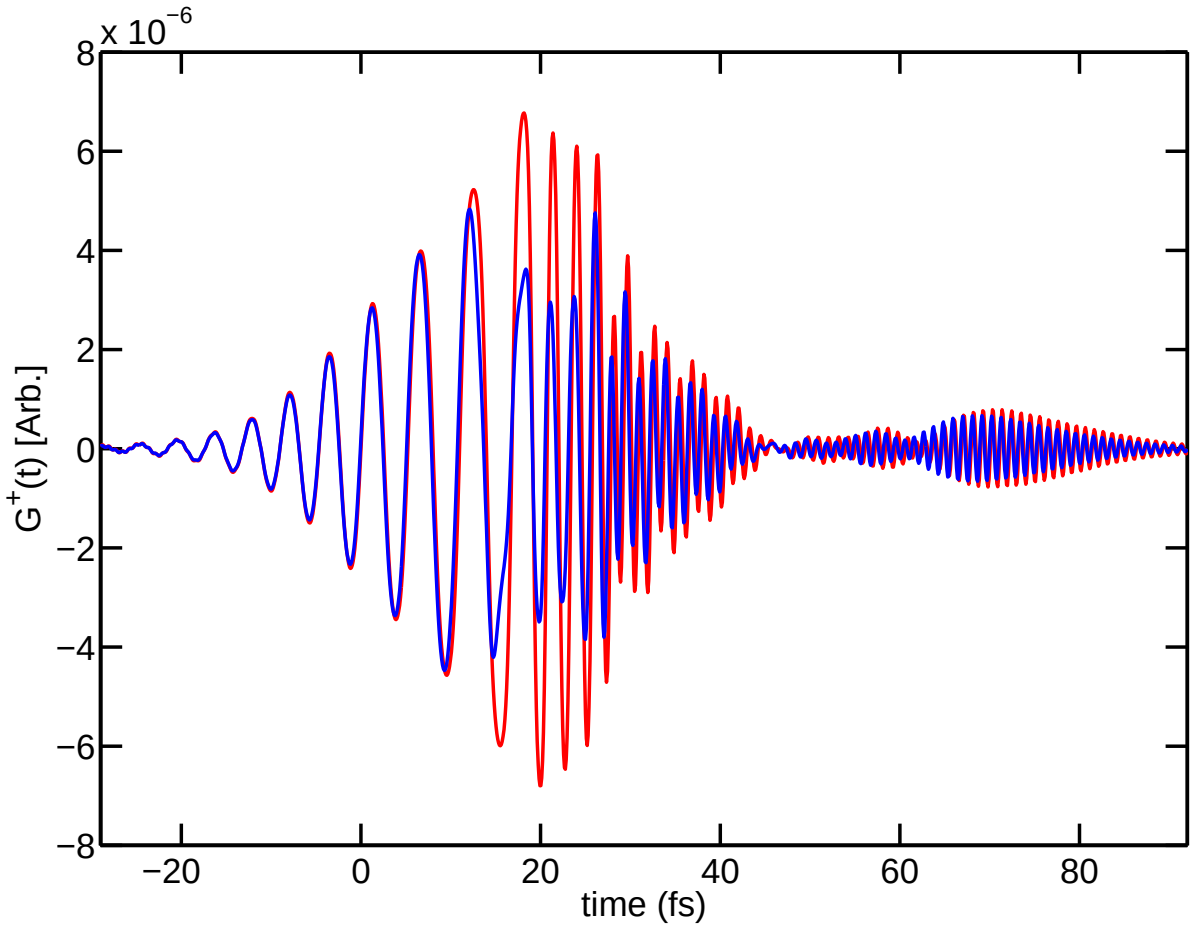

Figure 4.9: Comparison of the diffracted beam on-axis (blue), with a plane wave simulation (red). The difference between the two cases is apparent at the centre and trailing edges of the pulse.

approximation, demonstrating convergence between more explicit uni-directional approaches and carrier-envelope approaches. Excellent agreement is found between *G-Maxwell*, *G-envelope* and PSSD, even when wide bandwidths are involved.

- The successes of *G-Maxwell* facilitate the addition of a transverse dimension, enabling ultra-wideband, transverse nonlinear problems to be investigated.

Chapter 5

Carrier Wave Shocking

5.1 Introduction

The earliest discussion of electromagnetic shocks occurring on the optical carrier appeared in a paper by Rosen in 1965 [36]. At the time, the notion was purely theoretical given the intensity of the pulses then available. However the self-steepening of the pulse *envelope* was discussed two years later by De-Martini *et al.* [61]. The idea of envelope self-steepening soon became well known [61–64] but its application to the optical carrier received little attention until Moloney *et al.* revisited the subject in the 1990s with the help of FDTD simulations [37, 38]. Since then, Kinsler *et al.* [39] studied the role of dispersion in Carrier Wave Shocking, with a range of numerical methods.

Not only is Carrier Wave Shocking (CWS) a remarkable nonlinear phenomenon with possible applications to HHG [41], but it also offers the ideal test bed for ultra-wideband numerical simulations. This is because a mathematical shock requires an infinite bandwidth, for its description. This chapter discusses the nature of CWS from a mathematical, numerical and physical point of view.

We start by developing a mathematical model based on the Method Of Characteristics (MOC), to provide analytic solutions in the dispersionless regime. These solutions then enable accurate and reliable shock detection techniques to be developed within the contexts of the numerical model. The ideas are then extended to more general cases involving designer dispersion, which is a crucial stage in understanding the interplay of linear and nonlinear effects in CWS. The knowledge is then applied to the most general case of CWS in real media, where the possibility of physically realising a shock is discussed.

5.1.1 Basic theory

The 1D plane polarised Maxwell equations form the starting point of our analysis:

$$\frac{\partial E_x(t,z)}{\partial z} = -\mu_0 \frac{\partial H_y(t,z)}{\partial t} \tag{5.1}$$

$$-\frac{\partial H(t,z)}{\partial x} = \frac{\partial}{\partial t}\left[\epsilon_0 \epsilon_r(t) * E_x(t,z) + \chi^{(3)} E_x(t,z)^3\right], \tag{5.2}$$

where the polarisation includes linear dispersion ($\epsilon_r * E$), and third-order instantaneous nonlinearity ($\chi^{(3)}E^3$). Though the ultimate goal here is to understand the interplay of dispersion in the process, we begin by studying CWS in dispersionless media, as this is the only regime possessing analytical solutions. This enables the process to be understood in its simplest sense, and provides a method to verify the numerics, and shock detection schemes, before deploying them to more general dispersion profiles.

Fig. 5.1 illustrates the simplest case of CWS, occurring in a dispersionless medium with a third-order nonlinearity. The profile shows the pulse at the point of shocking, where near vertical gradients are visible.

5.1.2 Simulation parameters

The initial pulse profile used throughout this chapter was

$$E(t) = E_0 \sin(\omega_1 t + \phi)\mathrm{sech}(\mathrm{d} \cdot \omega_1 \mathrm{t}), \tag{5.3}$$

where $\omega_1 = 2.356 \times 10^{15}$ rad s^{-1} (wavelength=800 nm), and "d" parameterises the width of the sech envelope (standard $d = 0.3$). [1] The array size was set to N=16384 nodes, with a time window dependent on the type of pulse being investigated. Simulations involving fused silica (at the end of the chapter), use a central wavelength of 1240 nm, and $d = 0.1$. In the cw case, a lower resolution of 1024 grid points was used, as one wavelength was fitted to the entire period of the grid (i.e. 1024 points per carrier wavelength). The PSSD technique [32] was primarily used for simulations in this chapter, because of its very high level of energy conservation. Orzag's 2/3 rule [59] was employed to filter the upper third of the spectral domain, stopping aliasing and the buildup of '2h' waves (waves of the highest possible grid frequency). The default nonlinear strength was $\chi^{(3)}E_0^2 = 0.02$, comparable to 0.7×10^{14}W/cm^2 in fused silica.

[1] Only in this chapter is ω_1 defined as the central frequency, as it helps explain some of the later figures. The notation is also chosen to be consistent with [39].

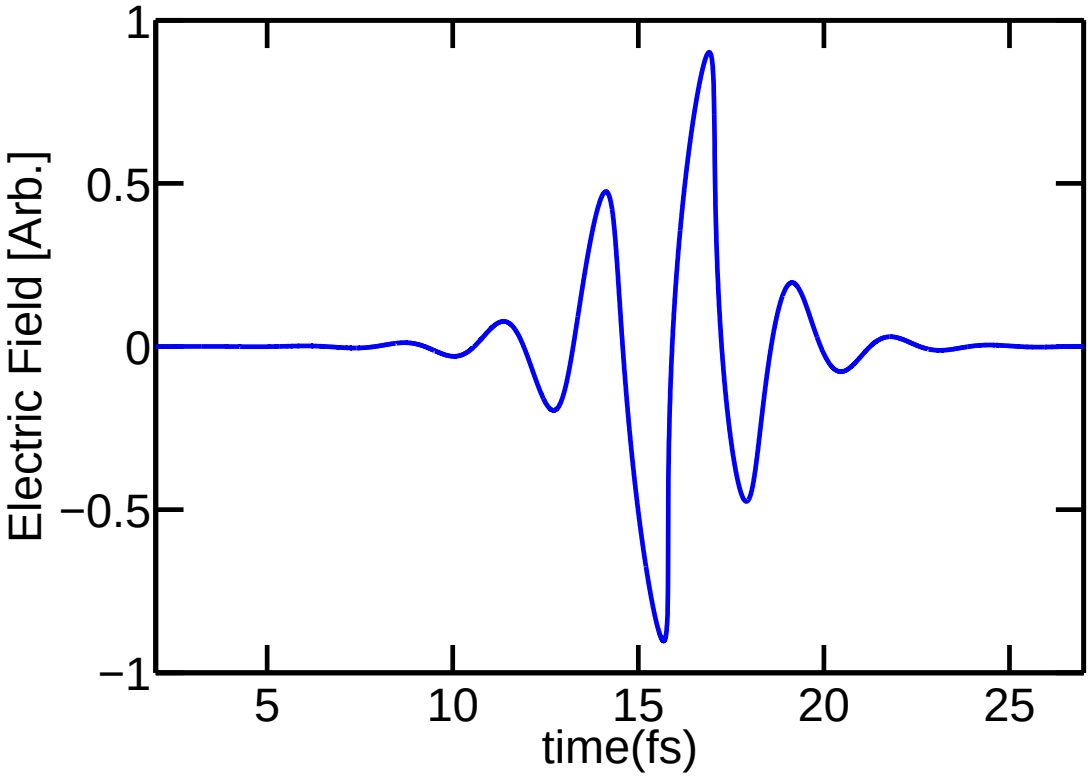

Figure 5.1: E field profile of a pulse at the point of shocking. The most intense regions of the pulse have been delayed by the intensity dependent refractive index, producing a 'leaning' effect. This causes near vertical gradients to arise on the back of the most intense carriers.

5.2 CWS in dispersionless media

5.2.1 Method Of Characteristics (MOC)

The analysis begins with the second order wave equation derived from eq(5.1) and eq(5.2)

$$c^2\frac{\partial^2 E}{\partial z^2} = (1+\chi^{(1)})\frac{\partial^2 E}{\partial t^2} + \chi^{(3)}\frac{\partial^2 E^3}{\partial t^2}. \tag{5.4}$$

Here

$$D = \epsilon_0(E + \chi^{(1)}E + \chi^{(3)}E^3), \tag{5.5}$$

and the subscripts have been dropped for brevity. Eq (5.4) can be factorised into two first order PDEs,

$$\left(v(E)\frac{\partial}{\partial z}+\frac{\partial}{\partial t}\right)\left(v(E)\frac{\partial}{\partial z}-\frac{\partial}{\partial t}\right)E=0, \tag{5.6}$$

describing fields travelling in the $\pm z$ direction. The velocity $v(E)$ of the E field is given by

$$v(E)=\frac{c}{\sqrt{\epsilon_r+3\chi^{(3)}E^2}}. \tag{5.7}$$

Taking the field travelling to the right in eq(5.6), presents us with a first order PDE where the initial conditions travel on characteristics given by the velocity of eq(5.7).

A simple calculation using the construction in fig. 5.2, enables us to predict the distance where two characteristics intersect, producing a shock at C. In fig. 5.2, A and B correspond to two adjacent points on the initial pulse with slightly different E field values.

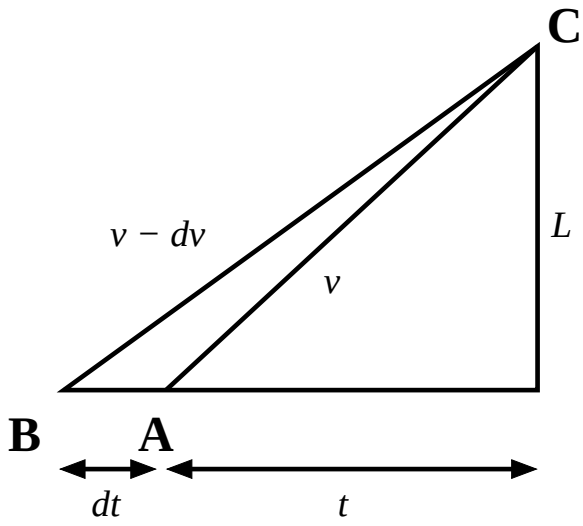

Figure 5.2: Method Of Characteristics. The two adjacent field values produce a shock at C after travelling a distance L.

The two characteristics AC and BC intersect at a distance L, the former travelling slower than the latter. The small differences in time and velocity allow us to write a

simple differential equation

$$\frac{dv}{dt} = \frac{v}{t} = \frac{v^2}{L}, \tag{5.8}$$

where $n_0 = \epsilon_r^{1/2}$, and the derivative of (5.7) can be calculated, yielding

$$\frac{dv}{dt} = -\frac{3c\chi^{(3)}}{2[n_0^2 + 3\chi^{(3)}E^2]^{3/2}}\frac{d(E^2)}{dt}. \tag{5.9}$$

Combining eq(5.8) and eq(5.9) then leads to a formula for L, namely

$$L = \frac{2cn_0\sqrt{1 + 3\chi^{(3)}E^2/n_0^2}}{3\chi^{(3)}(-dE^2/dt)}. \tag{5.10}$$

Because a shock first develops at the minimum value of L, an upper boundary condition can be imposed so the shocking distance becomes

$$L_{shock} = \frac{2cn_0\sqrt{1 + 3\chi^{(3)}E^2/n_0^2}}{3\chi^{(3)}} \quad \min\left[\frac{1}{-\mathrm{dE^2/dt}}\right]. \tag{5.11}$$

L_{shock} can now be used to develop shock detection methods, and verify their accuracy.

5.2.2 Numerical shock detection

So far we have developed a mathematical model for CWS that will predict L_{shock} in the dispersionless case. The physical manifestation of a shock will undoubtedly differ from any mathematical or numerical depiction, but this discussion is postponed until the end of the chapter.

Any numerical model takes place within a finite computational domain, and thus has a limited resolution. As a simulation proceeds towards a mathematical shock, the field gradients become progressively steeper, eventually becoming so steep that numerical breakdown begins. Increasing the number of grid points not only slows the simulation down, but also fails to alleviate the problem, as the extra bandwidth available, is exhausted after a few extra iterations. This has been tested with different resolutions and convergence checks.

In a discrete system, numerical breakdown itself can be used to infer where a mathematical shock is about to occur. The simplest way to monitor numerical integrity derives from energy conservation. Because PSSD generally displays energy conservation to an accuracy of one part in 1×10^{14}, even the slightest numerical breakdown is detectable.

However, the disadvantage of using energy conservation for shock detection, is that there is no convergence to a specific distance. Thus, the breakdown of energy conservation occurs over a range of distances close to where a shock might occur. For this reason it was utilised as a complementary shock detection method, independently verifying the more sophisticated Local Discontinuity Detection (LDD) method which we now discuss.

5.2.3 Local Discontinuity Detection (LDD)

The most accurate and reliable technique for shock detection was the Local Discontinuity Detection (LDD) method, which has parallels in other fields [65]. Monitoring the profile of a pulse approaching a shock, revealed points of inflection appearing in the vicinity of the maximum gradient. These have been shown elsewhere, to be signatures of incipient shock formation [65]. A scheme was therefore set up, to scan the profile of the E field around the maximum gradient searching for such features. Various tolerances for the distance between the maximum gradient and the point of inflection were tested, but were found to have little effect on L_{shock}. Other sensitivities were also tested, but the default parameters chosen for their reliability were: *one point of inflection, over adjacent grid points, within a range of five grid points from the maximum gradient.*

Fig. 5.3 shows an example of an E field profile that has triggered the LDD scheme, along with a close-up of the shock.

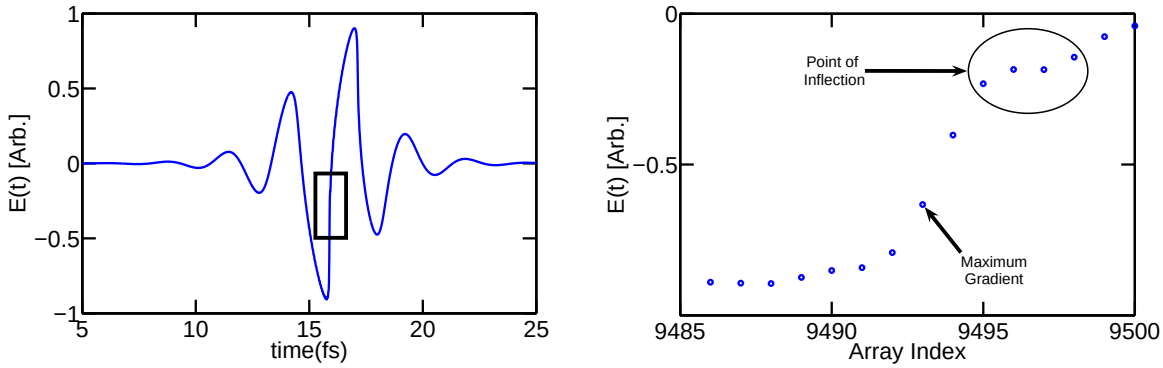

Figure 5.3: (left) E field of a pulse at the point of shocking, where the LDD method has been used as the detection measure. (right) Enlargement of the rectangle, displaying the features that have triggered the LDD method.

Having developed a shock detection mechanism, it was then tested within the dispersionless regime, where analytical solutions allow direct comparisons to be made. These tests also reveal some fundamental characteristics of CWS, including CEP sensitivity for few-cycle pulses.

5.2.4 Factors affecting L_{shock} in the dispersionless regime

In this section, the sensitivity of CWS to fundamental parameters appearing in eq(5.11) are investigated using the LDD method. The basic parameters varied were: pulse length, Carrier Envelope Phase (CEP), and bulk refractive index (parameterised by d, ϕ, and n_0 respectively). The results were then compared to analytic solutions produced using the MOC.

Fig. 5.4 demonstrates how L_{shock} changes for different pulse lengths (by varying d in eq(5.3)). The results indicate that L_{shock} decreases for longer pulses. One proposed reason for this [39], is that narrower bandwidths are more efficient at generating higher harmonics.

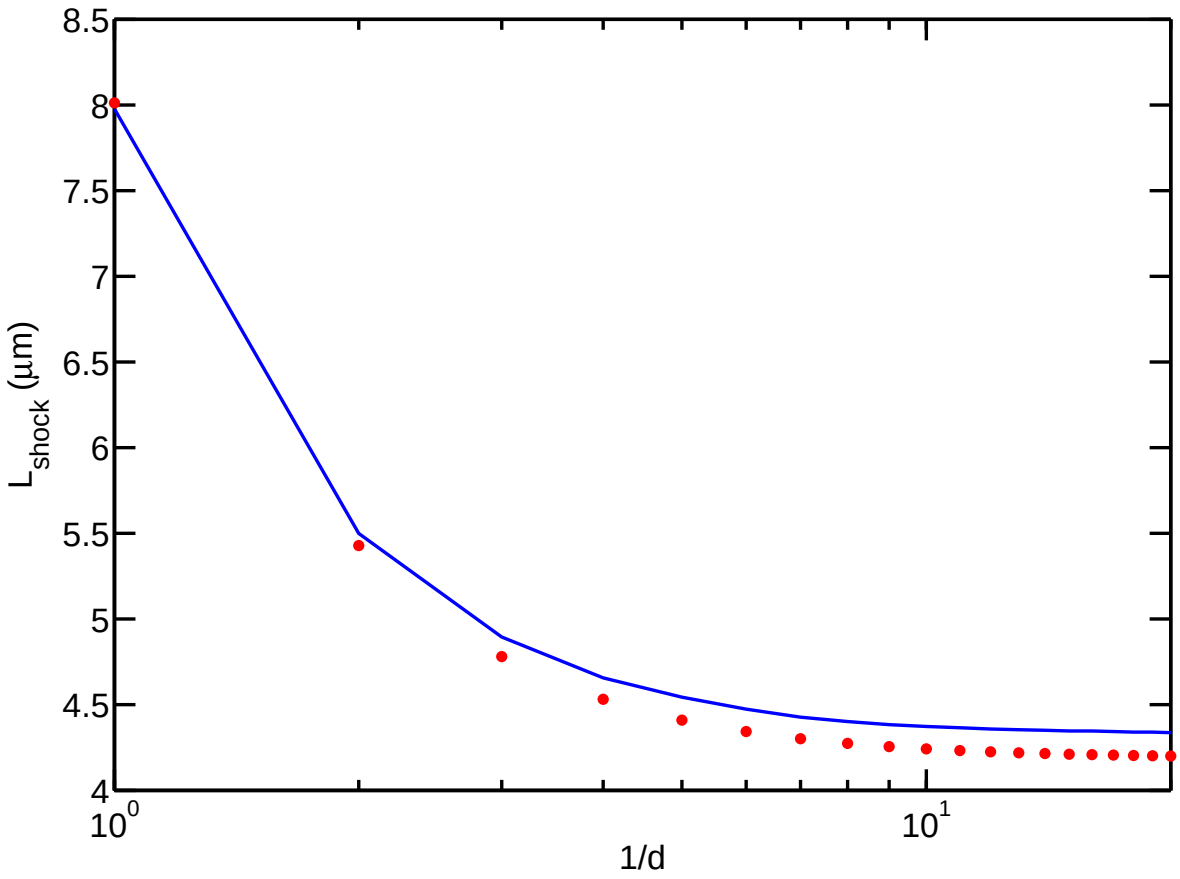

Figure 5.4: Sensitivity of L_{shock} to pulse length. The LDD method (red dots), and MOC (blue solid) are in excellent agreement, showing that L_{shock} increases for shorter pulses.

In reality, the sub-cycle pulses that shock at greater distances, have experienced changes to their peak intensity and central wavelength. This occurs, as the envelope affects the central carrier [26], explaining the increase in L_{shock}. This effect is discussed

in more detail, later in chapter VII. Fig. 5.4 also demonstrates the agreement between the LDD method and the MOC, the former always shocking slightly earlier than the latter. For pulses longer than one cycle, pulse length makes little difference to L_{shock}, and is consistent with the notion that the *carrier* is shocking, as opposed to the envelope.

The sensitivity of L_{shock} to CEP was then tested. Fig. 5.5 reveals CEP sensitivity using the LDD method (red dots), where a sharp peak occurs at $\phi \simeq 0.3$ rad, and is also supported by the MOC (solid blue). The peak marks a curve crossing, where the shock location switches from one part of the carrier oscillation to another ($-E\frac{dE}{dt}$ can either have a negative field value E or gradient $\frac{dE}{dt}$). The location of the peak did not change as the pulse width (d) was varied, however L_{shock}) did increase for shorter pulses. As expected, CEP was found to play a much smaller role in longer pulses.

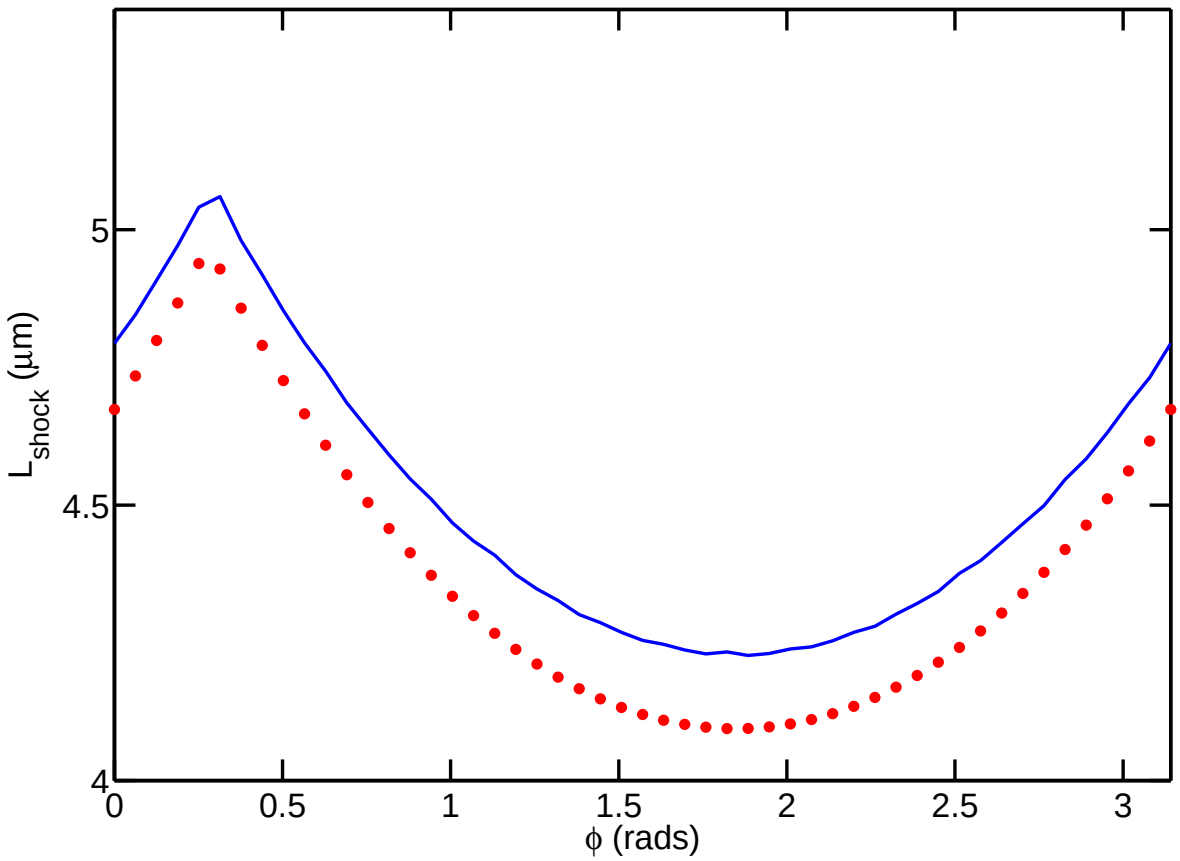

Figure 5.5: L_{shock} as a function of CEP (ϕ), for LDD (red dots) and MOC (blue solid). L_{shock} is greatest at $\phi \simeq 0.3$ rad, where the shock location switches from one part of the carrier oscillation to another. In this case, the default value of $d = 0.3$ was used in eq(5.11) to highlight the CEP sensitivity.

Finally L_{shock} was tested as a function of the bulk refractive index (n_0). Fig. 5.6 shows how L_{shock} increases with n_0, as predicted by eq(5.11). In all the above cases, the LDD method and MOC were in excellent agreement.

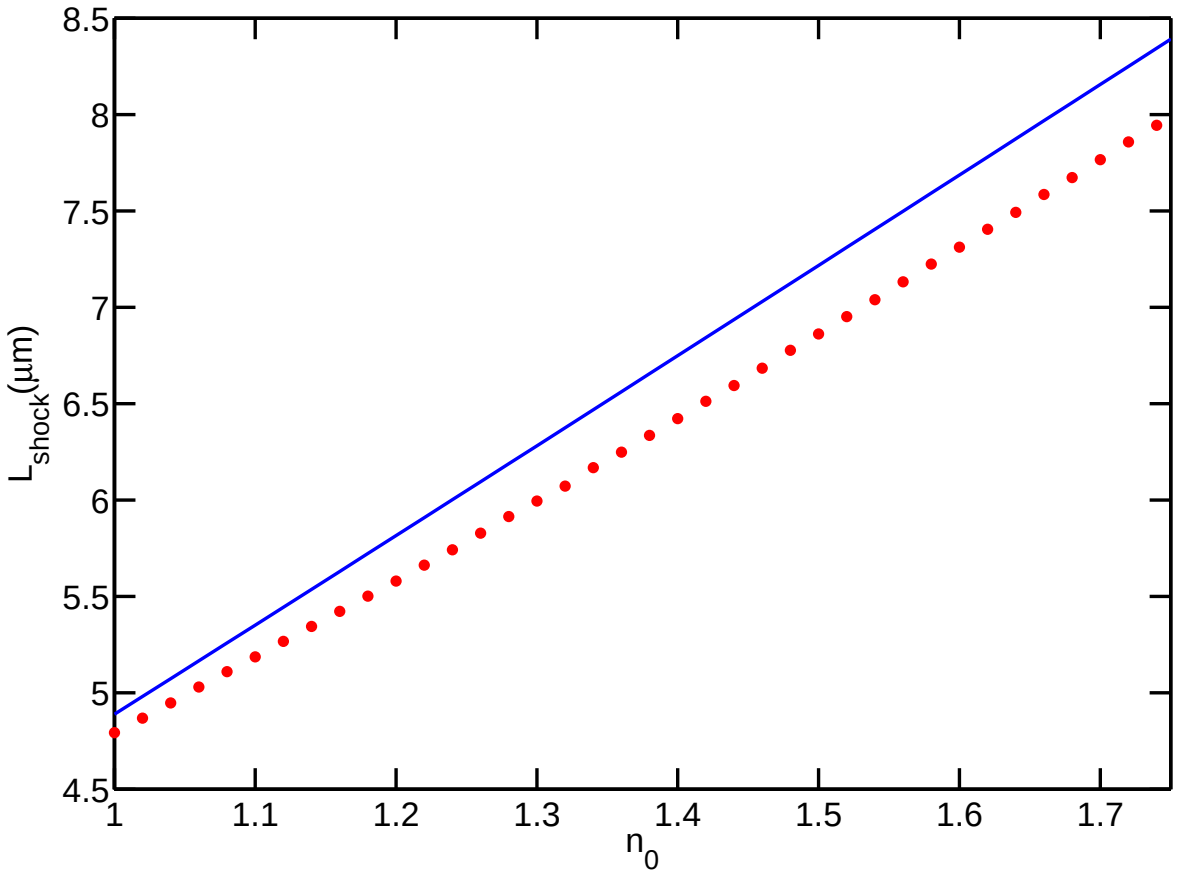

Figure 5.6: L_{shock} as a function of n_0. Numerical simulations (red dots) indicate the increase of L_{shock} with n_0, and are clearly supported by the MOC (blue solid).

5.3 Designer dispersion

Any realistic material has a smoothly varying $n(\omega)$, with many different phase and group velocities. Before attempting to understand the behaviour of CWS in such complex environments, it is helpful to build up a picture using designer dispersion profiles. These profiles help explain the interplay between dispersion and nonlinearity, and are easily controlled using the PSSD technique.

The simplest designer dispersion profile can be seen in fig. 5.7, and consists of a single refractive index step. The step, allows us to offset specific harmonics, by controlling its

magnitude (Δn). Furthermore, it enables a unique coherence length (L_C) to be defined e.g. $L_C = \frac{\pi}{k_3 - 3k_1}$ for a single refractive index step placed at ω_2. We might therefore expect a shock to develop when the SPM length (L_{SPM}) is considerably less than L_C, as the effect of dispersion will then be slight. Because our objective is to understand CWS in dispersive media, the size of the refractive index steps was chosen to be comparable to fused silica, $\Delta n_{1,3} \approx 0.06$, and $\Delta n_{3,5} \approx 0.12$ [38] (where the indices refer to the frequencies that have been off-set from each other).

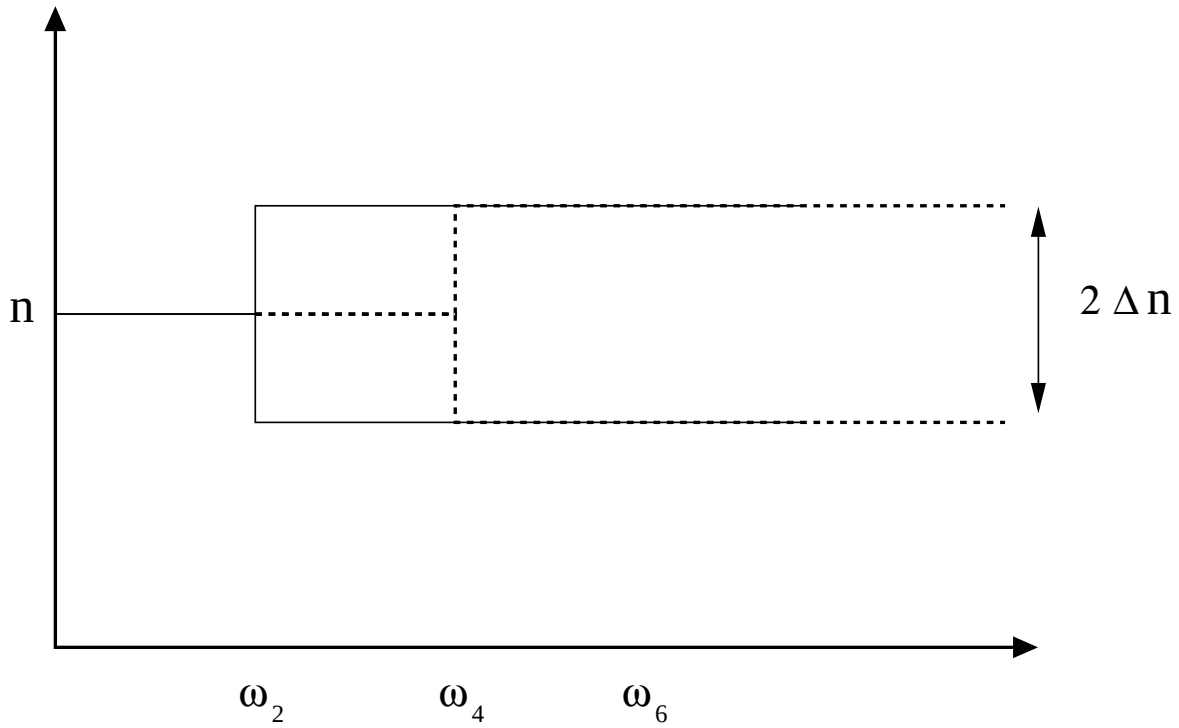

Figure 5.7: Schematic diagram of the simplest designer dispersion profile used. In this case, the dispersion profile consists of a single refractive index step placed either at ω_2 (solid line), or ω_4 (dashed line). In the former case, the step $\Delta n_{1,3}$ forces the first ω_1, and third ω_3 harmonics to travel at different phase velocities. Similarly, $\Delta n_{3,5}$, creates a phase velocity difference between frequencies ω_1 and ω_3, and anything higher.

Fig. 5.8 shows results from the simplest single-step profile, namely $\Delta n_{1,3}$ describing a refractive index step placed between ω_1 and ω_3 (see fig. 5.7). Varying the magnitude of the step led to well defined shocked regions, delineated by boundaries for large positive or negative step values. A shocked region can clearly be seen for pulses that have triggered the LDD method (red), and is also supported by the energy conservation method (blue) where the value of $\Delta E/E$ signifies the level of energy conservation. To understand whether pulse length plays a significant role in defining the shocked region, a cw case was also investigated. This involved using the same dispersive profiles as the pulsed case,

but with a single wavelength fitted to the time window. In a discrete Fourier transform this represents a monochromatic cw train. Results from this (black-dashed) indicate a slightly wider shocking region than the pulsed case, but nonetheless agree that CWS does not occur if the refractive index step becomes too large.

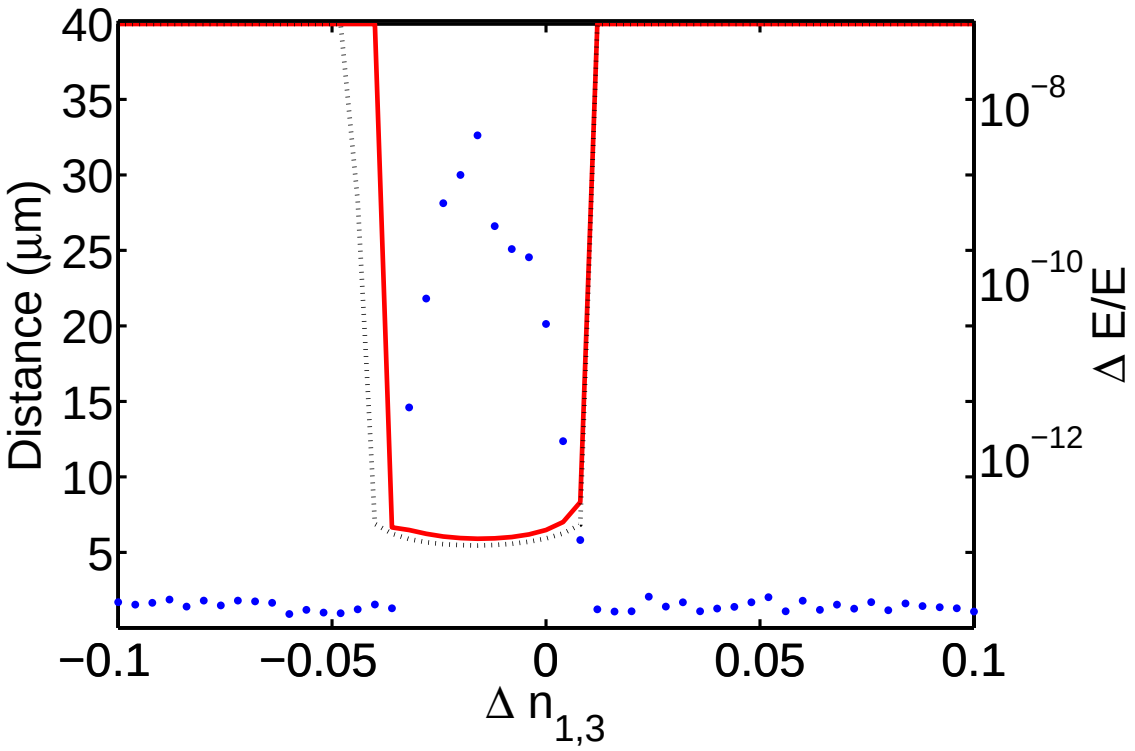

Figure 5.8: Carrier wave shocking for the single refractive index step ($\Delta n_{1,3}$). The solid (red) line refers to the LDD method, indicating that CWS is resistant to small refractive index steps. This result is supported by the energy conservation method (blue), plotted against the right hand axis (log scale). When a shock occurs, the energy conservation breaks down, supporting the LDD result. Failure to shock, results in the simulation propagating to the end of the simulation (40 microns) and a high level of energy conservation ($\Delta E/E \simeq 10^{-14}$). The asymmetry in the shocking region is discussed at the end of the section.

To investigate the tolerance of phase velocity mismatches at other parts of the spectrum, a refractive index step was then placed at ω_4. As in the previous case, a single-step was introduced ($\Delta n_{3,5}$) in order to offset the first and third harmonics (ω_1 and ω_3), from anything higher (see fig. 5.7). The results can be seen in fig. 5.9, and are in qualitative agreement with the $\Delta n_{1,3}$ case. As CWS is highly sensitive to the alignment of all of the harmonics, even offsetting the fifth (and higher) is enough to halt the process. Both $\Delta n_{1,3}$ and $\Delta n_{3,5}$ possess a unique L_C. The only significant difference apparent when

comparing the two cases ($\Delta n_{1,3}$ and $\Delta n_{3,5}$), is a slightly narrower shocking region in the $\Delta n_{3,5}$ case, and a small shift in the cw shocked region (relative to the pulse's shocked region).

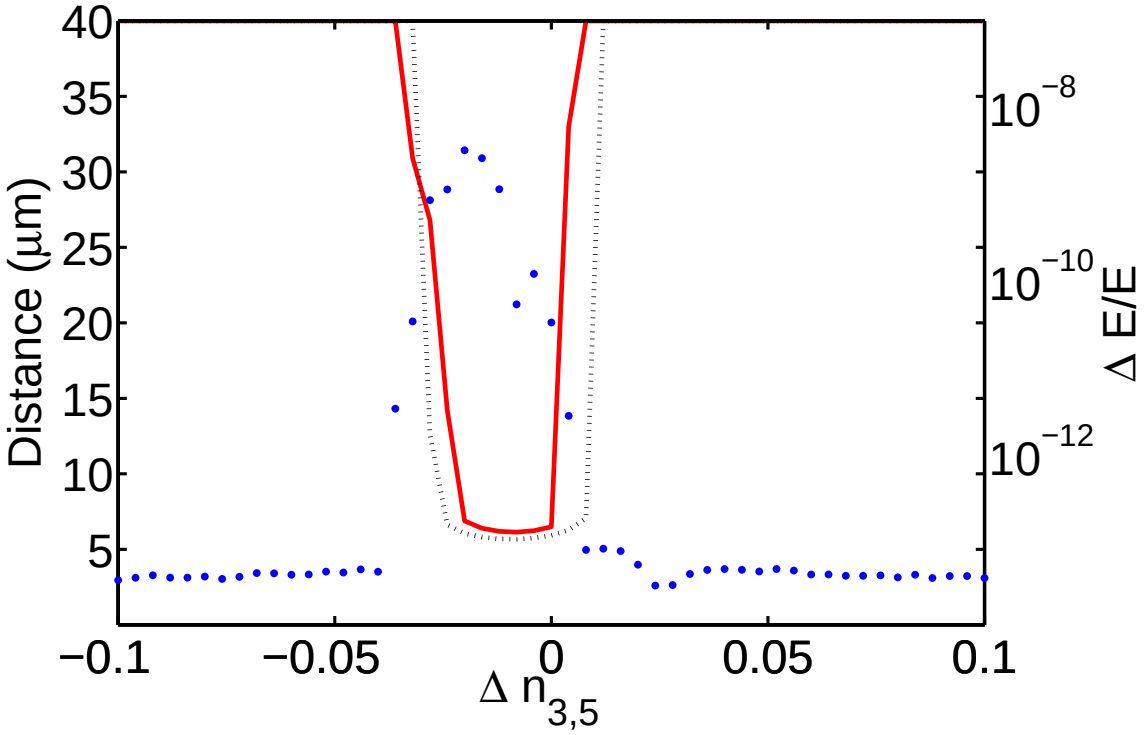

Figure 5.9: Carrier wave shocking for the single refractive index step $\Delta n_{3,5}$. The solid (red) line refers to the LDD method, and the (blue dots) refer to the energy conservation method ($\Delta E/E$). Both methods are in excellent agreement, displaying a slightly narrower shocking region than the $\Delta n_{1,3}$ step. The cw plot (dashed) appears slightly shifted to the right.

The next designer dispersion profile developed extended the idea of a single-step to multiple refractive index steps. Fig. 5.10 illustrates the steps placed between adjacent harmonics, where each step is of the same magnitude. Within a particular harmonic, there is a constant phase velocity. Offsetting adjacent harmonics more closely resembles a real material, where there is no longer a single coherence length.

Fig. 5.11 shows the results from the multi-step case $\Delta n_{1,3,5...}$. It is clear that the shocked region has become considerably narrower, because a small step now impacts on all the odd harmonics, introducing many different phase velocities (note the change in scale on the x-axis). There is however a well defined shock region as in the previous two cases.

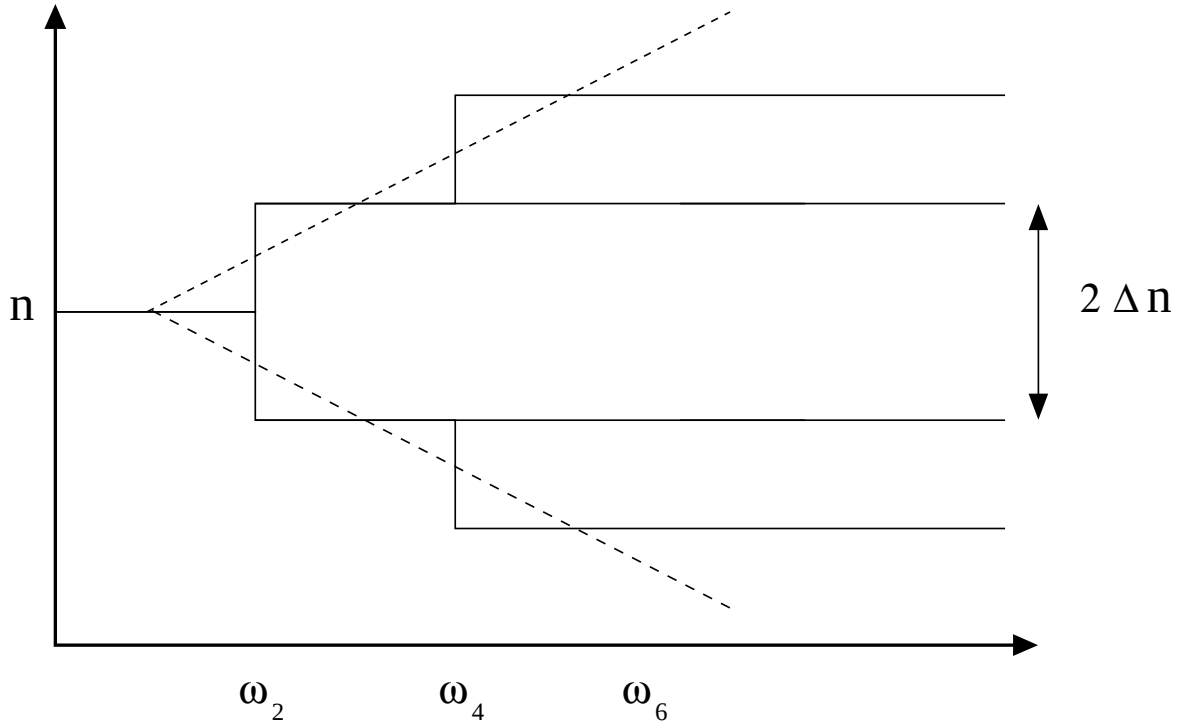

Figure 5.10: Schematic diagram of the multi-step (solid), and refractive index gradient (dashed) designer dispersion profiles. All steps are of the same size in the multi-step case. The refractive index gradients consist of straight lines, where the size of the gradient was scaled by the equivalent inter-harmonic step. In this case, group velocity dispersion (GVD) is present.

As before, the cw case differs only slightly from the pulsed case. It is important to note here that the cw case is approaching a realistic dispersion profile, as a flat refractive index step (within a harmonic), makes little difference when considering such a narrow bandwidth. It is only the phase-velocity at a particular frequency that is experienced within a cw limit. This provides some clues, as to what might happen in the case of a wideband pulse exposed to a refractive index gradient, as the difference between a pulse and the cw case tends to make little difference in CWS

The final dispersion profile applied is illustrated in fig. 5.10, and consists of a refractive index gradient. In this case, the size of the gradient was varied, to understand the effect of GVD on CWS. The effective nonlinear strength ($\chi^{(3)}E_0^2$) was also varied over the range of gradients, to investigate how this might affect the shocking region.

Fig. 5.12 shows the results of these simulations. In an analogy to the previous cases, shocking was found to be tolerant to shallow gradients, in the same way as it was for small steps. As expected, increasing the effective nonlinear strength, widens the shocking

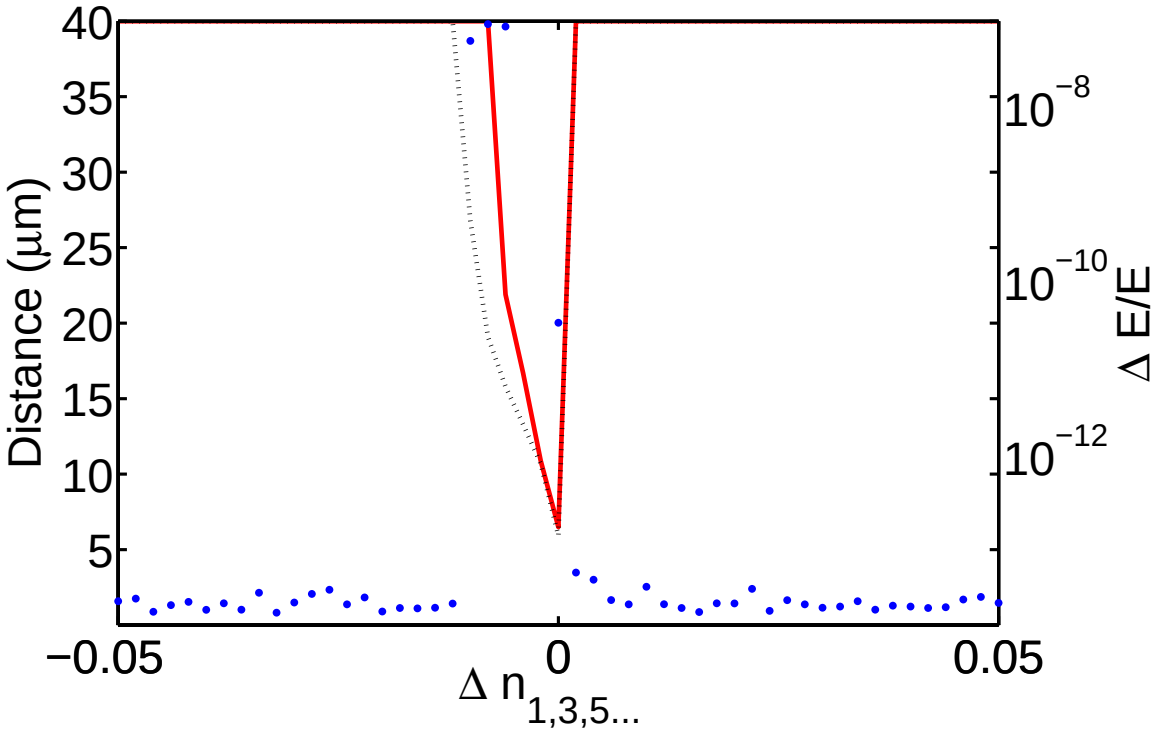

Figure 5.11: Carrier wave shocking in the multi-stepped case $\Delta n_{1,3,5...}$. In this case a much narrower shocking region occurs, as each harmonic is offset from its neighbour. This reduces the likelihood of shocking, as a small step now impacts on the entire harmonic cascade. The cw case (dashed) appears slightly more tolerant for anomalous dispersion (steps). Note the change in scale on the x-axis.

region, as the dispersion has less of an influence over a shorter L_{SPM}. Also evident from fig. 5.12, is the added complexity of the anomalous dispersion boundary (negative gradients). This sharply contrasts with the normal dispersion boundary (positive gradients), which always has a well defined cut-off.

The qualitative similarities in the above simulations indicate, that the dominant factor in the development of CWS is the inter-harmonic phase-velocity difference. CWS is tolerant to small phase-velocity mismatches, that can be induced in a variety of ways: single-step, multi-step, or refractive index gradient. Because CWS relies on the precise alignment of multiple harmonics (in order to achieve a near-vertical gradient), implementing even a small phase mismatch can be enough to halt the process. Though this is possible using a single-step, a multi-step profile, or a refractive index gradient tends to accentuate this effect. Once the phase-velocity mismatch is large enough, well defined shocked boundaries are produced, and are independently supported by the energy

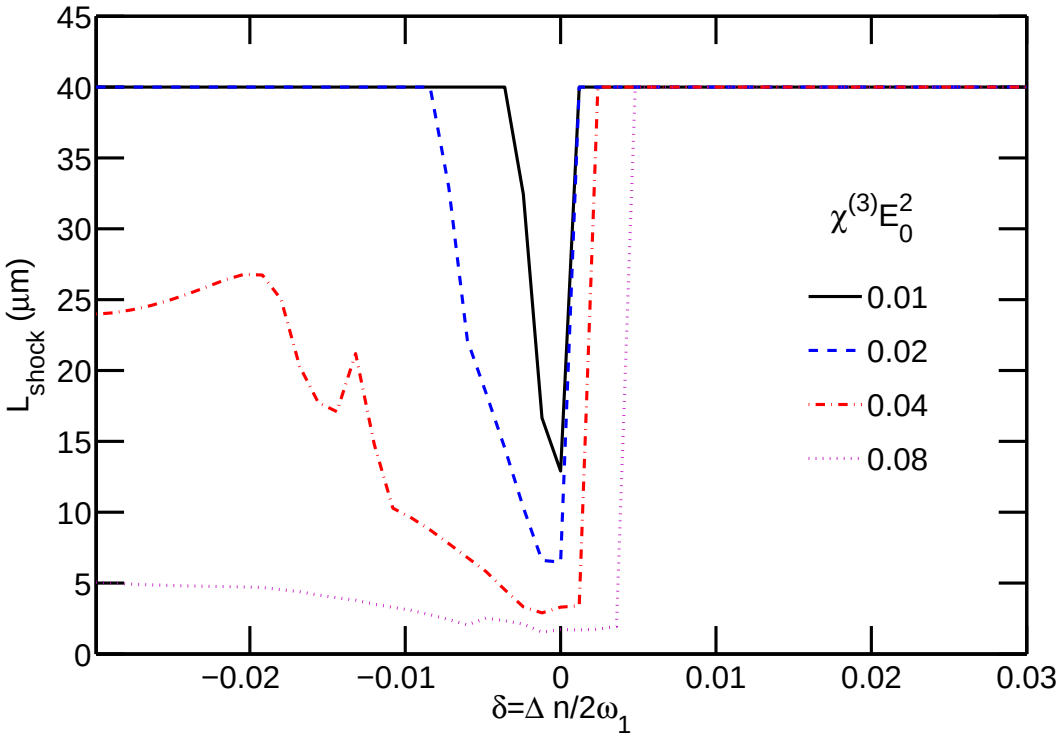

Figure 5.12: Shocking distance vs refractive index gradients (i.e. mismatch) δ, for a range of nonlinear strengths. An abrupt cut-off is visible at the normal dispersion boundary (right hand side), as opposed to the rather ill-defined anomalous dispersion boundary (left hand side). The complexity of the boundary appears to increase for higher effective nonlinearities. No cw results are shown, as these would be identical to the multi-stepped case of fig. 5.12.

conservation technique.

An important feature in all of the above dispersion profiles (section 5.3), is the asymmetry between the 'normal' and 'anomalous' dispersion regimes. The terms are used loosely here, to describe whether higher frequencies travel slower (normal), or faster (anomalous) with respect to each other. The above results clearly indicate that CWS is more tolerant to small amounts of anomalous dispersion, than normal dispersion, as all the shocked regions are centred with a bias towards the anomalous region (left). The explanation for this asymmetry lies in the intensity dependent refractive index of $\chi^{(3)}$ media. This predicts that the induced refractive index is greater at ω_1 than at ω_3. The effect of normal dispersion is therefore to add to this 'natural' phase mismatch, whereas anomalous dispersion cancels it out, thus promoting CWS. This is understood to be the mechanism behind the asymmetry of the shocked region.

The final result that is highlighted in all of the above profiles, is that there is very

little difference between CWS in the cw case, and in the pulsed case. This point has already been mentioned in section 5.2.4 in the context of the dispersionless regime, and is now apparent in the case of dispersion too.

5.4 Practicalities of CWS

So far the interplay between linear disperion and nonlinearity has been studied within the context of designer media. It has been shown, that offsetting the harmonics by a significant amount, is enough to arrest the CWS process. It is therefore reasonable to expect, that most realistic materials would suppress the process entirely. Moreover, the simulations so far have assumed an instantaneous nonlinear response, representing a significant approximation if the timescale involved tends to infinity. Another physical limitation to consider now, is the damage threshold of the material, which places an upper bound on the scalability of the effective nonlinear strength.

To assess whether CWS might occur in reality, there are three important questions to answer:

1. What constitutes a physical shock?

2. How would this be represented within a finite computational domain?

3. In what material might this be found?

In answer to the first question, it would be difficult to describe an infinite gradient predicted by our mathematical model. This is because the damage threshold of the materials we are considering would have long been surpassed before such gradients would have been realised. Generally speaking, a 'shock' or 'shock wave' denotes an abrupt change in the characteristics of the medium, e.g. a sonic boom, where a rapid change in air pressure occurs across a shock front. In the contexts of other fluid shocks e.g. water wave breaking, there is no physical reason to discount a multi-valued field as we so readily see with everyday hydraulic instabilities (ocean waves). In our case of optical polarisation, some other mechanism would have to exist in order to provide solutions to Maxwell's equations e.g. the sum of the linear and nonlinear polarisation components remaining finite. It is interesting to note that Rosen [36] did contemplate the ramifications of an optical carrier shock, concluding that it may act as a "source or sink for radiation field energy".

To answer the second question, we might continue to use the current LDD definition. This reliably converges to analytical solutions, whilst still dealing with finite gradients.

Thus by applying it to a real medium, we can investigate extreme Carrier-Wave Self-Steepening (CWSS) as the gradient approaches a shock.

Finally, the results from section 5.3, provide us with answers to the third question. The ideal material to probe would possess a weakly anomalous dispersion profile, with a very high nonlinear coefficient and damage threshold. Fused silica possesses the latter two qualities, and has been tested for CWS in [38, 39]. Most importantly, fused silica has a very flat dispersion profile compared to other media (see chapter III: fig. 3.3 for a plot of the Sellmeier equation), so that the phase velocity mismatch between adjacent harmonics is small.

To investigate whether CWS could be physically realised using the LDD measure, the intensity of the E field was increased to above the damage threshold (50×10^{12} W/cm^2) of fused silica, without triggering a numerical shock. CWSS did occur, producing visibly steepened pulse profiles. Fig. 5.13 shows the increasing gradient as a function of distance and intensity, up to the damage threshold. The maximum gradient occurs at $L \simeq 7\mu$m, where the various harmonics are most efficiently aligned. This alignment does not persist for long, because decoherence then occurs, reducing the maximum field gradient. Incorporating nonlinear dispersion into the model would moderate these effects even more, further decreasing the gradients.

According to our definition of a shock (LDD), CWS would therefore not occur in fused silica, and is unlikely to occur in any other real medium. On the other hand, CWSS would take place and has been predicted in [38]. With advances in media with tailored dispersion profiles, it might be possible to engineer a medium that can support extreme self-steepening, approaching a shock. As more harmonic orders are necessary to increase the field gradient, phase-matching over a progressively wider bandwidth becomes necessary. Fortunately, only a narrow band at each harmonic is needed, to phase-match for extreme CWSS in the cw case, but nonetheless this remains a formidable task. Materials with weakly anomalous dispersion, and extremely high damage thresholds provide the best route to achieving very steep field gradients, as L_C plays a diminishingly important role as L_{SPM} dominates.

5.5 Conclusion

A mathematical model for Carrier Wave Shocking has been developed using the Method of Characteristics. This has enabled the development of accurate numerical models and a shock detection scheme (LDD) that converges to the predicted shocking distance. CWS has also been shown to be weakly sensitive to CEP and pulse length for single-cycle

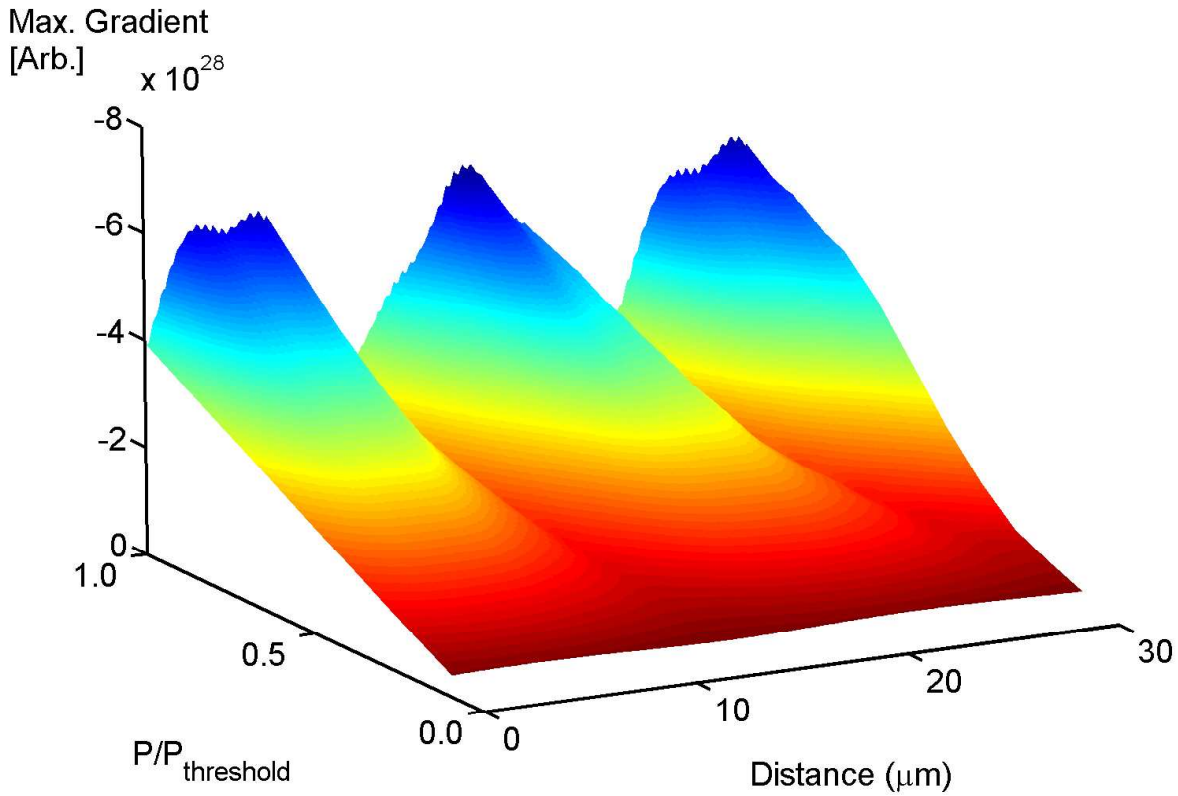

Figure 5.13: Maximum field gradient in fused silica at 0.1 micron intervals for intensities ranging from $1/10^{th}$ of the damage threshold, to the damage threshold. The surface indicates the maximum gradient at a particular distance for a given intensity. The highest gradient achieved occurs when the harmonics are most efficiently aligned.

pulses, though in general there is little difference between few-cycle pulses and a cw field.

The interplay between linear and nonlinear dispersion has been investigated using a variety of novel dispersion profiles. These profiles have enabled the CWS process to be understood in terms of well defined coherence lengths and phase mismatches. They have also helped explain the asymmetry between normal and anomalous dispersion, through the intensity dependent refractive index. The results indicate well defined shocking regions that are supported by the energy conservation measure. CWS has been shown to be highly sensitive to inter-harmonic phase-velocity differences. These can be applied through refractive index steps (single/multiple), or refractive index gradients.

Applying the LDD method to fused silica reveals that CWS would not occur. Even at intensities equal to the damage threshold, and assuming an instantaneous nonlinearity, only extreme CWSS is possible. The multiple coherence lengths present in real media, prevent the development and alignment of higher harmonics necessary for a shock. In-

cluding a finite response, would only moderate the field gradients further. CWSS may prove useful in the field of High Harmonic Generation (HHG) and this is discussed in the next chapter.

Chapter 6

Carrier Shaping and Applications to HHG

6.1 Introduction

The concept of Carrier Wave Shocking (CWS) in $\chi^{(3)}$ media was discussed in chapter V, and involves the self-steepening of the optical carrier due to third order nonlinearity. In this chapter a novel carrier wave self-steepening mechanism is reported, involving amplitude dependent self-steepening in quadratic media [41]. This phenomenon leads to CWS in the dispersionless limit, and (as in the $\chi^{(3)}$ case) can be predicted using the method of characteristics (MOC). These predictions are supported by a variety of numerical methods, including the bandwidth unlimited *G-envelope* developed in chapter IV. In fact, it is shown that CWS can be generalised to any nonlinear order (within the dispersionless limit).

The novel shocked waveforms produced at different nonlinear orders exhibit interesting symmetry properties. For example, $\chi^{(2)}$ CWS waveforms do not display inversion symmetry. These atypical properties have useful applications in High Harmonic Generation (HHG), increasing the spectral cut-off, and potentially generating shorter attosecond bursts. This work goes beyond current experimental schemes, where at most, two-colour fields are used to drive the HHG process [66–68].

The chapter begins with the generalised formula for predicting the shocking distance based on the MOC, for any arbitrary combination of nonlinearities. These results are then compared with numerical simulations for the case of quadratic media. Quadratic media have sparked a lot of recent interest because of the ability to control their nonlinearity [69–71]. However, these models looked at envelope descriptions of the E field, and did not involve shock solutions. Many of the possible nonlinear combinations are unrealistic,

although those based on second- and/or third-order processes are reasonable.

In practice, there are many potential pitfalls when trying to achieve $\chi^{(2)}$ CWS, including dispersion, birefringence, and the possibility that the plane of polarisation of the generated harmonic is different to that of the incoming field. Though CWS itself is not expected to occur in a real medium, the Carrier-Wave Self-Steepening (CWSS) preceding a shock, remains a viable option and could prove useful in HHG, where the carrier gradient of the driving pulse plays an important role. The increase in carrier gradient with pulse power, is tested up to the damage threshold in various media. CWSS pulses are then used to drive a HHG model, in order to examine their effects in terms of harmonic yield and cut-off.

6.2 Theory

Our starting point is the pair of 1D sourceless, plane polarised Maxwell's equations for a field propagating in the z direction, namely

$$\begin{aligned} \frac{\partial E_x}{\partial z} &= -\mu_0 \frac{\partial H_y}{\partial t} \\ -\frac{\partial H_y}{\partial z} &= \frac{\partial D_x}{\partial t}, \end{aligned} \tag{6.1}$$

where E_x, H_y and D_x are the electric, magnetic and electrical displacement fields respectively. Ignoring the tensor nature of the nonlinear coefficients, and assuming the polarisation of the generated field is the same as that of the incoming field yields:

$$D = \epsilon_0 \left(E + \chi^{(1)} E + \sum_{m>1} \chi^{(m)} E^m \right), \tag{6.2}$$

where $\chi^{(m)}$ refers to the m^{th} order nonlinear susceptibility, and the medium is assumed to be dispersionless (the subscripts are now dropped for brevity). This leads to the second-order wave equation

$$c^2 \frac{\partial^2 E}{\partial x^2} = n_0^2 \frac{\partial^2 E}{\partial t^2} + \sum_{m>1} \chi^{(m)} \frac{\partial^2 E^m}{\partial t^2}, \tag{6.3}$$

which can be factorised, such that

$$\left(\frac{\partial}{\partial t} + v(E) \frac{\partial}{\partial x} \right) \left(\frac{\partial}{\partial t} - v(E) \frac{\partial}{\partial x} \right) E = 0, \tag{6.4}$$

and the characteristic velocity $v(E)$ is,

$$v(E) = \frac{c}{\sqrt{n_0^2 + \sum_{m>1} m\chi^{(m)} E^{m-1}}}. \tag{6.5}$$

Using the same technique that was applied in chapter V, it is possible to obtain a generalised formula for the shock solutions, namely

$$L = -\frac{2c\sqrt{n_0^2 + \sum_{q>1} q\chi^{(q)} E^{q-1}}}{\sum_{m>1} m\chi^{(m)} \frac{dE^{m-1}}{dt}}. \tag{6.6}$$

The shocking distance (L_{shock}) is now the minimum value of L in eq(6.6), i.e. $L_{shock} = \mathrm{Min}[L]$. In the case of a $\chi^{(2)}$ medium, the formula predicts CWS at a distance of

$$L_{shock} = \frac{c\sqrt{n_0^2 + 2\chi^{(2)}E}}{\chi^{(2)}} \mathrm{Min}\left[-\frac{1}{\frac{\mathrm{dE}}{\mathrm{dt}}}\right] \tag{6.7}$$

contrasting with the $\chi^{(3)}$ case (chapter V), where $L_{shock} \propto \mathrm{Min}[-\frac{1}{\mathrm{dE^2/dt}}]$. An example of the E field profile at L_{shock} can be seen in fig. 6.1, for the case of a dispersionless $\chi^{(2)}$ medium.

It is also instructive to think of how the self-steepening process manifests itself in the frequency domain, where production of harmonics occurs during the reshaping and steepening of the time domain profile. Let us consider the early stages of the process, in a $\chi^{(2)}$ medium, with a sinusoidal E field ($E = E_0 \sin(\omega_0 t)$). We have from eq(6.2)

$$\begin{aligned} D &= \epsilon_0(n_0^2 E + \chi^{(2)} E^2) \\ &= \epsilon_0(n_0^2 E_0 \sin(\omega_0 t) + \chi^{(2)} E_0^2 \sin^2(\omega_0 t)) \\ &= \epsilon_0(\frac{\chi^{(2)} E_0^2}{2} + n_0^2 E_0 \sin(\omega_0 t) - \frac{\chi^{(2)} E_0^2}{2} \cos(2\omega_0 t)). \end{aligned} \tag{6.8}$$

We know from eq(6.1) that H depends on the derivative of D, and therefore that the new EM field contains both fundamental and second harmonic components. The mixing of the fields on the next step (assuming a discrete process), produces frequencies ranging from ω_0 to $4\omega_0$. The build-up of the harmonic cascade as the pulse approaches L_{shock} can be seen in fig. 6.2. This spectrum differs from that of $\chi^{(3)}$ self-steepening, where only odd harmonics are present. It is the presence of even harmonics that always causes

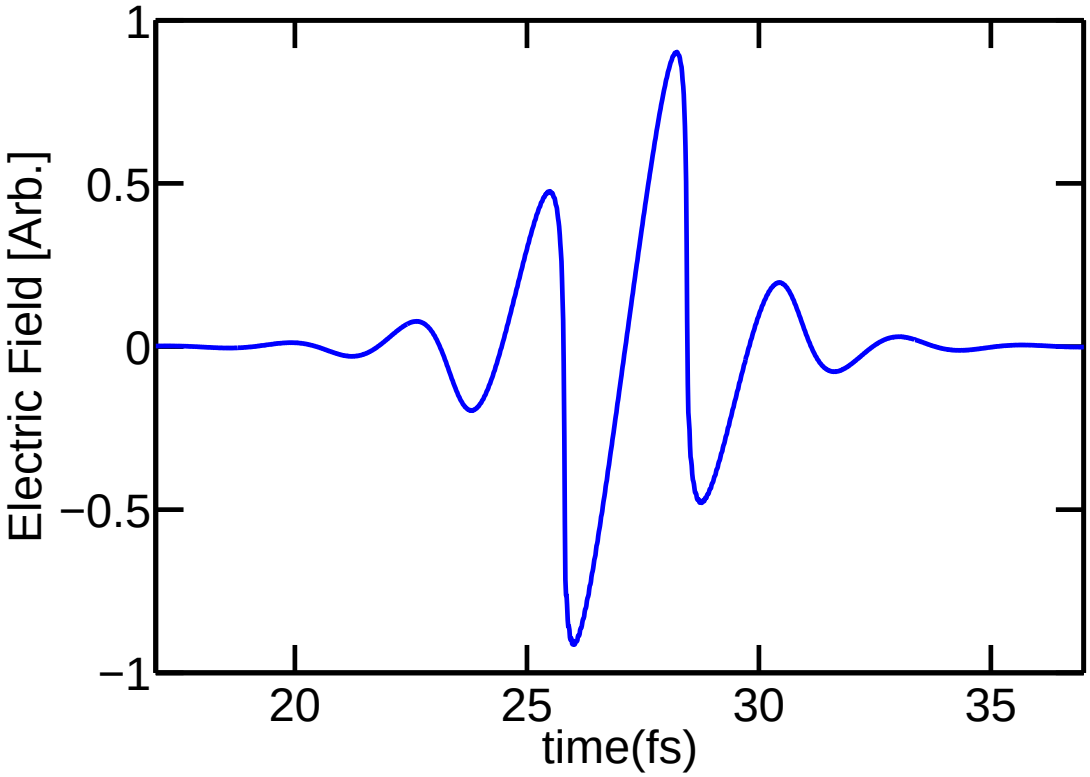

Figure 6.1: Electric field profile of a few-cycle pulse at the point of shocking: $E(t) = E_0 \sin(\omega_0 t + \phi)\text{sech}(0.3\omega_0 t)$, $(\chi^{(2)}E_0 = 0.02)$. Note the skewed shape of the pulse and the sawtooth profile. On either side of the central carrier oscillation the field gradient is near vertical, causing a shock (LDD). The smallest unit of repetition here is 2π rads, as opposed to π rads in the $\chi^{(3)}$ case. This has consequences in driving HHG, and will be discussed later.

asymmetry in the time domain profile.

6.3 Detection of $\chi^{(2)}$ CWS

Using the LDD method [39] (chapter V section 5.2.3), CWS in $\chi^{(2)}$ media was investigated for different pulse lengths, and differing Carrier Envelope Phase (CEP) offsets (in the few-cycle limit). This is because both of these attributes are crucial when driving HHG. The results were in qualitative agreement with those of $\chi^{(3)}$ CWS, and were confirmed at the analytically predicted distance. As in the $\chi^{(3)}$ case, L_{shock} was found to be sensitive to both pulse length and CEP. Fig. 6.3 illustrates this feature, where L_{shock} is compared to the prediction of eq(6.7), for different pulse lengths. The initial pulse profile was $E(t) = E_0 \sin(\omega_0 t + \phi)\text{sech}(0.3\omega_0 t)$, where $\chi^{(2)}E_0 = 0.02$.

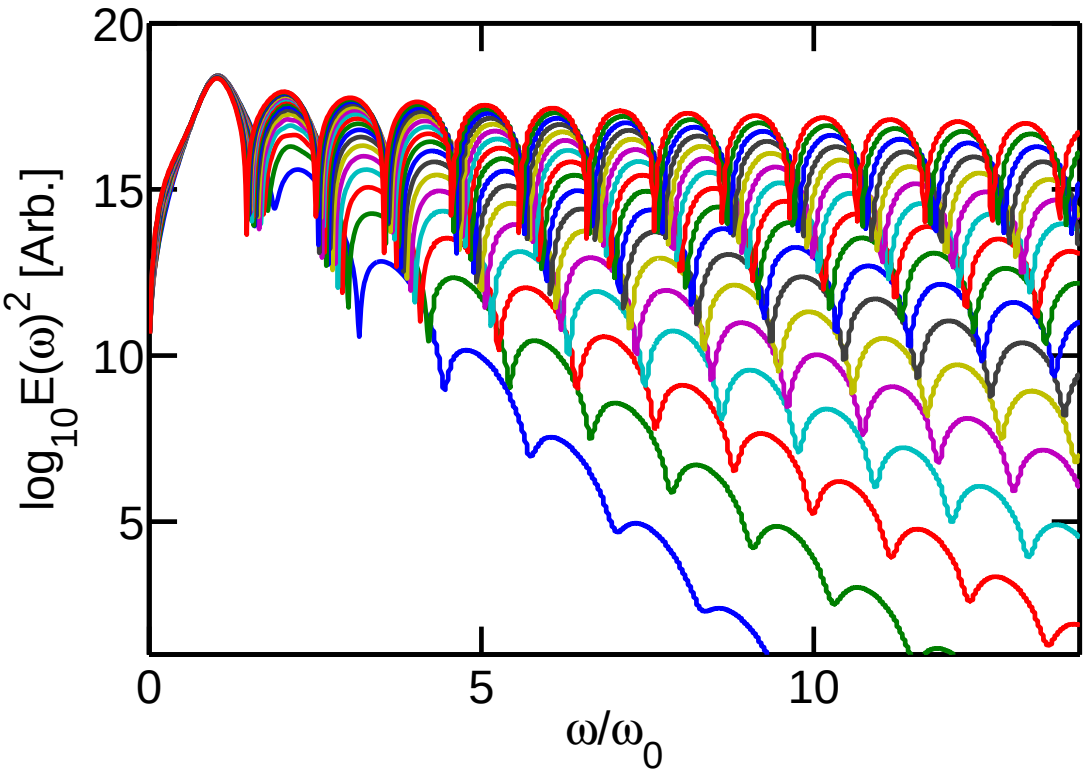

Figure 6.2: Log plot of $E(\omega)^2$ at half micron intervals, approaching L_{shock} in a $\chi^{(2)}$ material (taken from fig. 6.1). The curves flatten out as progressively more harmonics are generated close to L_{shock}. The spectrum contrasts with $\chi^{(3)}$ shocking, where only odd harmonics are produced (see fig. 6.6).

CEP sensitivity can be seen in fig. 6.4, where L_{shock} decreases as the pulse approaches a cosine ('cosine' refers to $\phi = \pi/2$ in this case, where a maximum occurs at the envelope peak). This is expected, as a cosine pulse has the highest peak intensity, producing the smallest $-dE/dt$. This differs from $\chi^{(3)}$ CWS where $L_{shock} \propto$ Min$(-\text{EdE/dt})^{-1}$, producing a more complicated CEP dependence within the few-cycle regime.

6.4 Shocked waveforms

Following the predictions of eq(6.6), this section demonstrates some novel shocked waveforms. The waveforms have been generated in dispersionless media, and are included to highlight the symmetry properties at different nonlinear orders. This helps us to understand their benefits when applied to HHG.

The PSSD method [32] was used for this task, along with the *G-envelope* method (see

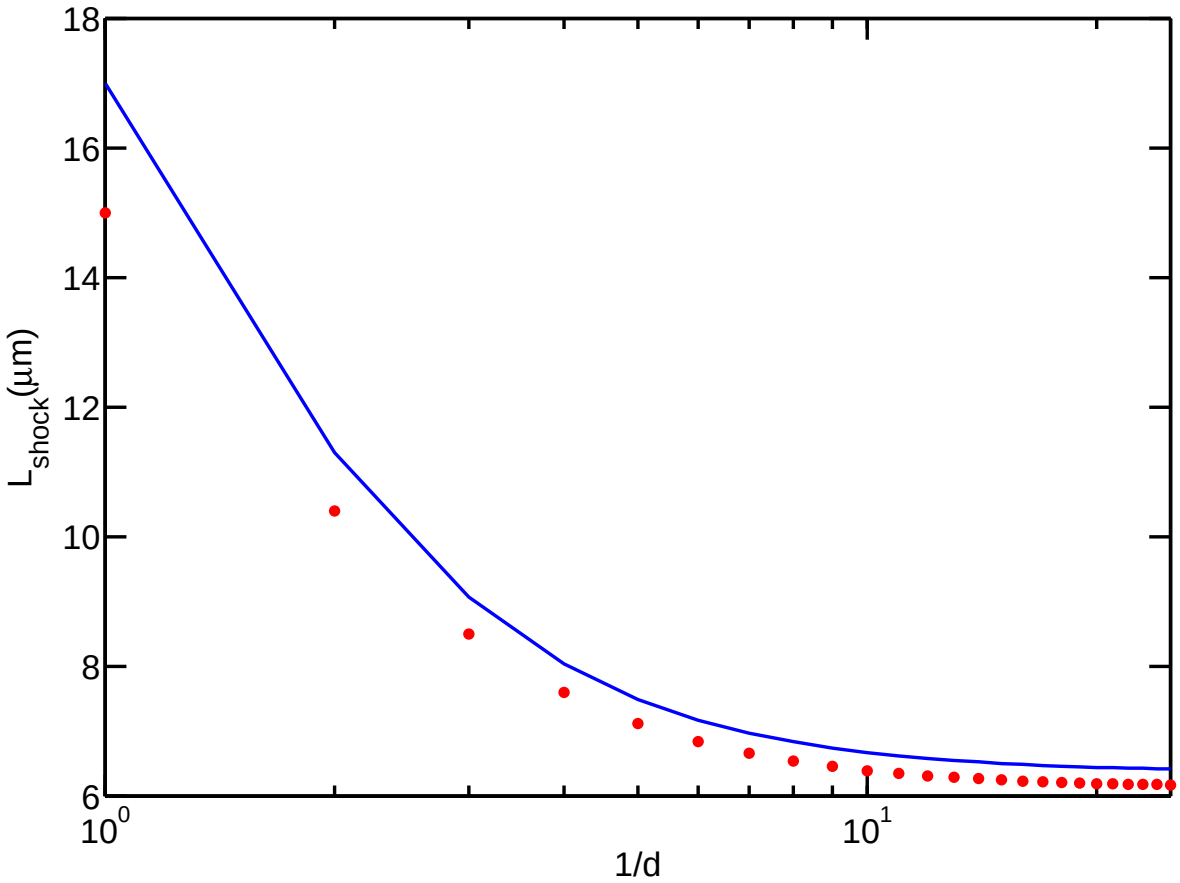

Figure 6.3: Comparison of shocking distance in $\chi^{(2)}$ media with respect to initial pulse length (d) for the case $E(t) = E_0 \sin(\omega_0 t)\mathrm{sech}(\mathrm{d}\omega_0 \mathrm{t})$. The blue solid curve represents the analytical result and the red dotted curve represents the numerical results (LDD). The shocking distance approaches an asymptotic limit for the cw case.

chapter IV). CWS was found very close to the predicted distance for all nonlinear orders tested. These simulations also emphasise the accuracy of bandwidth unlimited envelope methods [35], where the E field is oscillating on a very fast timescale. A theoretical $\chi^{(4)}$ CWS waveform has been included to illustrate the generality of the formula and to demonstrate the breaking of the inversion symmetry at even nonlinear orders. It should be emphasised, that its inclusion is not meant as a realistic suggestion, but rather to highlight the connection between E field symmetry/asymmetry and the nonlinear order.

The shocked waveforms in fig. 6.5 display some striking properties. In particular, figs. 6.5 (a) and (c) which both have an underlying sawtooth shape, where the smallest unit of repetition is 2π rads. This is because even harmonics cause the pulse to be asymmetric on inversion. In such cases, positive lobes lean to later times whilst negative lobes lean to earlier times. The induced refractive index now affects positive and negative half-cycles

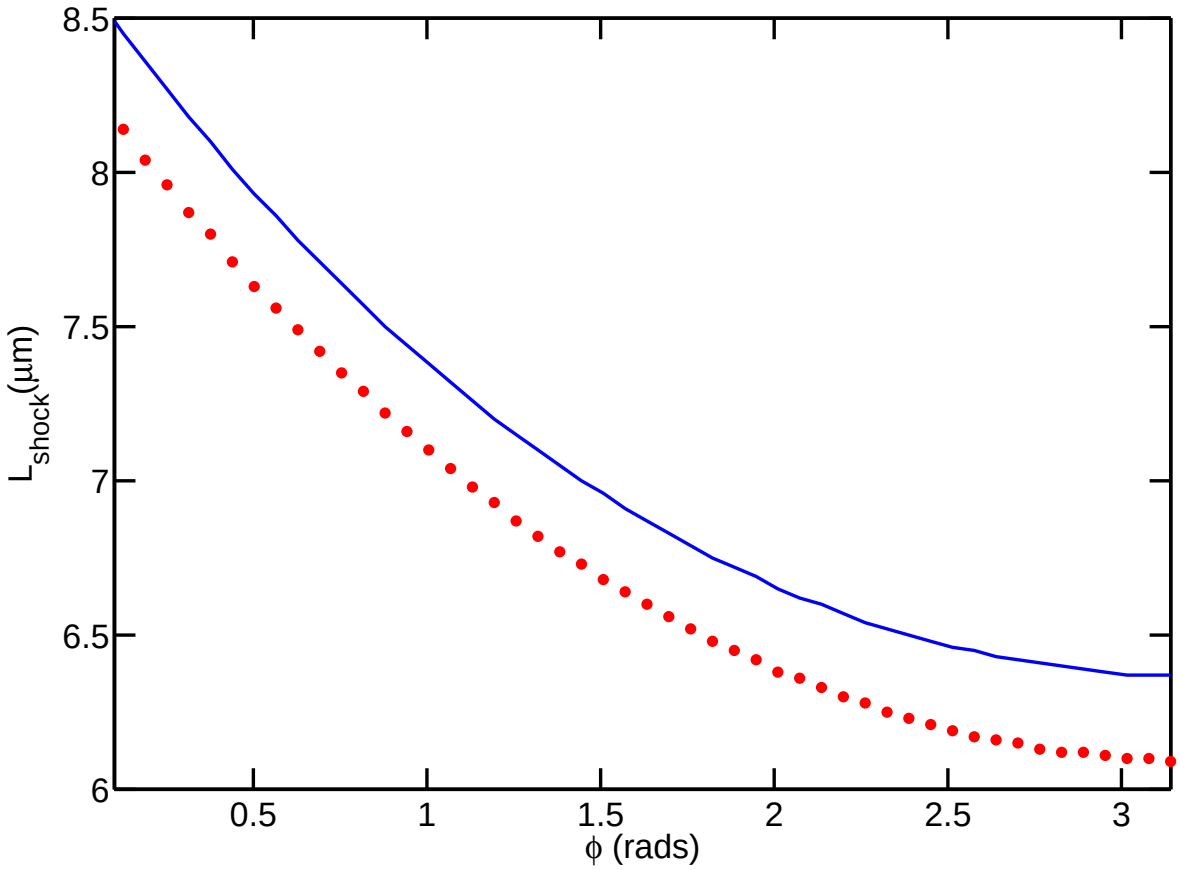

Figure 6.4: Comparison of shocking distance in $\chi^{(2)}$ media with respect to CEP (ϕ). The solid curve (blue) represents the analytical result and the dotted curve (red) represents the numerical results (LDD). The two curves are in excellent agreement, showing the expected change in shocking distance due to CEP.

differently. (Both dE/dt and dE^3/dt can take on positive and negative values.)

This contrasts with fig. 6.5 (b), where both positive and negative half-cycles lean to later times, as the characteristic change in velocity depends on dE^2/dt, affecting both positive and negative E values equally. The smallest unit of repetition therefore becomes π. Another noteworthy feature is that, for lower order nonlinearities, *all* the carrier oscillations undergo noticeable change, whereas at higher orders, the majority of the reshaping occurs on the most intense carrier(s).

The agreement between PSSD (blue) and *G-envelope* (red), over such a vast bandwidth is remarkable. The curves in fig. 6.5 almost exactly overlay each other, testifying to both the accuracy of a uni-directional method and, a bandwidth unlimited envelope. For such consistency to occur, the uni-directional approximation (chapter IV), and a wideband envelope calculation must both reproduce Maxwell's equations to a very high

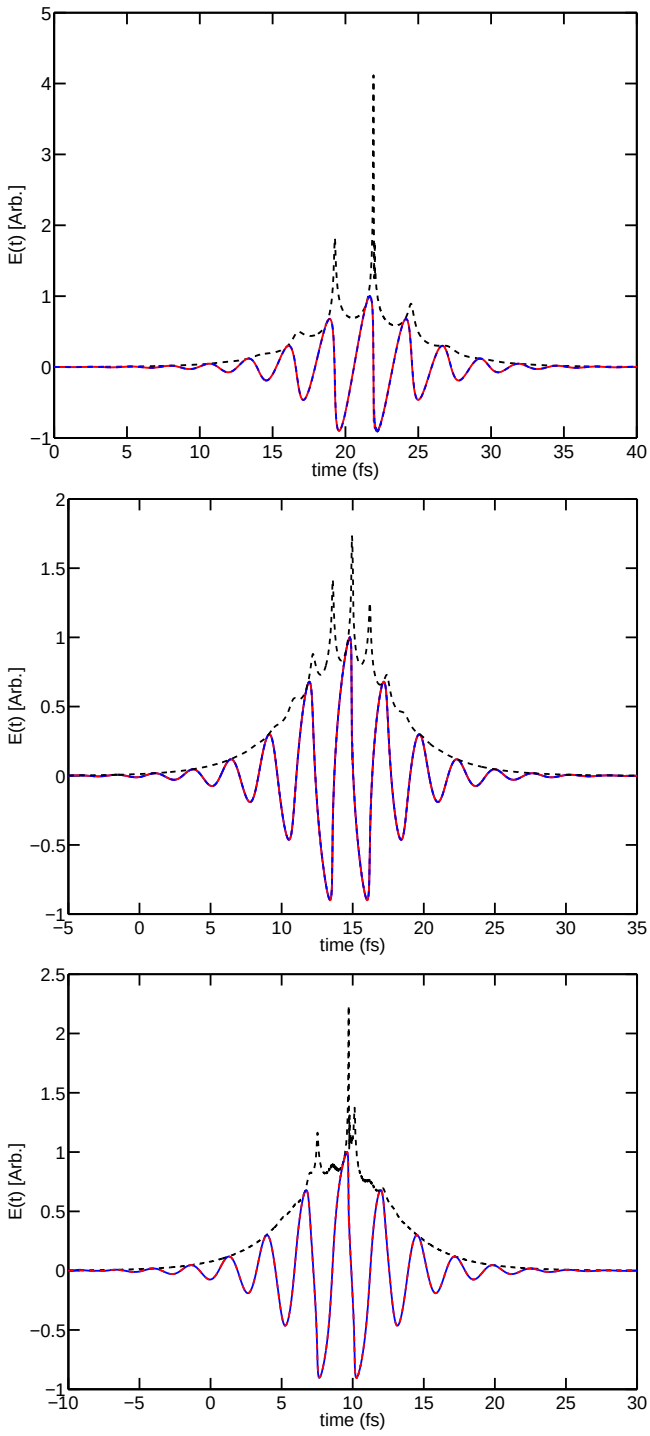

Figure 6.5: CWS for different nonlinearities: PSSD (blue-dashed), *G-envelope* (red-dashed), and complex envelope (black-dashed). (top) $\chi^{(2)}$: The sawtooth shape is characterised by near vertical gradients on either side of the carrier, as $\pm E$ move to higher/lower times respectively. (middle) $\chi^{(3)}$: All the carrier oscillations 'lean' in one direction, as both $\pm E$ move to higher times. (bottom) $\chi^{(4)}$: Like the $\chi^{(2)}$ case, the inversion symmetry is broken as $\frac{dE^{(3)}}{dt}$ can be positive/negative.

degree of accuracy. The magnitude of the complex envelope has also been plotted in fig. 6.5 (black-dashed), demonstrating CWS from another perspective. Because the carrier has been removed from the picture, all the relevant information is contained in the complex envelope, and is responsible for its complicated structure. The highest frequency on the envelope is always just one harmonic less than it would be in a carrier picture. The LDD method did not consistently work with the complex envelope representation, therefore *G-envelope* was propagated to the same distance as PSSD where it was then stopped.

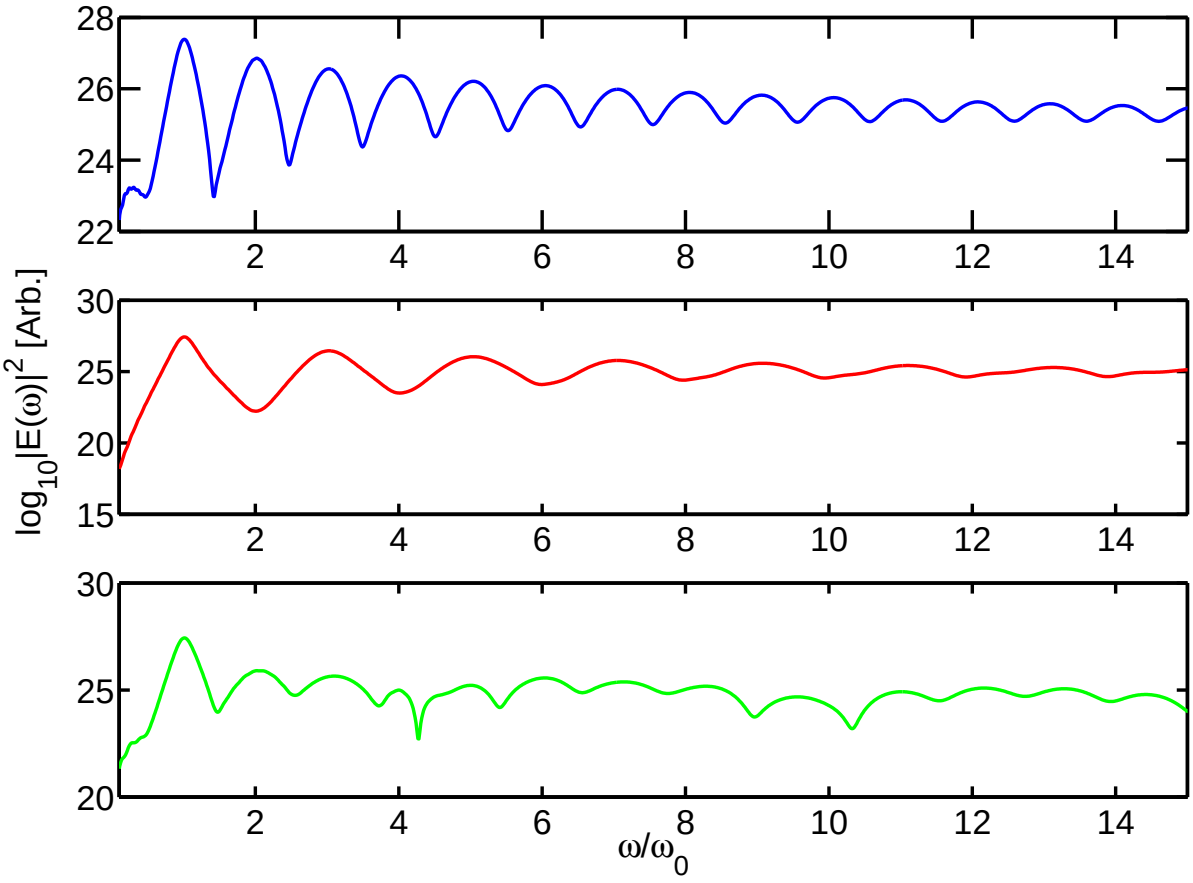

Figure 6.6: Intensity spectra for figs. 6.5, $\chi^{(2)}E_0 = \chi^{(3)}E_0^2 = \chi^{(4)}E_0^3 = 0.02$. (top) Harmonic distribution for $\chi^{(2)}$ CWS. The presence of even harmonics is clearly visible. (middle) Harmonic distribution for $\chi^{(3)}$ CWS. In this case only odd harmonics are present. (bottom) Harmonic distribution for $\chi^{(4)}$ CWS. The intensity distribution here contains features from both of the previous spectra.

Though all the profiles in fig. 6.5 have triggered a shock, they occurred at different distances, underlining another important aspect of the CWS model. L_{shock} is reduced at higher nonlinear orders for the same effective nonlinear strength $\chi^{(2)}E_0 = \chi^{(3)}E_0^2 =$

$\chi^{(4)}E_0^3 = 0.02$. The reason being, that at higher nonlinear orders, the steepest gradients are approached faster. This can be seen from the frequency distribution at L_{shock} in fig. 6.6. The presence of only odd harmonics in the case of $\chi^{(3)}$ is also re-emphasised.

The rate of steepening impacts on the practical applications of carrier-steepened waveforms. Because dispersion is present in real media, for maximum steepening, a higher order nonlinearity would be beneficial. Unfortunately, the disadvantage of this is that the effective nonlinear strength is generally diminished at higher orders. Thus, $\chi^{(2)}E_0$ is generally larger than $\chi^{(3)}E_0^2$. The symmetry properties of the medium also play an important part in the CWSS process, as we shall see in section 6.7.

6.5 Wavelet representation

Wavelets have been used elsewhere in nonlinear optics because of the clear and intuitive picture they provide [72]. A wavelet cannot be exclusively defined in time or frequency space, but rather exists is a mixed basis. The mother wavelet can be manipulated through a series of either scaling or transformation operations, into various daughter wavelets. These daughter wavelets can be used to decompose a function into the desired wavelet basis. The higher frequency wavelets provide information on a faster timescale, and thus allow high frequency regions of the pulse to be pinpointed. This would not be possible using a Fourier basis, as all frequencies are present at all times.

Wavelets are particularly useful when describing very sharp profiles or shocked features. In this case the Moorlet 5 wavelet was used to analyse the shocked waveforms from fig. 6.5, displaying where the highest frequency content was present. The wavelet plot also highlights the contrasting symmetry of $\chi^{(2)}$ and $\chi^{(3)}$ CWS (where the high frequency content occurs once per cycle vs twice).

6.6 Practicalities of $\chi^{(2)}$ self-steepening

6.6.1 Real Media

The theory discussed so far, has relied on an idealised dispersionless medium with instantaneous nonlinear response. As in the previous chapter (chapter V: $\chi^{(3)}$ CWS), we would not expect a physical shock to occur, but instead consider how $\chi^{(2)}$ CWSS pulses might be generated, and the properties they would have. Chapter V dealt with the interplay of linear and nonlinear effects [39], and because those considerations have already been covered, they are not repeated here. This section discusses some important

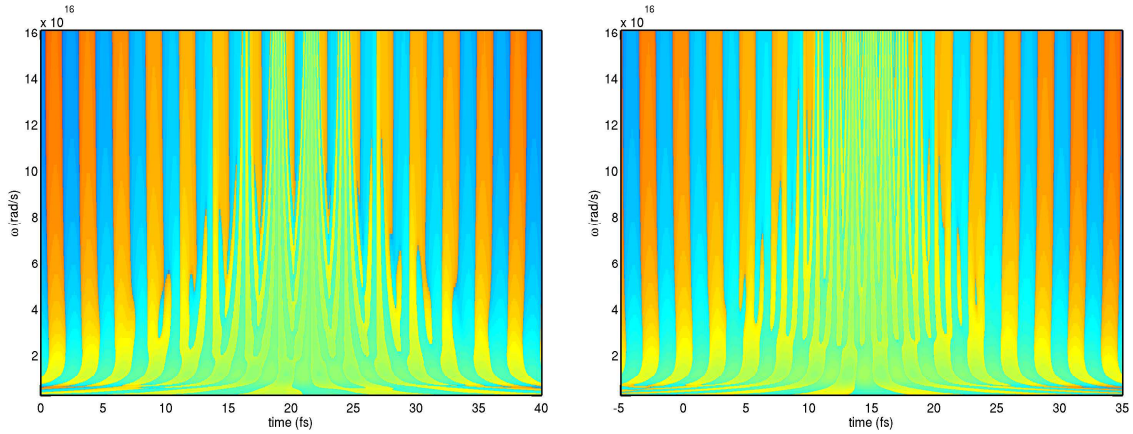

(a) Wavelet transform of $\chi^{(2)}$ CWS. The breaking of the inversion symmetry using a wavelet basis can clearly be seen, where each half-cycle becomes distinct, contrasting to $\chi^{(3)}$ CWS. The highest frequency wavelets are visible around the most intense carrier.

(b) Wavelet transform of $\chi^{(3)}$ CWS. High frequency wavelets can be seen on both half-cycles of the carrier, emphasising the inversion symmetry. The highest frequencies occur where the intensity is highest as in fig. (a) above.

Figure 6.7: Wavelet transforms of $\chi^{(2)}$ and $\chi^{(3)}$ CWS using a log scale for the field, where *sgn* was applied separately ($\pm$), to deal with the negative field values. The greatest positive and negative values are red and blue respectively. The waveforms were taken from fig. 6.5 (a) and (b).

consequences of $\chi^{(2)}$ self-steepening, including results from real media where the degree of carrier-steepening is considered at the damage threshold (power). The extent of the carrier-steepening can then be compared to the $\chi^{(3)}$ case from the previous chapter.

Linear dispersion generally makes phase-matching the entire harmonic cascade impossible, so it is necessary to consider the level of steepening that can be accomplished in practice. Steepening will take place where there is phase-matching, but in general linear dispersion will dominate after a short distance, stopping the exponential growth of the field gradients as the harmonics become out of phase. Fig. 6.8 shows the maximum gradient at the damage threshold of MgO:LN as a function of distance. In less than a micron, dispersion has reduced the maximum gradient, making extreme CWSS unlikely.

Another important consideration for $\chi^{(2)}$ interactions is the plane of polarisation of the generated harmonics. This is generally different to that of the driving field, adding the further complication of birefringence. Fortunately, materials exist where the nonlinear plane of polarisation is the same as that of the driving field e.g. $e + e \rightarrow e$ in lithium niobate [46]. This may help begin a harmonic cascade, and is one reason why MgO:LN was chosen as a comparison to fused silica.

The maximum gradient achieved at the damage threshold of MgO:LN was $\simeq$ 10%

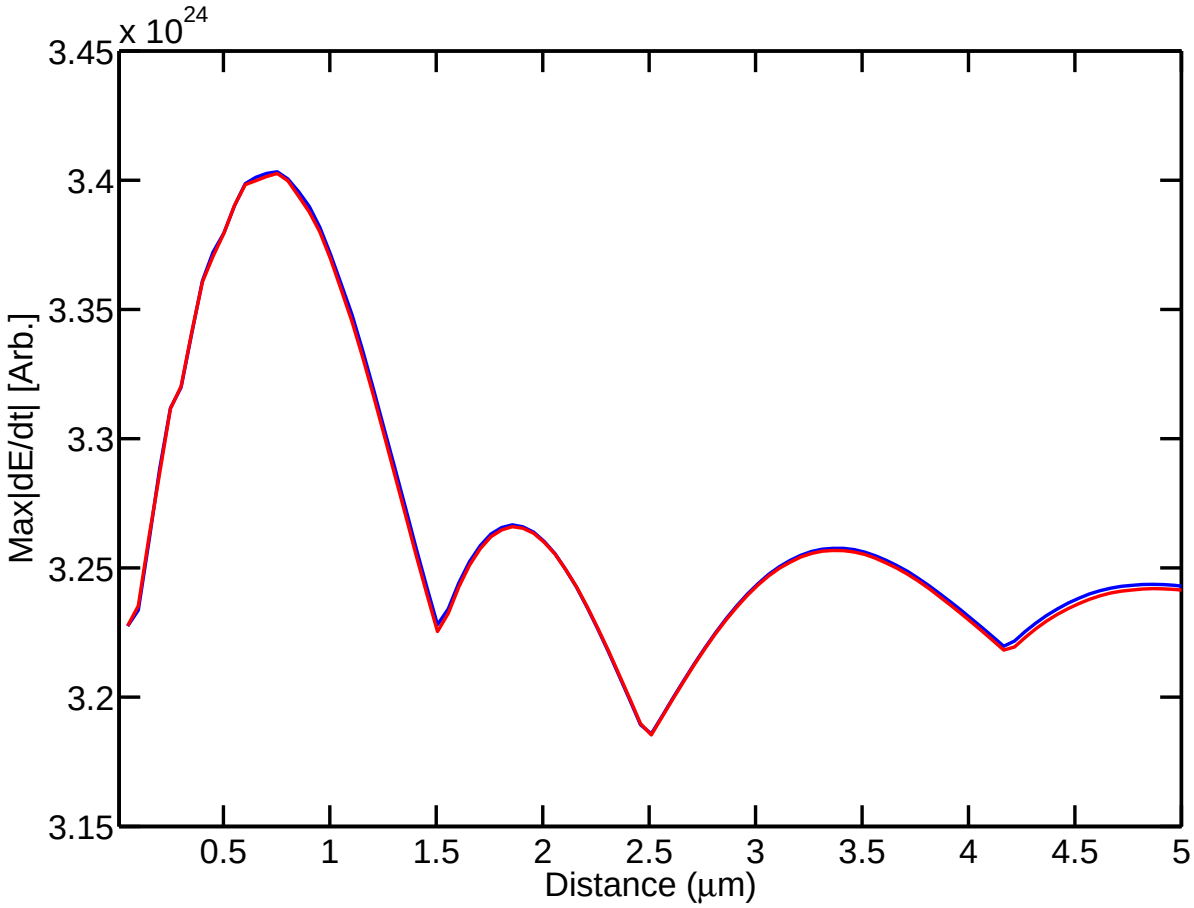

Figure 6.8: Comparison of the maximum gradient at the damage threshhold of MgO:LN as a function of distance. The blue curve includes all the harmonic content available, whereas the red curve contains only the fundamental and second harmonic. In this case, frequencies where $\omega > 2\omega_0$ have a minimal affect on the gradient because of the material dispersion.

of fused silica. This is because of fused silica's high damage threshold, high effective nonlinear strength, and flat dispersion profile (see fig. 3.3). On the other hand, MgO:LN has a higher nonlinear coefficient, but because the damage threshold is considerably lower (approximately two orders of magnitude [73]) than fused silica ($\simeq 50 \times 10^{12}$ W/cm^2 [38]), the maximum effective nonlinearity remains considerably less.

L_{shock} also depends on the frequency of the underlying carrier eq(6.7), where a higher frequency has the effect of reducing L_{shock}. In the comparison here, an 800 nm carrier was used with MgO:LN, whereas a 1240 nm carrier was used with fused silica. The combined effect of the higher carrier frequency and larger nonlinear coefficient, was not enough to achieve a steeper gradient, because of the flatter dispersion profile, and the higher damage threshold in fused silica.

The results indicate that generating extreme CWSS pulses in $\chi^{(2)}$ media is unlikely; although some success might be expected if relatively weak self-steepening is sufficient. An alternative route to achieving extreme CWSS waveforms might be through synthesis. This is done by combining a set of harmonics and using the phase offsets and amplitudes provided by our numerically generated CWSS profiles.

6.6.2 Synthesised waveforms

Another possible route to CWSS is through synthesised waveforms. This idea extends current two-colour schemes, to many, and focuses on maximising the field gradient (as opposed to the field value). To understand the process, individual harmonics were added to the fundamental field, using the phase relationships present in CWSS. Each added harmonic, increases the carrier gradient, and could perhaps be used to drive HHG if the enhancement warranted it (see section 6.7 for harmonic related yields).

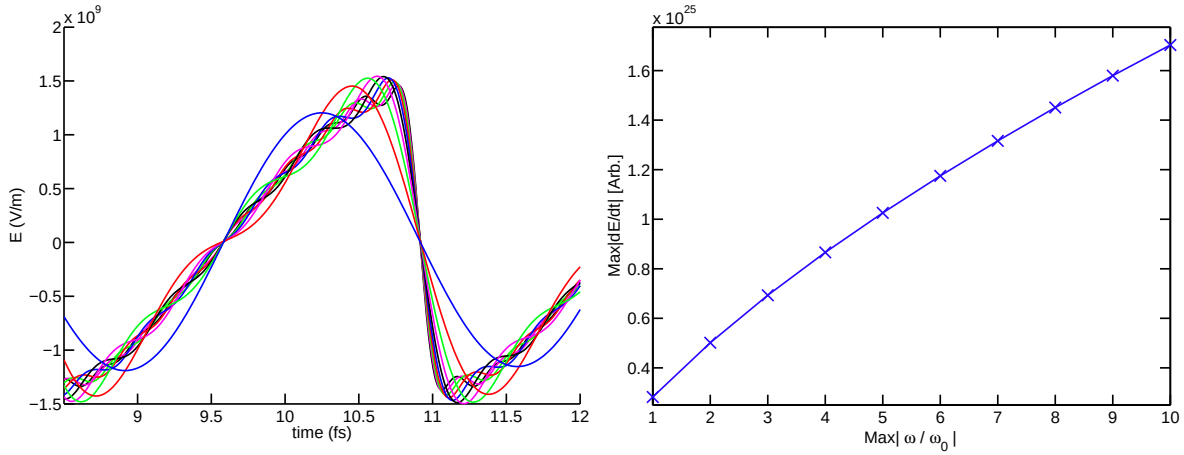

Figure 6.9: Synthesised CWSS: (left) The pulse profile begins as a sinusoid, and approaches the sawtooth shape associated with $\chi^{(2)}$ CWS as more harmonics are added. (right) Increase in maximum gradient, where each data point corresponds to the addition of an extra harmonic up to $10\omega_0$. The increase in gradient is slightly less than linear.

Fig. 6.9 shows how the most intense carrier oscillation changes with each additional harmonic. Depending on the yield that is required, a carrier with the necessary gradient might be synthesised from the individual harmonics.

6.7 HHG driven by $\chi^{(2)}$ CWSS pulses

In HHG, the intensity maxima of a strong driving laser pulse tunnel ionise an atom or molecule. Once in the continuum, the acceleration of the liberated electron is dominated by the electric field profile $E(t)$ of the pulse. Initially the electron is driven away from the core, before the electric field reverses in direction and drives it back again for a high energy recollision, approximately three-quarters of a cycle later [74]. This recollision generates an eXtreme UltraViolet (XUV) burst of radiation, localised to within a few hundred attoseconds. Since each half-cycle of the driving pulse initiates the process, a train of these XUV bursts is generated. Due to their extremely short duration, they form an ideal probe of ultrafast dynamics.

A typical HHG spectrum from an atomic gas consists of a plateau of harmonics extending to high orders, but falling off rapidly above a cut-off energy ε. For monochromatic driving fields or sufficiently long pulses, with a maximum field strength of E_0, the cut-off (ε) is related to the ionisation potential (I_P), and ponderomotive potential (U_P) of the laser field as follows: $\varepsilon = I_P + 3.17U_P$ [74, 75], where $U_P = E_0^2/(2m_e\omega_0)^2$. This equation suggests that increasing ε requires either increasing E_0, or using an atomic species with a higher I_P. However, increasing E_0 causes extra ionisation of the gas, which can result in the defocussing of the laser beam and depletion of the HHG spectrum.

Not all HHG experiments rely on monochromatic driving fields, indeed, two-colour driving field schemes have already been used [66–68]. Here a second harmonic field (E_1) is added so that $E(t) = E_0 \sin(\omega_0 t) + E_1 \sin(2\omega_0 t + \phi)$; the inversion symmetry of the driving field is thus removed. For $\phi = 0$, this means that the positive lobes of $E(t)$ are increased (giving enhanced tunnel ionisation), whilst the negative lobes are reduced (giving diminished tunnel ionisation). As a result, the XUV bursts produced have an intensity and spectral cut-off which alternate each half-cycle. This makes it easier to isolate a *single* XUV burst of high harmonic radiation from each cycle using a high band pass filter. In fact, it is possible to improve on this simple two-colour method of maximising the peak field. By changing the phase (ϕ), between a strong fundamental and weak second harmonic, increased cut-offs have been found [76]. Setting $\phi = \pi/2$ maximises the gradient, increasing the cut-off energy for every other half-cycle.

For non-monochromatic driving fields, the Strong Field Approximation (SFA) [77] can be used to predict the spectral cut-off ε. This varies for each half-cycle of the driving pulse as the maxima of the function [78]

$$\varepsilon(t_i, t_r) \;=\; I_P + \frac{1}{2}\left[eV(t_r) + p(t_i, t_r)\right]^2 \tag{6.9}$$

where t_i and t_r, are the ionisation and re collision times respectively. The asymptotic momentum of the electron, $p(t_i, t_r)$, is equal to minus the average value of the vector potential V during the electron's trajectory

$$p(t_i, t_r) \quad = \quad -e\,(t_r - t_i)^{-1} \int_{t_i}^{t_r} V(t)dt. \tag{6.10}$$

Thus it is possible to increase ε by increasing the peak vector potential $V(t_r)$, rather than increasing the peak driving field E_0. Since the gradient of the field dE/dt is the second derivative of the vector potential, a maximised gradient corresponds to a strongly peaked vector potential, and indeed the maximum value of the cut-off ε is strongly correlated to the maximum $V(t)$. For two-colour schemes, setting the relative phase to $\phi = \pi/2$ steepens the gradient by the maximum possible amount, and thus increases ε for every second half-cycle. With CWSS pulses we can improve on this, and further increase ε without suffering the disadvantages of a larger E_0. Indeed, each extra correctly phased and weighted harmonic used to build up a CWSS pulse increases the field gradient and can be seen in fig. 6.9.

Any CWSS pulse can be used to increase the field gradient, but by using $\chi^{(2)}$ CWSS pulses (as opposed to e.g. $\chi^{(3)}$ CWSS pulses), the added benefit of breaking the inversion symmetry is also derived. Because the driving E field dominates the Coulomb potential, electrons follow the form of the E field. Thus, breaking the inversion symmetry of the driving field, breaks the inversion symmetry of the HHG. Referring to section 6.4, it is clear that one half-cycle of a $\chi^{(2)}$ CWSS pulse experiences a reduction in the E field gradient. This then reduces the frequencies in the characteristic XUV burst (low ε), which can then be easily removed with a high band-pass filter. The other half-cycle of the E field, experiences an increase in maximum gradient (i.e. a maximised vector potential), and can therefore pass the filter. The maximised gradient also occurs over a shorter time period, producing a correspondingly shorter XUV burst with a smaller than average chirp. These subtelties are very useful in the generation of isolated attosecond bursts or when using attosecond pulse trains for stroboscopic imaging.

To understand the effect that additional harmonics (of the driving field) have on the HHG spectrum, a synthesised $\chi^{(2)}$ CWSS pulse was used to drive the HHG process (as in fig. 6.9). The high harmonic spectrum was then filtered at the frequency that produced the 'cleanest' attosecond pulse. This corresponds to selecting a region of the spectrum consisting of radiation emitted from a single attosecond burst. In order to isolate such an event it becomes necessary to sacrifice some of the energy in the pulse. Fig. 6.10 illustrates the reduction in FWHM and intensity of the attosecond pulses, for each extra

harmonic added to the driving field.

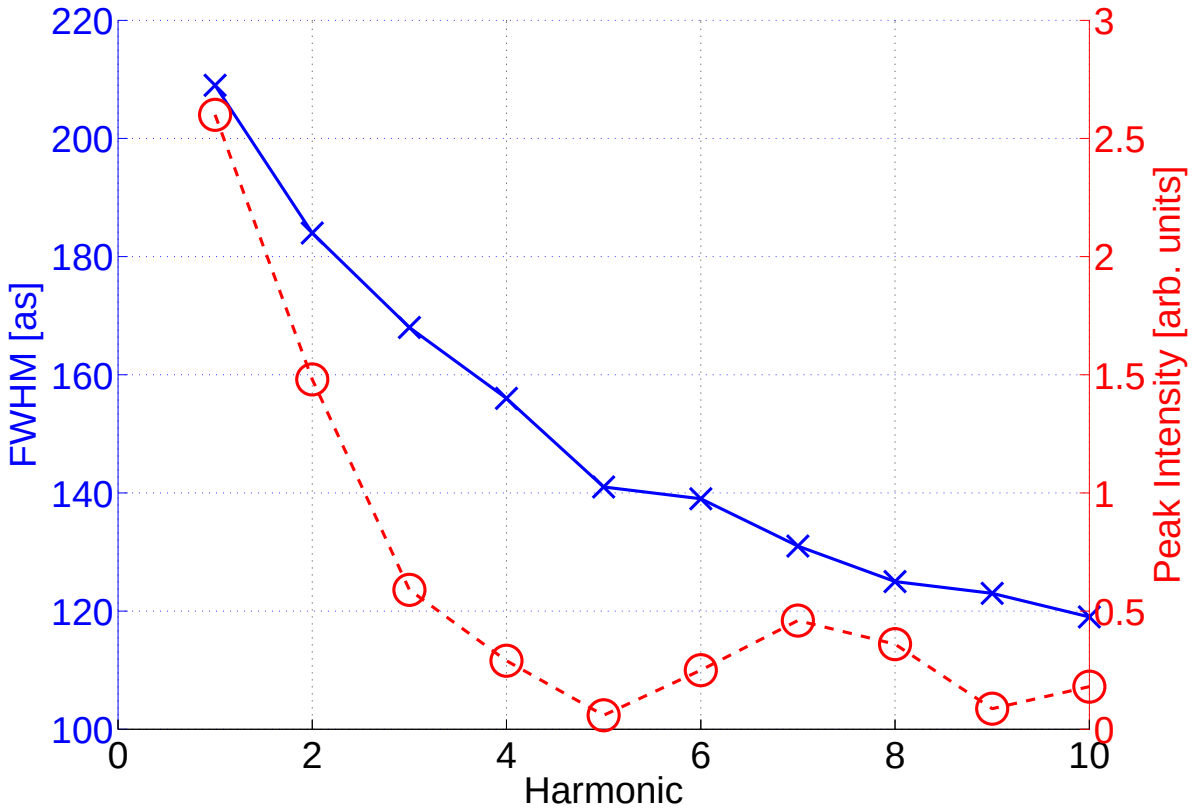

Figure 6.10: Reduction in attosecond pulse duration and intensity for additional harmonics. The attosecond duration (blue) decreases with the addition of extra harmonics to the driving field. A side effect of filtering the attosecond pulses, is a reduction in peak intensity (red). *Figure produced by L. E. Chipperfield for [41], with permission.*

6.8 Conclusion

In this chapter, the analytical predictions for shocking distance have been generalised to arbitrary nonlinear order, including combinations of the nonlinear terms. The previously neglected case of $\chi^{(2)}$ carrier wave self-steepening and shocking has been examined, and the theoretical predictions for the shocking distance are shown to be in excellent agreement with a variety of numerical integration methods. The results demonstrate a qualitative agreement with the more familiar $\chi^{(3)}$ CWS, including CEP sensitivity, and sensitivity to pulse length (in the single-cycle regime).

When generalising the theory of carrier wave shocking, an important feature emerges: at *odd* nonlinear orders, the shocked waveforms possess inversion symmetry, but lack this

symmetry at *even* orders. This lack of symmetry has great potential when used to drive HHG pulses, as it helps isolate attosecond radiation, whilst also producing attosecond events on a faster timescale. The faster timescale is a result of the rapid gradient changes in the driving field.

It is clear that producing extreme $\chi^{(2)}$ CWSS pulses in available nonlinear media remains a significant challenge. The challenge is greater than in the $\chi^{(3)}$ case, because even though $\chi^{(2)}$ nonlinear coefficients are typically greater, the damage threshold is orders of magnitude lower. Nonetheless, the breaking of the inversion symmetry makes $\chi^{(2)}$ CWSS pulses a more attractive option. A more viable route to their production, might be through synthesis. If synthesised, such pulse profiles would have some unique and very useful properties. The lack of inversion symmetry could be exploited in HHG, for stroboscopic imaging and isolation of attosecond radiation. Furthermore it would provide us with an opportunity to maximise the HHG spectral cut-off without resorting to stronger electric fields. Consequently, extending the idea of two-colour HHG driving schemes to multi-colour $\chi^{(2)}$ CWSS pulses may become an attractive option, despite its complexity, as it could ultimately lead to shorter attosecond XUV bursts.

Chapter 7

CEP Stabilisation and Measurement

7.1 Introduction

The Carrier Envelope Phase (CEP) of a few-cycle pulse has become a prominent feature of nonlinear optics in recent years. Its heightened importance is a direct result of processes becoming sensitive to the electric field of a pulse as opposed to the intensity envelope.

7.1.1 Carrier Envelope Phase

The CEP of a pulse ϕ_{CE} can be defined in the time domain as the *phase* between the pulse envelope $A(t)$, and the underlying carrier ω_0

$$E(t) = A(t)\cos(\omega_0 \mathrm{t} + \phi_{\mathrm{CE}}). \tag{7.1}$$

Fig. 7.1 shows an example of a few-cycle pulse where $\phi_{CE} = -\pi/2$. CEP sensitivity only occurs in the few-cycle regime where changes in CEP significantly influence the pulse structure, the difference becoming more pronounced the shorter the pulse duration. (Fig. 1 of chapter II illustrates this, with a plot of the 'maximum change in peak intensity' vs 'pulse duration', for fig. 7.1 this is $\simeq 2.5\%$.) Other strong field effects such as High Harmonic Generation (HHG) are also highly sensitive to CEP [78]. This is because, in the strong field regime, the electric field intensity is sufficiently high, to suppress the coulomb potential of an atom or molecule, producing optical ionisation. The tunnel ionised electrons then follow the electric field profile, making them immensly responsive to its structure. (The effect of the electric field gradient on HHG was discussed in chapter VI.)

The method of CEP measurement is fundamentally connected to mode-locked lasers and frequency combs. As discussed in chapter I, a mode-locked laser produces a train of

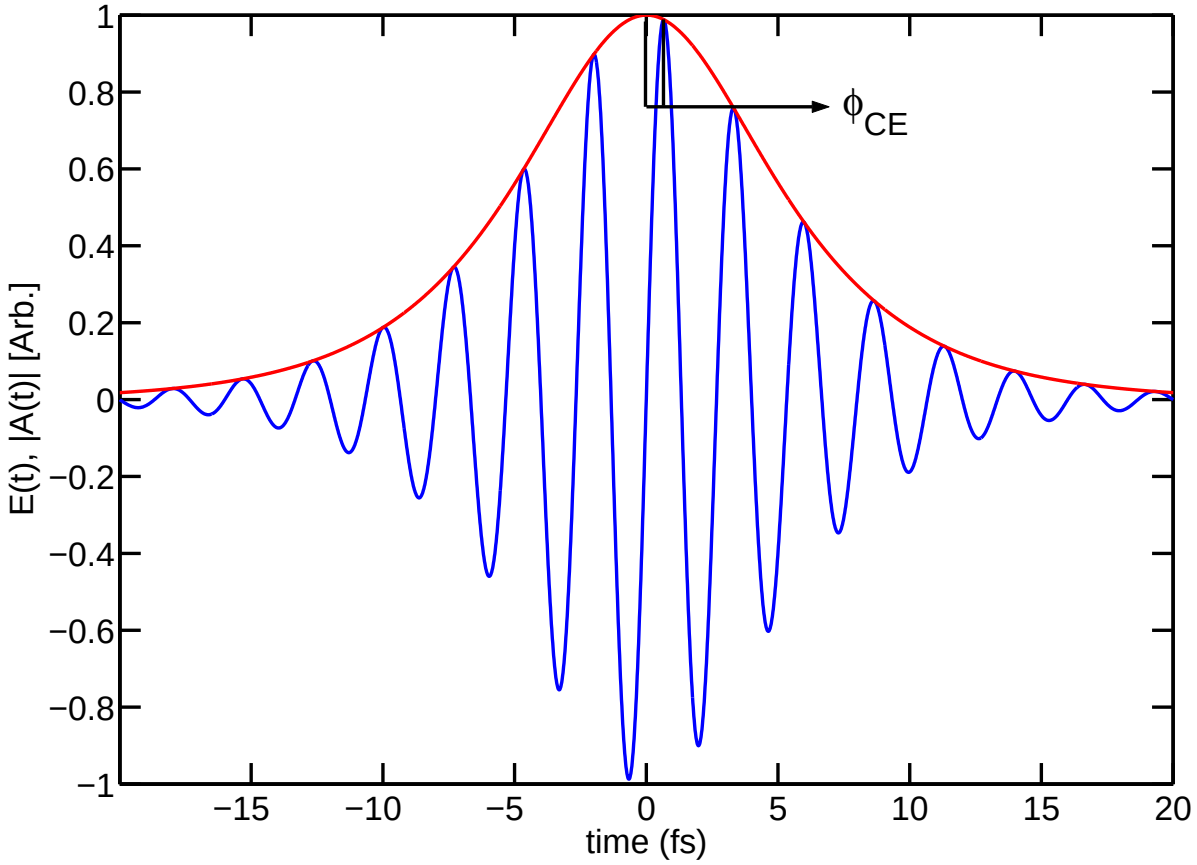

Figure 7.1: Electric field profile ($E(t)$, blue), and envelope ($|A(t)|$, red) of a 2.8 cycle, 800 nm pulse ($\simeq$ 7.5 fs) typical of a commercial Ti:sapphire laser system. In this example the absolute CEP $\phi_{CE} = -\pi/2$, and is referred to as a 'sine' pulse because of the phase of the carrier at the centre of the envelope (a 'cosine' pulse would peak in the centre). The maximum difference in peak power due to CEP corresponds to $\simeq 2.5\%$ in this case.

pulses, using the superposition of a multitude of cw (longitudinal) cavity modes. Once every round trip time, the cavity modes constructively interfere producing a pulse, where most of the energy of the EM field is present. A train of pulses in the time domain, results in an intensity spectrum made up of a frequency comb in the spectral domain (see fig. 7.2). These combs form the basis of all self-referencing techniques.

Before describing various self-referencing approaches, it is important to divide the CEP into its various components. Absolute CEP is best described as

$$\phi_{CE} = \phi_0 + \Delta\phi_{CE}, \tag{7.2}$$

where ϕ_{CE} is the absolute CEP and ϕ_0 is the unknown offset, which accumulates phase

slip on successive round-trips. [1] In the phase stabilised case ϕ_0 remains an unknown constant. $\Delta\phi_{CE}$ is the dynamic pulse-to-pulse slip adding a fixed phase to successive pulses [23, 79]. The dynamic CEP slip arises in a mode-locked laser, because of the differences in the phase v_p and group v_g velocity experienced by the circulating pulse, namely

$$\Delta\phi_{CE} = \left(\frac{1}{v_g} - \frac{1}{v_p}\right) l_c\omega_0 \quad \text{Mod}[2\pi] \tag{7.3}$$

where l_c is the round-trip cavity length. $\Delta\phi_{CE}$ is responsible for the carrier slipping beneath the envelope from pulse-to-pulse (see fig. 7.2); the slip is always modulo 2π.

7.1.2 Self-referencing

Self-referencing is one of the most successful measurement techniques of recent years, impacting on fields from coherent control to frequency metrology. The technique is best understood in the frequency domain, where a train of pulses in time, produces a spectrum consisting of an intensity comb. The tooth spacing of the intensity comb is equal to the repetition-rate of the laser f_{rep}. The dynamic pulse-to pulse slip $\Delta\phi_{CE}$, produces a shift in the frequency comb equal to the offset frequency f_O [23, 79], through the equation

$$f_O = \frac{\Delta\phi_{CE} f_{rep}}{2\pi}, \tag{7.4}$$

which is highlighted in fig. 7.2.

All self-referencing techniques, be it $0-f$, $f-2f$ or $3.5f-4f$, contain two fundamental components. They all combine the effects of a $\chi^{(2)}$ parametric interaction, with the fixed pulse-to-pulse phase slip $\Delta\phi_{CE}$. The parametric processes create frequencies with different multiples of $\Delta\phi_{CE}$, through Sum/Difference Frequency Generation ($2\Delta\phi_{CE}$ and 0 respectively), which when self-referenced to other parts of the initial spectrum display a relative phase slip of $\Delta\phi_{CE}$. The relative CEP phase slip is then detected in the form of a beat allowing a measurement of $\Delta\phi_{CE}$. (Fig. 7.10 later summarises how different parts of the spectrum experience different multiples of CEP slip.)

$f-2f$

The most widespread self-referencing technique is $f-2f$. This takes place by frequency doubling part of the initial pulse spectrum, and beating the lower wing of the second harmonic, with the upper wing of the fundamental. An octave wide spectrum is required

[1] An alternative way of writing the absolute CEP is $\phi_{CE}^{(n)} = \phi_0 + n\Delta\phi_{CE}$, where n describes the number of times the pulse has circulated in the cavity.

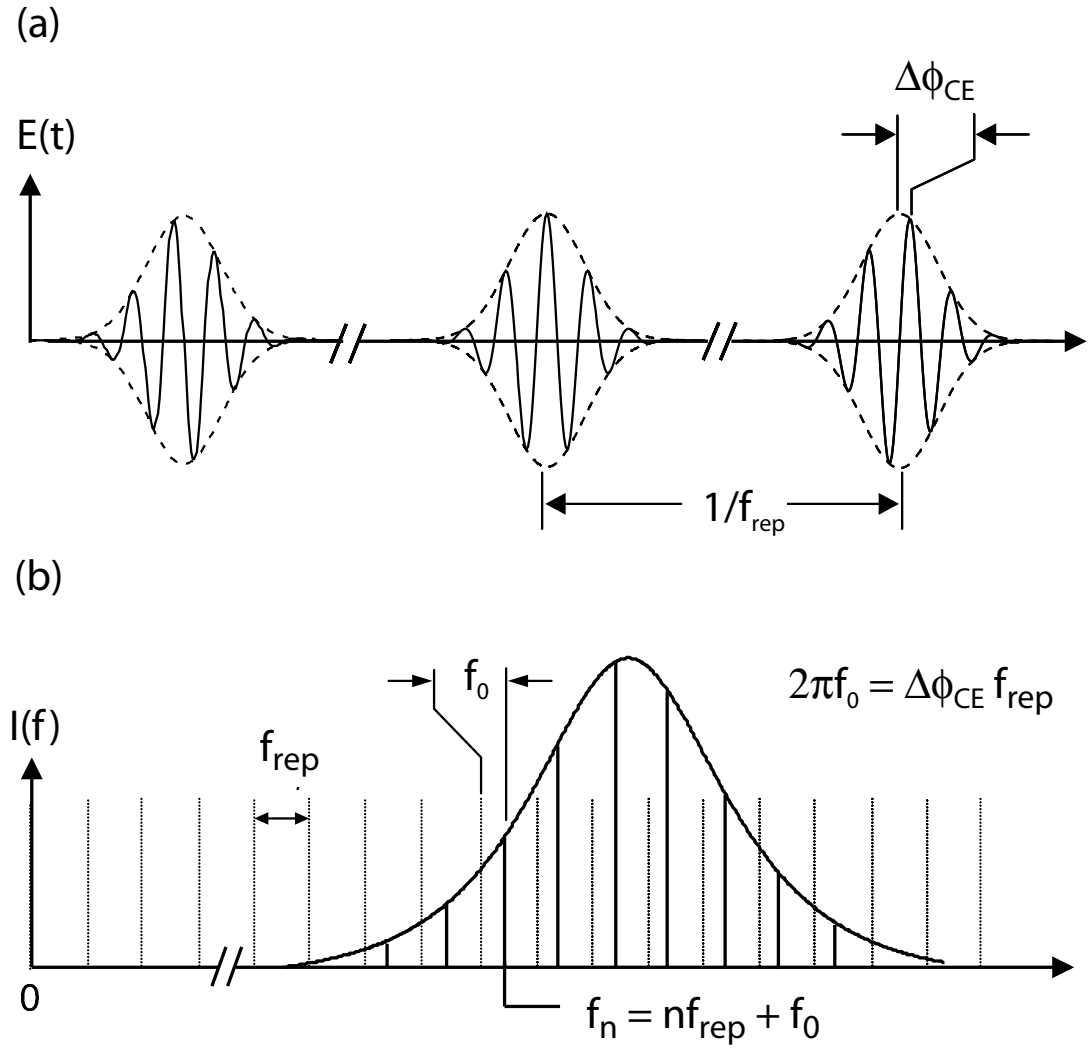

Figure 7.2: Time and spectral domain representation, where a train of pulses in time produces a frequency comb spectrum. The pulse-to-pulse CEP slip is responsible for a comb shift of f_O in the frequency domain.

for the spectral overlap, and can either be directly produced [80], or may be done with the help of a photonic crystal fiber (or some other method of broadening the fundamental spectrum to an octave). An alternative arrangement for pulses significantly less than an octave involves self-referencing other parts of the spectrum e.g. $3.5\omega_0 - 4\omega_0$ [81]. Interference then occurs in the spectral region where the teeth of the fundamental $f_n =$

$nf_{rep} + f_O$ and second harmonic $f_s = sf_{rep} + 2f_O$ interfere creating a beat at a frequency

$$f_{beat} = \pm|sf_{rep} - nf_{rep} + f_O|. \tag{7.5}$$

Here nf_{rep} and sf_{rep} correspond to the frequencies of the n/s teeth of the fundamental/second harmonic frequency combs respectively. If the photodiode response window is wide enough to include nf_{rep} and sf_{rep}, a beat at f_{beat} can be detected.

$0 - f$

In this chapter, a novel $0 - f$ self-referencing technique [42, 43], that relies on passive self-stabilisation occurring in a Periodically-Poled (PP) MgO:LN crystal, is numerically investigated. In the scheme, Difference Frequency Generation (DFG) takes place between two Quasi-Phase Matched (QPM) frequencies present in the upper (ω_3), and lower (ω_2) wings of the fundamental frequency spectrum. Any phase slip experienced by the incoming pulse ($\Delta\phi_{CE}$), is not transferred to the DFG signal, since $(\omega_3 + \Delta\phi_{CE}) - (\omega_2 + \Delta\phi_{CE}) = \omega_{pm}$ (where '$_{pm}$' refers to the quasi Phase-Matched difference frequency); see fig. 7.3. A beat between ω_1 and ω_{pm}, is then observed with the help of a photodiode (PD).

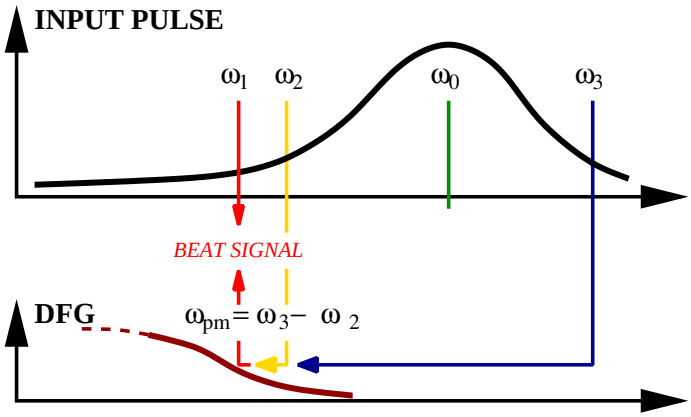

Figure 7.3: Schematic diagram of the beat between the input pulse and the DFG signal.

The beat between the phase stable ω_{pm} (in which $\Delta\phi_{CE}$ has cancelled out), and the dynamic pulse-to-pulse ω_1 (in which it hasn't), forms sidebands to the photodiode signal in a similar way to $f - 2f$. The sidebands are then used to determine f_O, which can then be incorporated in an electronic feedback loop, to change the phase and group velocity difference of eq(7.3), e.g. adjusting the pump power of the laser.

This chapter examines the nature of the $0-f$ self-referencing scheme of [42, 43], by mapping the evolution of the EM field through the crystal, and investigating the nonlinear interactions taking place. The robustness of the scheme to phase and intensity variations is also tested. On the basis of the numerical results and spectral structure observed, a novel absolute CEP measurement scheme is proposed, where the level of interference between ω_1 and ω_{pm} is used to determine ϕ_{CE} on a single-shot basis. The limitations and necessary conditions for the scheme to succeed are discussed, along with other suggestions to determine absolute CEP from the spectral domain.

7.2 Numerical model

In this section, an outline of the experiment performed in [42, 43] is provided along with some simple calculations, giving a qualitative feel of the parameters used, and the effective strength of the nonlinear interactions. This helps explain the experimental results described in [42, 43], and enables us to propose an extension of this setup to the measurement of absolute CEP.

The PSSD technique [32] was used to solve Maxwell's equations for the nonlinear propagation. Given the short interaction length, diffraction was ignored (an assumption discussed later), and in MgO:LN where the $\chi^{(2)}$ interaction is $e+e \rightarrow e$, Maxwell's equations become

$$\frac{\partial E_x}{\partial z} = -\mu_0 \frac{\partial H_y}{\partial t} \tag{7.6}$$

$$\frac{\partial H_y}{\partial z} = -\epsilon_0 \frac{\partial}{\partial t}\left[E + \chi^{(1)} * E + \chi^{(2)} E^2 + \chi^{(3)} E^3\right]. \tag{7.7}$$

Here $\chi^{(1)}$ contains linear dispersion, and any nonlinear response is assumed to be instantaneous. The crystal was periodically poled at 11.21μm, and so was optimised for DFG between the wings of the fundamental: $\omega_3(3.04\times10^{15})-\omega_2(1.885\times10^{15}) = \omega_{pm}(1.155\times10^{15})$ (rad s^{-1}). The repetition-rate of the oscillator was 70 MHz with an average power of 420 mW, producing Gaussian pulses of $\simeq$ 6 fs duration ($\lambda_0 = 830$ nm). The initial pulse was focused down to a spot size of $w_0 \simeq 15\mu$m, before propagating 2mm through the MgO:LN crystal. A mirror acting as a dichroic beam splitter was then used to reflect the fundamental, and transmit the infrared frequencies ($\lambda > 1250$ nm, $\omega < 1.51\times10^{15}$ rad s^{-1}), before the infrared part of the beam passed through a long-pass filter ($\lambda > 1400$nm, $\omega = 1.35\times10^{15}$ rad s^{-1}). The transmitted component was then detected by an InGaAs photodiode, with a rise time of 3 ns. The photodiode's spectral range was 900-1700 nm, and the response was assumed to be linear for simplicity.

For stability reasons, Orzag's 2/3 rule was implemented [59], along with a moving super-Gaussian filter to stop aliasing problems. The array size was N=16384 (2^{14}), and the Sellmeier equation for MgO:LN in [73] was used.

7.2.1 Calculation of peak intensity

Assuming a Gaussian profile in space and time, the peak intensity (I_0) can be calculated from w_0 (beam waist) and t_{FWHM} (Full-Width Half-Maximum). The intensity of E at $z = 0$, is

$$I(x, y, t) = I_0 e^{-(2ax^2+2by^2+2ct^2)} \tag{7.8}$$

where a, b and c describe the Gaussian profile and can be determined from t_{FWHM} and w_0 respectively.

$$\text{Energy[J]} = \int_{-\infty}^{+\infty}\int_{-\infty}^{+\infty}\int_{-\infty}^{+\infty} \text{I}_0[\text{W/m}^2]\text{e}^{-2\alpha\text{x}^2}\cdot\text{e}^{-2\beta\text{y}^2}\cdot\text{e}^{-2\gamma\text{t}^2}\,dx[\text{m}]\,dy[\text{m}]\,dt[\text{s}]. \tag{7.9}$$

The peak intensity can then be calculated using the standard integral ($\int_{-\infty}^{+\infty} e^{-ax^2}dx = \sqrt{\pi/a}$)

$$I_0[W/m^2] = \frac{\text{Energy[J]}}{\sqrt{\frac{\pi^3}{8\alpha\beta\gamma}}}, \tag{7.10}$$

where: average pulse energy (= average energy/rep rate) = 6×10^{-9} J, gives $I_0 \simeq 4 \times 10^{15}$ W/m^2. Using an estimate of a cylinder with diameter $w_0 = 15\mu$m and 6 fs duration, produces $I_0 = 5.65 \times 10^{15}$W/m^2, and $I_0 = 5 \times 10^{15}$W/m^2 was therefore used as the default value throughout.

7.2.2 Effective nonlinear strengths: $\chi^{(2)}E_0$ vs. $\chi^{(3)}E_0^2$

In order to appreciate the robustness of the scheme, it is instructive to consider the relative nonlinear strengths acting throughout the crystal, by normalising them to E_0.

The value of d_{33} in MgO:LN was taken to be $d_{33} = 30.0$ pm/V. Converting the units to (W/m^2) was done using

$$I[\text{W/m}^2] = \frac{1}{2}\text{nc}\epsilon_0|\text{A[V/m]}|^2 \tag{7.11}$$

where $n \simeq 2$ for bulk LN [82], and A is the intensity envelope, giving $\text{d}_{33} = 5.82\times^{-10}$

$\mathrm{m}/\sqrt{\mathrm{W}}$. $\chi_{ijk} = 2d_{ijk}$ [73], finally results in $\chi^{(2)} = 1.16 \times 10^{-9}$ $\mathrm{m}/\sqrt{\mathrm{W}}$. The value of n_2 in MgO:LN, was approximated to that of LN $\simeq 10 \times 10^{-16}$ cm^2/W [82], where applying the formula $n_2 = \frac{3\chi^{(3)}}{8n_0}$, yields $\chi^{(3)} = 5.33 \times 10^{-19}\mathrm{m}^2/\mathrm{W}$.

This produces the following normalised ratio of effective nonlinear strengths:

$$\mathrm{E}_0 \quad : \quad \chi^{(2)}\mathrm{E}_0^2 \quad : \quad \chi^{(3)}\mathrm{E}_0^3 \Longrightarrow 1 \quad : \quad 0.082 \quad : \quad 0.0027. \tag{7.12}$$

It is clear from the ratio in eq(7.12) that significant nonlinearities act throughout the propagation. Though $\frac{\chi^{(3)}E_0^2}{\chi^{(2)}E_0} \simeq 0.03$, the SPM length is $L_{SPM} = 0.26$mm, constituting a strong $\chi^{(3)}$ effect over a 2mm crystal. The presence of $\chi^{(2)}$ and $\chi^{(3)}$ enables 3 and 4-wave mixing to take place, additionally complicating the frequency mixing. We might therefore expect many frequencies to be redistributed at the end of the 2mm propagation. Fig. 7.4 plots the final spectra (log scale) of the individual and combined nonlinearities after a 2mm propagation. The initial spectrum (blue) has been distinctly changed over the propagation, where the dominant nonlinearity is $\chi^{(2)}$.

7.3 Simulation results

Analytical formulae for the conversion efficiency of a DFG signal can be found in most standard texts, and usually ignore dispersive spreading, group-velocity mismatch, and assume no field depletion [73]. When dealing with few-cycle pulses, the DFG process becomes far more complex.

Firstly, the 6 fs pulse described in [42] has a bandwidth ranging from approximately 660 to 980 nm, at -10 dB below the peak (fig. 7.4 blue), making a DFG calculation between two well defined frequencies impossible. Secondly, the assumption of no field depletion is no longer valid as the intensity at the DFG frequencies change during the propagation (fig. 7.6 shows depletion before 250 microns), due to the many 3 and 4-wave mixing process taking place. Finally, the large bandwidth means that dispersion has a much stronger effect causing pulse spreading etc.

To understand the DFG taking place and the interplay of the different nonlinearities, numerical simulations (including feedback from the author of [42]) were carried out to simulate the evolution of the EM field through the crystal. It was initially thought that ω_{pm} would steadily grow thoughout the crystal length because of QPM. However, integrating the intensity at ω_{pm}, revealed growth over the first few coherence lengths only. This can be seen in fig. 7.5.

The lack of ω_{pm} growth beyond the first 50 microns, can be explained by the relatively

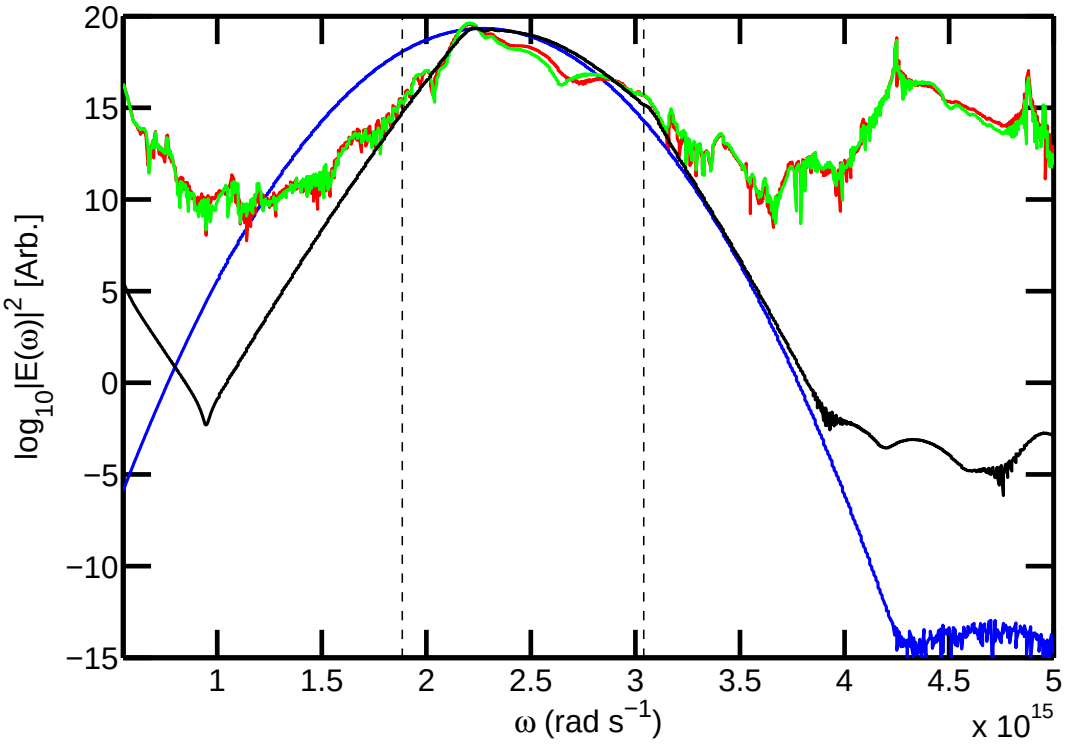

Figure 7.4: Log plot of the final intensity spectra for the following nonlinear combinations: $\chi^{(2)}$ **and** $\chi^{(3)}$ (red), $\chi^{(2)}$ only (green), and $\chi^{(3)}$ only (black). The initial spectrum (blue) is plotted for comparison. The results indicate that $\chi^{(2)}$ effects dominate $\chi^{(3)}$, which is expected from the effective nonlinear strengths. The frequencies for which the crystal is optimised/periodically poled (ω_3 and ω_2) are marked with dashed lines.

small intensity of ω_3, and the depletion at ω_2. Fig. 7.6 shows the intensity spectrum after 250 microns, where the upper wing of the fundamental (ω_3) contains a relatively small amount of energy (compared to the rest of the spectrum), whilst energy appears depleted at ω_2. The depletion of ω_2 is generally associated with Sum Frequency Generation (SFG), and indeed frequencies do appear around $\omega \simeq 4.3\omega_0$. This however was not consistent with the QPM period, which was setup to optimise DFG at ω_{pm}. The presence of strong $\chi^{(2)}$ and $\chi^{(3)}$ nonlinearities clearly makes the parametric processes taking place very complicated, where DFG and SFG both seem to occur. Small changes to the poling period ($1/10^{th}$ micron) did not significantly affect these results.

In the experiment described in [42, 43], the best beat signal detected by the PD was found using a 1400 nm ($\omega = 1.35 \times 10^{15}$) longpass filter, compared to other longer pass filters e.g. 1600 nm ($\omega = 1.18 \times 10^{15}$). This is because the optimum beat signal arises when the two interfering frequencies produce the largest PD modulation, and

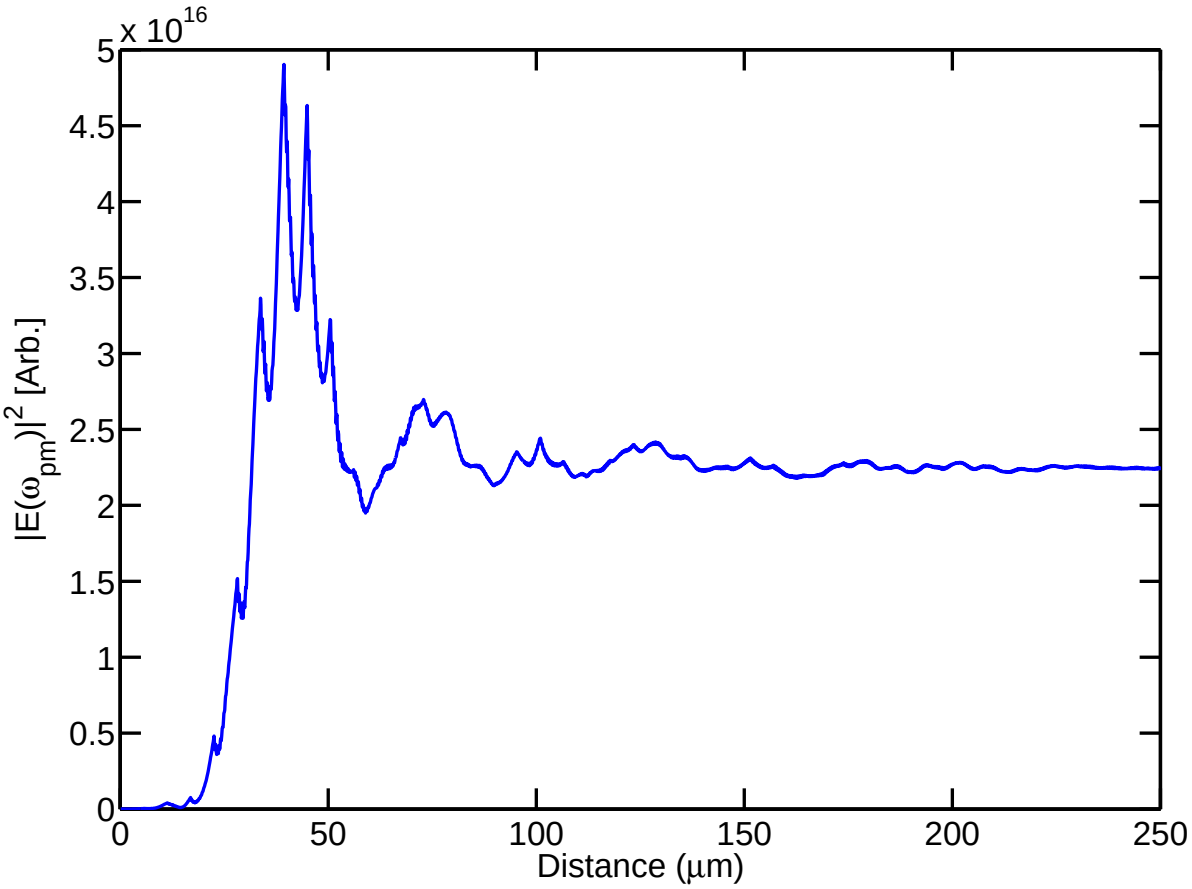

Figure 7.5: Intensity of ω_{pm} during propagation. The signal grows for approximately 50 microns before stabilising.

consequently the largest signal to noise ratio. [2] Having a disproportionate amount of energy at frequencies above or below ω_{pm} will reduce the modulation. For this reason, a good signal was detected with only a small amount of DFG, as the intensity was then comparable to ω_1 (on the lower wing of the fundamental). It is important to emphasise that a large DFG signal does not provide the best results, as a strong beat requires equally intense contributions from ω_1 and ω_{pm}. These beats are therefore found in the *tails* of the overlapping frequencies. A plane wave approximation can therefore be justified by the interaction length, being only tens of microns, diffraction is negligible.

Now that we have a handle on the nonlinear processes taking place, there are two fundamental requirements for the scheme to accurately work. The ω_{pm} signal must be insensitive to:

[2]Strictly speaking, the greatest PD modulation will depend on its frequency response and will generally be frequency dependent, but for the purposes of this study its response was considered frequency independent.

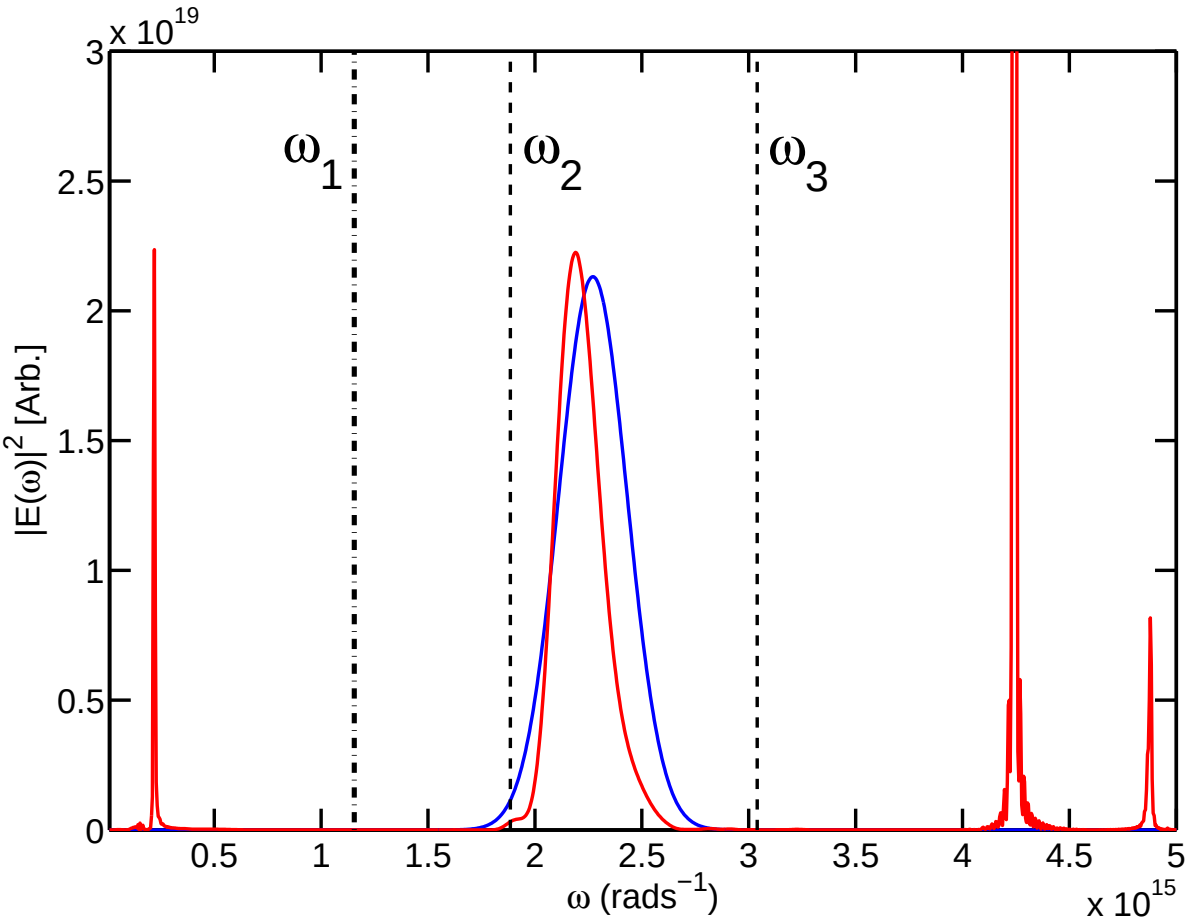

Figure 7.6: Intensity spectrum after a propagation distance of 250 microns (red). New frequencies have appeared at $\omega \simeq 0.25\omega_0$ and $\omega \simeq 4.25\omega_0$. Depletion can be seen at ω_2 compared to the initial spectrum (blue), suggesting SFG.

- $\Delta\phi_{CE}$: Pulse-to-Pulse phase slip of the input pulse.
- Intensity fluctuations of the order of $\pm 1\%$, that might occur on the incoming pulse.

The stability of the scheme to these parameters is now tested.

7.4 Self-stabilisation

The phase stability of ω_{pm} produced through DFG, to CEP slip ($\Delta\phi_{CE}$) was numerically tested. Starting from $\phi_{CE} = \phi_0 = 0$ (cosine), a pulse-to-pulse change of $\Delta\phi_{CE} = \pi/10$ was applied at the beginning of the 2mm propagation, mimicking the CEP slip from a mode-locked laser. Most of the final intensity spectrum showed little CEP sensitivity, where production of frequencies in the dc and $2\omega_0$ regions seemed unaffected. An example

of the spectral evolution during a 2mm propagation ($\Delta\phi_{CE} = 0$) can be seen in fig. 7.7. Most of the defining nonlinear activity occurs in the early parts of the propagation (up to 250 microns), creating new frequencies through parametric processes especially in the $2\omega_0$ and dc regions of the spectrum.

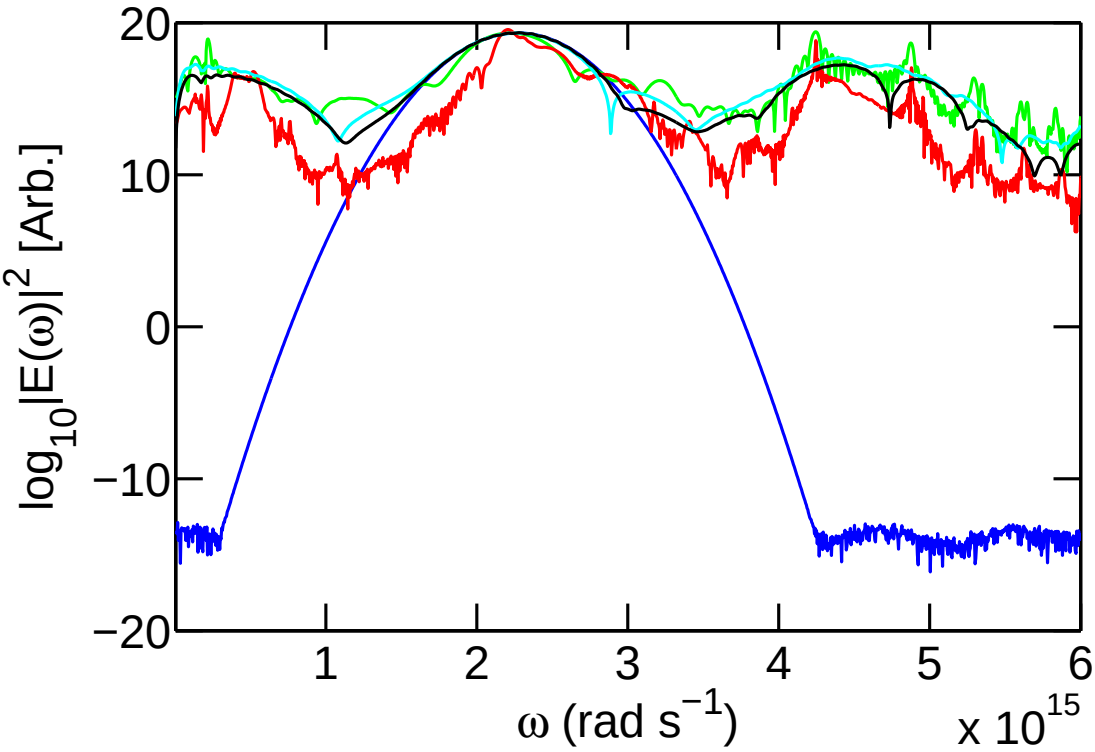

Figure 7.7: Log plot of $|E(\omega)|^2$ at various distances inside the crystal. blue=0, black=5, cyan=10, green=100 and red=2000 microns respectively. Most of the energy redistribution occurs within the first few hundred microns.

To notice the effect of CEP slip, we must look closer at the phase structure of the spectrum around ω_1. This can be done by calculating the pulse-to-pulse phase change at $E(\omega)$

$$\Delta\phi_\omega = \phi_{n+1} - \phi_n, \tag{7.13}$$

where ϕ_{n+1} and ϕ_n are the phases at a particular frequency (ω) over successive shots. The results are presented in fig. 7.8, where the self-stabilisation mechanism is clearly visible. $\Delta\phi_{CE}$ on the incoming pulse leaves the phase in the region $\omega < \omega_{pm}$ unaffected, illustrating self-stabilisation. For $\omega > \omega_{pm}$ the expected $\Delta\phi_\omega = \pi/10$ phase change due to the phase slip $\Delta\phi_{CE} = \pi/10$ is evident.

CEP slip represents a fixed pulse-to-pulse phase change that produces a frequency comparable to the repetition-rate. In the above example where $\Delta\phi_{CE} = \pi/10$, an 80MHz

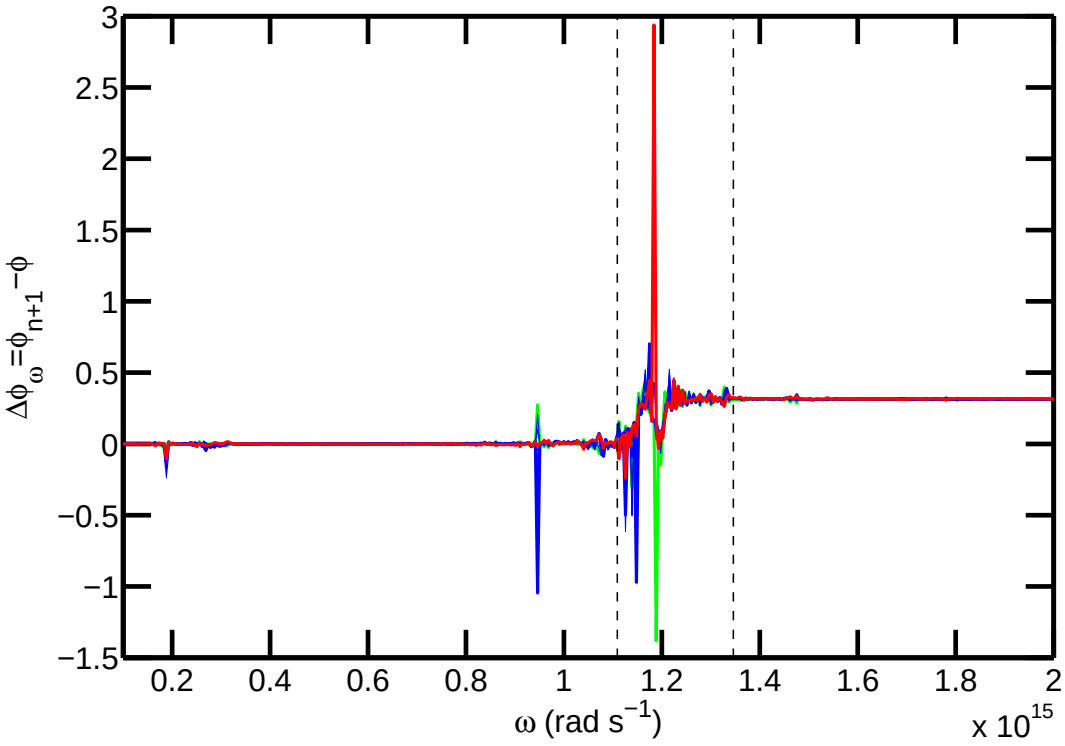

Figure 7.8: Pulse-to-pulse phase change in the final spectrum at the end of a 2mm propagation. Five plots overlay each other, representing $\Delta\phi_\omega$ between successive pulses 1-2 (red), 3-4 (blue), 5-6 (blue), 7-8 (blue), and 9-10 (green). The right hand side of the figure shows the expected $\pi/10$ phase change. The left hand side, corresponding to $\omega < \omega_{pm}$ is phase stable $\Delta\phi_\omega \simeq 0$ because of the DFG process. The 'noise' in the spectrum is the interference between ω_1 and ω_{pm}. The dashed lines, represent the spectral range of the PD including the long-pass filter.

repetition-rate would produce an offset frequency of $f_O = 4$MHz using eq(7.4). CEP stabilisation could then be achieved by changing the round-trip phase and group delay inside the laser [23], producing a train of identical pulses with an unknown offset frequency ϕ_0.

Starting from $\phi_{CE} = 0$, the PD current in a typical experiment was simulated. This can be seen in fig. 7.9, where the current has been calculated by integrating the intensity transmitted by the long-pass filter, arriving at the PD. The figure clearly shows the sinusoidal change that we would expect over a $0 - 2\pi$ range.

$0 - f$ self-referencing shares many similarities with the more well known $f - 2f$ self-referencing. In $f-2f$ schemes, intensity modulation arises between the upper wing of the fundamental where the phase is $(\phi_0 + \Delta\phi_{CE})$, and the lower wing of the second harmonic, where the phase is $2(\phi_0 + \Delta\phi_{CE})$. The two contributions are therefore always offset from

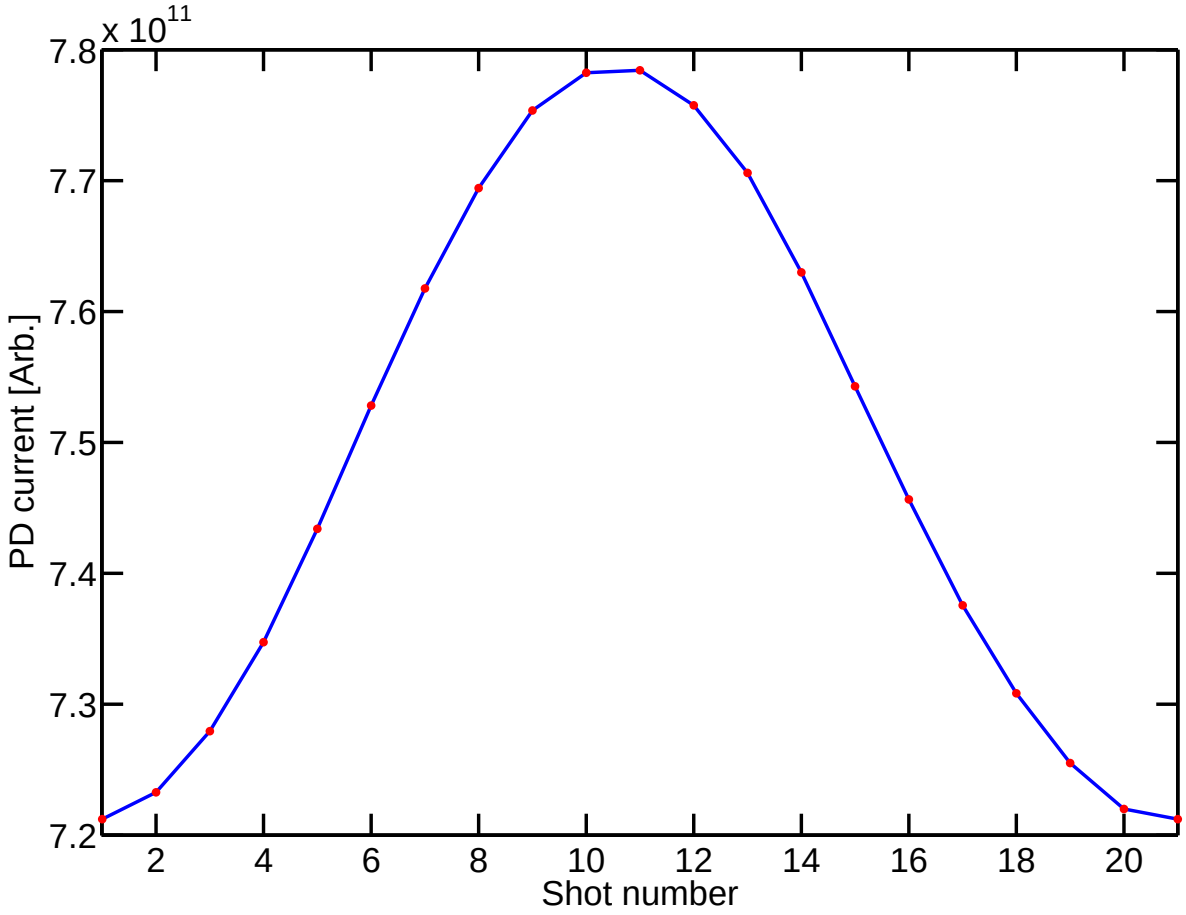

Figure 7.9: Integral of the power falling on the PD pulse-to-pulse. The frequency of the oscillation is $f_{CEO} = 4$ MHz for an 80 MHz rep-rate. ϕ_{CE} has been varied over $0 - 2\pi$.

each other by $(\phi_0 + \Delta\phi_{CE})$ thereby constructively and destructively interfering. The pulse-to-pulse phase change across the interference region $\Delta\phi_\omega$ is therefore $\Delta\phi_{CE}$ on the upper wing of the fundamental, and $2\Delta\phi_{CE}$ on the lower wing of the second harmonic.

In $0 - f$ self-referencing, ω_{pm} is passively self-stabilised to any CEP slip. This means that the pulse-to-pulse phase change in the DFG region is zero, as we have already seen in fig. 7.8. The lower wing of the fundamental (ω_1) does however experience a phase slip of $\Delta\phi_{CE}$. As in the case of $f - 2f$, a phase difference of $\Delta\phi_{CE}$ forms the boundary between these two regions.

This idea is elegantly summarised in fig. 7.10 where $\Delta\phi_\omega$ is plotted across the entire spectrum. Clearly marked 'steps' describing a relative phase offset between adjacent regions can be seen for $0 - f$, $f - 2f$, $3.5f - 4f$ etc. Placing a PD across any of these interference regions could be used to determine $\Delta\phi_{CE}$. Fig. 7.11 plots the variance of $\Delta\phi_\omega$ over successive shots, which characterises the phase stability of the spectrum. The

largest variance occurs at the points where interference takes place, as $\Delta\phi_\omega$ now contains two competing phase components.

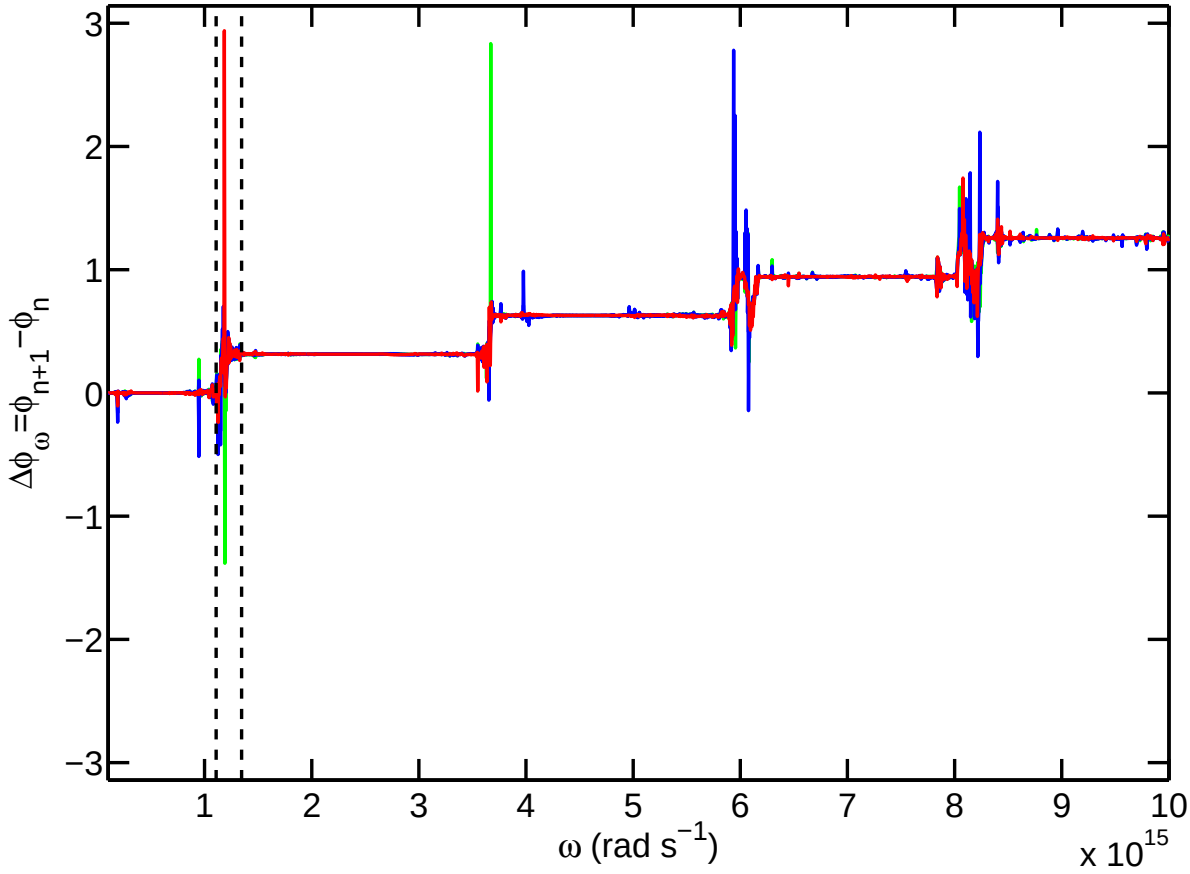

Figure 7.10: Pulse-to-pulse phase change over the entire spectrum. Five plots are present, representing $\Delta\phi_\omega$ between pulses 1-2 (red), 3-4 (blue), 5-6 (blue), 7-8 (blue), and 9-10 (green). Fixed phase differences can clearly be seen between $0-f$, $f-2f$, $3.5f-4f$ etc. The dashed lines represent the spectral range of the PD used in the $0-f$ case.

Passive self-stabilisation has been successfully used in other areas of nonlinear optics aside from self-referencing, including Optical Parametric Amplification (OPA) [83, 84], and has even been demonstrated on a single-shot basis [85].

The above results indicate that only a small amount of DFG is needed to measure $\Delta\phi_{CE}$. In fact, to achieve maximum modulation, it is essential that the contributions from ω_{pm} and ω_1 are of a similar magnitude. Though we have shown that multiple nonlinear interactions are taking place, the numerical results support the success of the scheme to CEP slip in the beat region. The sensitivity to intensity fluctuations is now investigated.

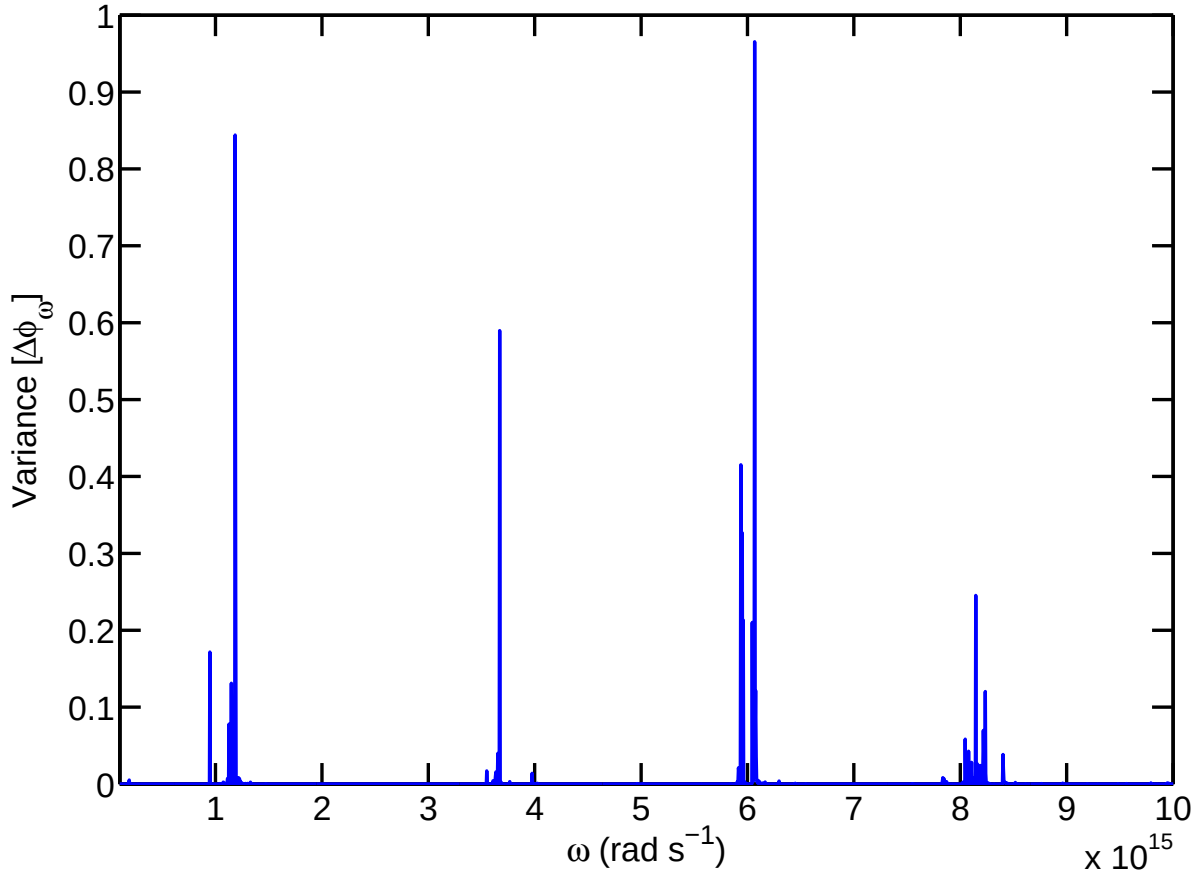

Figure 7.11: Variance of $\Delta\phi_\omega$ over 10 successive pulses. The low variance values indicate a high level of phase stability across the spectrum. The greatest values arise from the beat regions where the competing phase contributions stop the pulse-to-pulse phase change from being linear.

7.5 Intensity fluctuations

The second criterion required for accurate tracking of $\Delta\phi_{CE}$ is that $\Delta\phi_\omega$ (the pulse-to-pulse phase change at ω) be stable to small intensity fluctuations, typically $\pm 1\%$ (following private communication with the author of [42]). To model this, simulations were run with peak intensities ranging from 99% to 101% of $I_0 = 5\times10^{15}\mathrm{W/m}^2$. Changes to $\Delta\phi_\omega$ were calculated in a similar manner to the previous case (section 7.4), to see whether intensity fluctuations would distort the phase. Fig. 7.12 below shows $\Delta\phi_\omega$ for a range of intensities ($\phi_{CE} = 0$ in all cases).

Fig 7.12 illustrates how small intensity fluctuations have little effect on the phase of the spectrum in the beat region. This is because ω_3, ω_2, ω_1 and ω_{pm} are all of low intensity, therefore intensity induced phase changes are small. From the above results, it is clear that $0-f$ self-referencing is a reliable and robust technique for measuring $\Delta\phi_{CE}$,

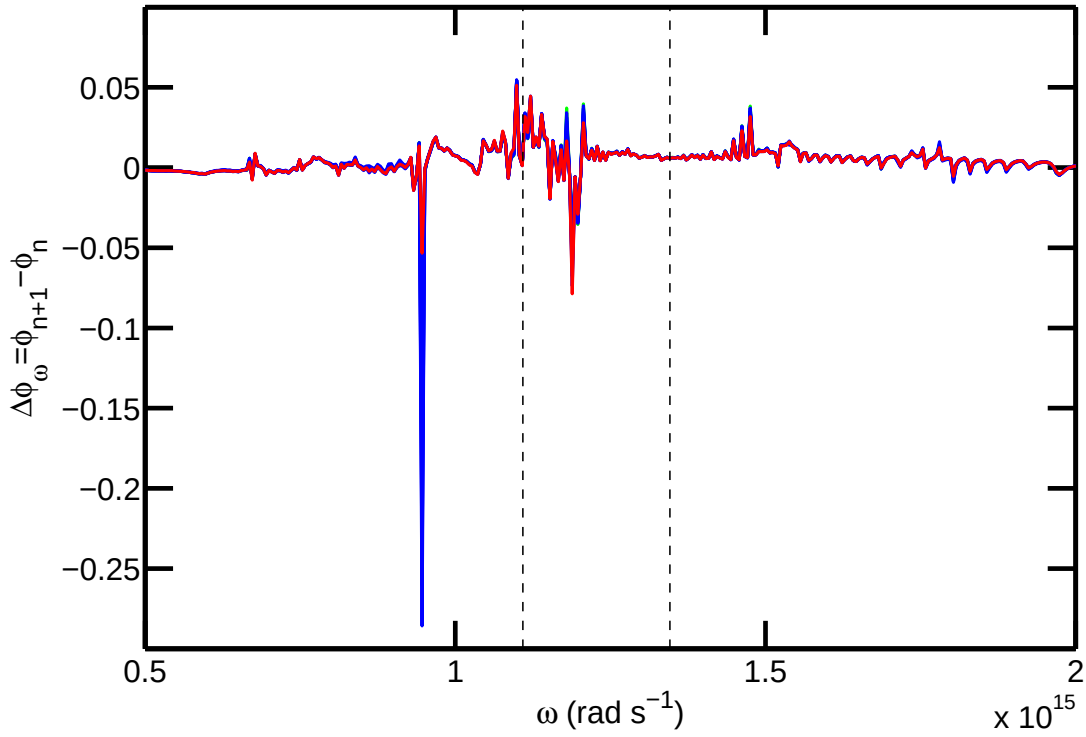

Figure 7.12: Plot of $\Delta\phi_\omega$ for intensities ranging from 99% to 101%. All pulses began with $\phi_{CE} = 0$. The red and green curves represents the lowest and highest intensities respectively and the 2% range has been divided into 10 intervals (blue). The plot shows that intensity variations of ±1% (incoming pulse), produce little phase distortion.

and has much in common with the other self-referencing methods.

7.6 Measuring the absolute CEP

Measurement of the absolute CEP has been demonstrated in a number of areas ranging from photo-ionisation [86] to high harmonic generation [78], and plasma generation [87]. Some innovative methods for single-shot CEP measurement based on spectral interference have also been suggested [88, 89]. These methods rely on CEP dependent interference occurring between various harmonics. In the case of Mehendale *et al.* [88] this involves interference between the second and third harmonics, whereas the work by Kakehata *et al.* [89] relies on interference between a delayed fundamental and its second harmonic. Both mechanisms work on the basis of a *relative* CEP dependent relationship being enforced by the nonlinearity. Though the schemes are interesting, it is not clear how sensitive their interference assumptions are to intensity fluctuations, propagation distance etc.

A new method for absolute CEP measurement based on the self-stabilisation mechanism described in section 7.1 is now proposed. The technique enables absolute CEP measurement by mapping the spectral region in the vicinity of ω_{pm}. Interference in this region is highly sensitive to ϕ_{CE}. At various distances through the crystal a clear CEP dependent structure is evident. This structure can tolerate small intensity fluctuations and may persist over distances of tens of microns. By combining a numerical model, with the detected level of interference (at the PD), a mapping can be made to an absolute CEP value. The map can be built using the crystal properties, and initial pulse characteristics (relative phase, intensity and duration), to provide a range of CEP dependent PD readings. If the map is sufficiently accurate, the PD reading can only be achieved for a given ϕ_{CE}.

7.7 Robust CEP definitions and the net-force condition

Before embarking on a description of the scheme, it is useful to review some important attributes of few-cycle pulses. Developments in ultrafast optical pulses have led to the production of half-cycle terahertz pulses [50]. In these limits, robust definitions are needed to fully characterise the pulse, as common descriptions break down or become ambiguous. The best example of this ambiguity, is the representation of a pulse with a carrier and envelope. As early as 1946 it was known that carrier envelope decompositions were not unique, within the context of radar pulses [48]. Brabec and Krausz went some way towards dealing with these issues, by suggesting a definition for the central frequency, and stating that an envelope definition is only valid, if it remains invariant under a change of phase [26].

The breakdown of many of these concepts arises from time domain definitions of the E field

$$E(t) = A(t)\cos(\omega_0 \mathrm{t} + \phi_{\mathrm{CE}}).$$

where it is often implied that a change of the CEP (ϕ_{CE}) in the time domain does not affect the fundamental pulse characteristics. However, if an envelope contains only a single-cycle, a change of phase can affect the central wavelength of the pulse, as was shown in [26]. Fig. 7.13 demonstrates how the pulse energy and central wavelength change, as the duration approaches the single-cycle limit. The fractional change in the figure is achieved by comparing a sine to a cosine pulse (an example can be seen in fig. 7.1).

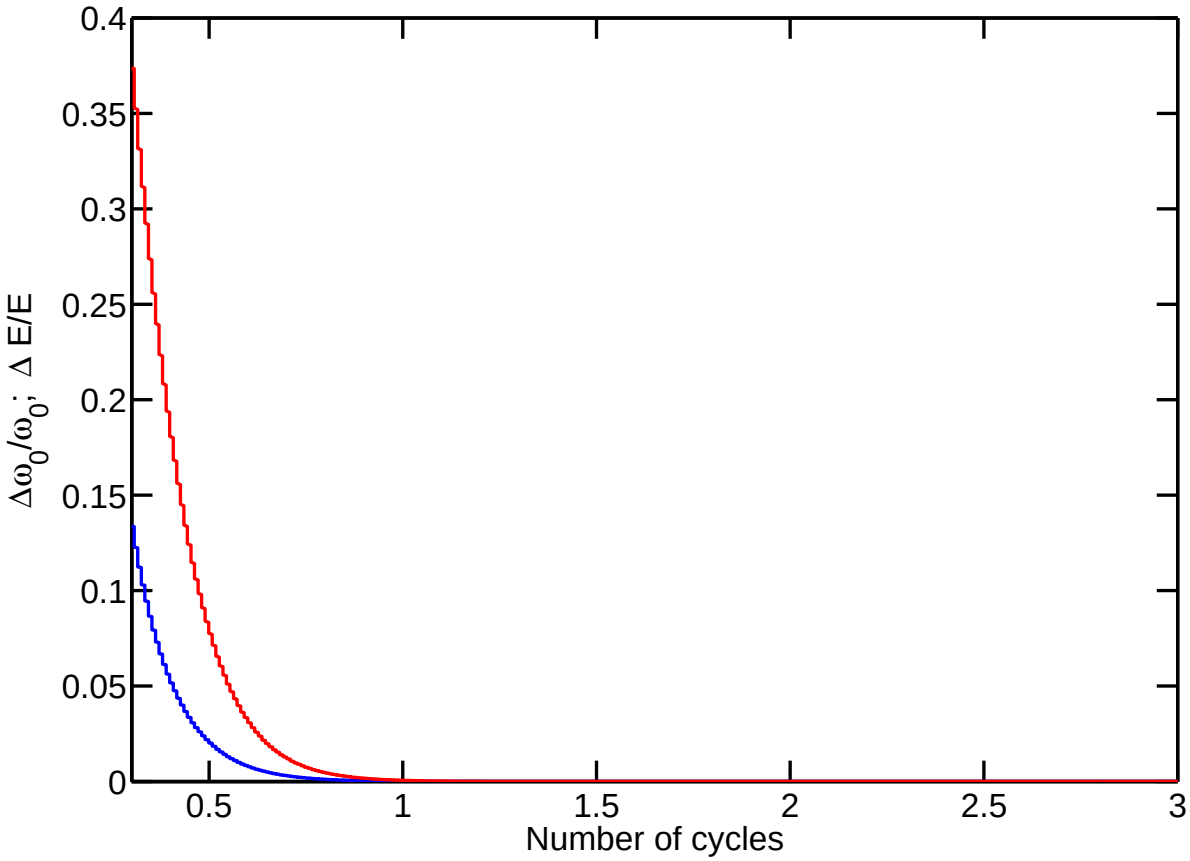

Figure 7.13: Maximum fractional change in central wavelength ω_0 (blue) and pulse energy (red). The time domain descriptions evidently break down when considering single-cycle pulses.

Another issue that is frequently neglected is that of the net-force condition. Laser pulses always satisfy the net-force condition [49], which states

$$\int_{-\infty}^{+\infty} dt \quad E(t) = -V(\infty) = 0 \tag{7.14}$$

where V is the vector potential of the laser field. Put another way, no dc component can freely propagate as part of a laser pulse. Strictly speaking, $E(t)$ should be derived from the vector potential, i.e. $E(t) = -\frac{dV(t)}{dt}$, thereby removing any dc components in the process for example eq(7.1) at the beginning of this chapter. Fortunately, the 6 fs pulse described by [42, 43] is too long for the net-force condition to have an effect (see fig. 7.14) but this would not be the case with a sub-cycle terahertz pulse. Analytical expressions exist for describing some standard pulses. For the case of a sech pulse,

$$V(t) = -V_0(t)\mathrm{sech}(\mathrm{B_3t})\sin(\omega_0\mathrm{t} + \phi_{\mathrm{CE}}) \tag{7.15}$$

goes to

$$E(t) = E_0\mathrm{sech}(\mathrm{B_3t})\cos(\omega_0\mathrm{t} + \phi_{\mathrm{CE}}) - \mathrm{V_0B_3sech(B_3t)tanh(B_3t)}\sin(\omega_0\mathrm{t} + \phi_{\mathrm{CE}}), \tag{7.16}$$

where $B_3 = \frac{\omega_0 \cosh^{-1}(2)}{\pi R}$, and R is the number of cycles (FWHM). Fig. 7.14 shows how the net-force condition is violated when using a time domain definition of the electric field which has not been derived from the vector potential. The blue curve represents the cosine pulse, where a significant dc component exists in the single/sub-cycle regime. The sine pulse automatically satisfies the net-force condition, as sine pulses contain no dc component. ('Cosine' and 'sine' pulses refer to the phase of the carrier at the centre of the envelope, see caption fig. 7.1.)

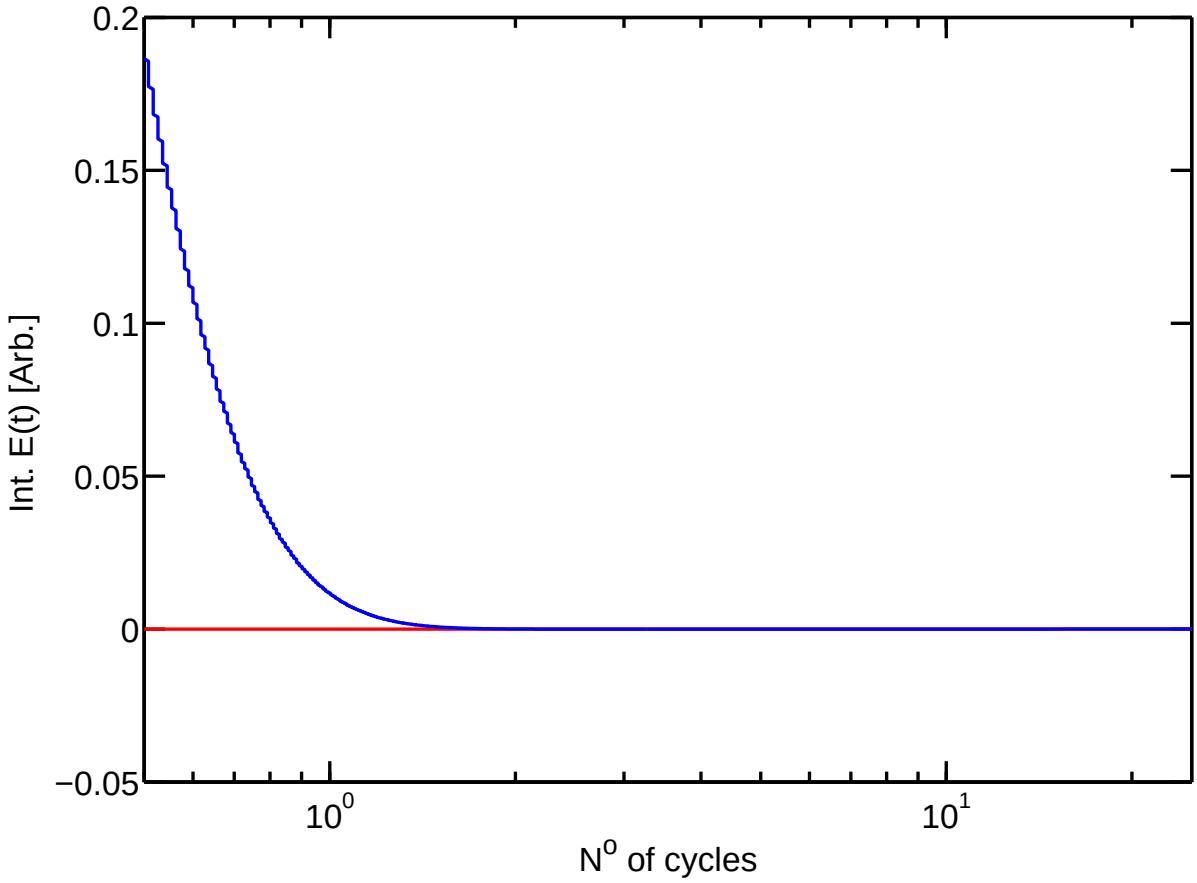

Figure 7.14: Integral of $E(t)$ for sine and cosine carriers. The cosine carrier clearly breaks the net-force condition as the pulse approaches the single-cycle regime.

If analytical expressions do not exist for the pulse in question, an alternative route begins from $V(t)$, where performing a Fourier transform, followed by a pseudo-spectral derivative, we arrive at $E(\omega)$. A central frequency can then be defined as the centre of gravity of the frequency domain (which was introduced in chapter II and in [26])

$$\omega_0 = \frac{\int_0^\infty \omega |E(\omega)|^2 d\omega}{\int_0^\infty |E(\omega)|^2 d\omega}.$$

The CEP can then be unequivocally defined in the spectral domain, as the phase of the central frequency component ω_0. Any changes to CEP can then be performed in the frequency domain, by adding a phase change to the spectrum. Fig. 7.15 compares the profiles of a pulse that satisfies the net-force condition (red), where a CEP change has been applied in the frequency domain, to one that violates it, where the phase change has been applied in time (blue). The pulse described contains $\simeq 0.56$ cycles. The time domain definition brings with it a maximum intensity difference of 4.58% (comparing a cosine pulse to a sine), and a central frequency difference of 2.21%. It is clear that a time domain description is inadequate under such circumstances.

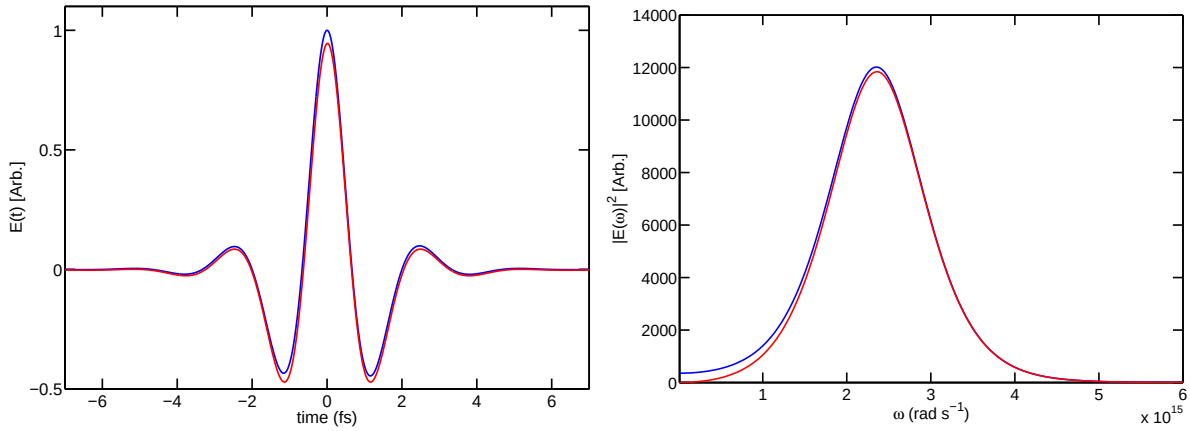

Figure 7.15: (left) Cosine pulse profile using a time domain definition (blue), and a spectral domain definition (red). The time domain definition violates the net-force condition, producing a more intense peak, and shorter wings. (right) Spectra of the above pulses (same colours), showing how the net-force condition can be observed using a spectral definition.

The advantage of deriving CEP using a spectral approach beginning from $V(t)$, is that it satisfies both the net-force condition, and the invariance of the complex envelope under a change in ϕ_{CE}. A change of phase can then be simply applied in the frequency domain, preserving the spectrum and energy of the pulse. These definitions for CEP are easily extended to sub-cycle pulses, where the concepts of carrier, envelope and phase

continue to hold.

7.8 The scheme

We now wish to determine the phase at the central frequency, using the definitions developed in section 7.7. It is possible to determine the relative spectral phases of few-cycle pulses [90] to an accuracy of 0.04 rads using the SPIDER technique [91]. The relative spectral component (with respect to the phase at ω_0) at a particular frequency is denoted $\phi_\omega(\omega)$. This means that the absolute phase of the entire pulse can be established from the absolute frequency of any single component. Taking into account the possible $\Delta\phi_{CE}$, leads to the following absolute spectral phase

$$\phi_{CE}(\omega) = \phi_0 + \phi_\omega(\omega) + \Delta\phi_{CE}. \tag{7.17}$$

The advantage of DFG over SFG is that any common unknown phases cancel each other out. In the experiment (section 7.1) we consider the two frequency components driving the DFG (ω_3 and ω_2) with the same ϕ_0 and $\Delta\phi_{CE}$. This leads to the following polarisation phase:

$$\begin{aligned} \phi_P(\omega) &= \phi_{CE}(\omega_3) - \phi_{CE}(\omega_2) \\ &= (\phi_0 + \phi_\omega(\omega_3) + \Delta\phi_{CE}) - (\phi_0 + \phi_\omega(\omega_2) + \Delta\phi_{CE}) \\ &= \phi_\omega(\omega_3) - \phi_\omega(\omega_2). \end{aligned} \tag{7.18}$$

The DFG signal (ω_{pm}) leaving the crystal is then

$$\phi'_{CE}(\omega_{pm}) = \phi_P + \delta_P, \tag{7.19}$$

where δ_P is the added phase from the integral of the polarisation during propagation. In the case of a transform limited pulse, where ω_3 and ω_2 are perfectly phase matched (or over infinitesimal distances) $\phi'_{CE}(\omega_{pm}) = \pi/2$, but in general δ_P is complicated, because of its evolution during propagation.

The phase of the pulse exiting the crystal at the DFG represents the interference between ω_1 and ω_{pm}. Assuming that the evolution of these two frequencies are independent, the evolved ω_1 component can be represented as

$$\phi'_{CE}(\omega_1) = \phi_{CE}(\omega_1) + \delta_D, \tag{7.20}$$

where δ_D represents the linear evolution of ω_1 through the crystal. The difference between $\phi'_{CE}(\omega_1)$ and $\phi'_{CE}(\omega_{pm})$ produces CEP dependent interference. Combining the final relative phase of $\phi'_{CE}(\omega_1)$ and $\phi'_{CE}(\omega_{pm})$, with knowledge of how they evolved, makes it possible (in theory) to calculate the initial relative phase offset between ω_1 and ω_{pm} at the crystal face. Because ω_{pm} is passively self-stabilised, there is only one possible initial ϕ_0 that produces a specific interference level (given knowledge of the initial pulse and crystal properties). This means that the absolute CEP of the incoming pulse can be determined.

7.9 Mapping ϕ_{CE}

In reality, the phase evolution described in section 7.8 is very complicated, and to understand it requires numerical modelling. Thus, the computational stage is crucial in determining the absolute CEP. By running a batch of simulations with different initial ϕ_{CE} values it is possible to produce an interference map because certain distances exhibit a well defined interference structure. The map then connects an initial absolute CEP, to a specific PD current value. Fig. 7.16 shows the CEP dependent structure at 50 microns for 20 cases in the range $0 < \phi_{CE} \leq \pi$. The upper (yellow) curve corresponds to $\phi_{CE} = \pi/20$, and the lower curve (bottom-right **black** +) corresponds to $\phi_{CE} = \pi$. The dotted vertical black line is the QPM frequency (ω_{pm}).

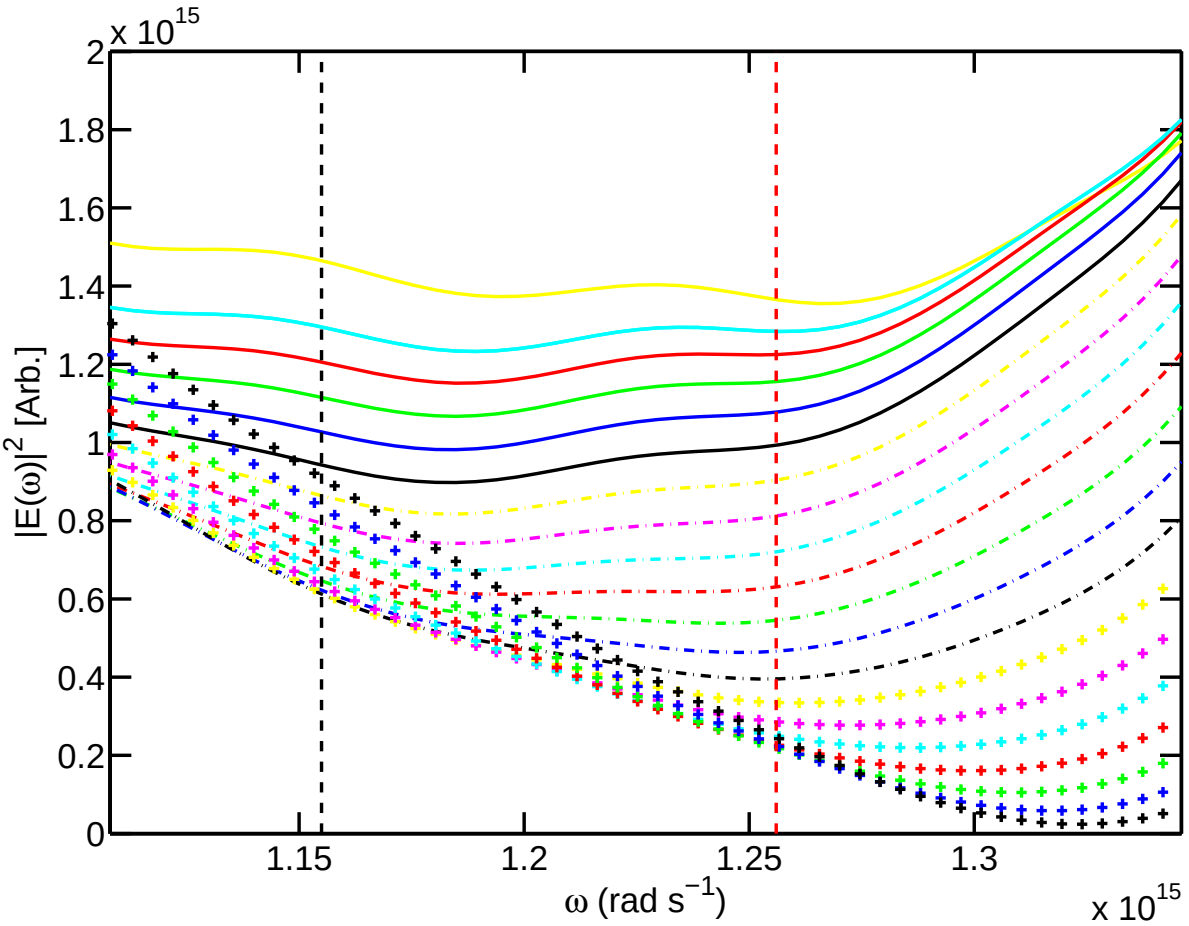

Figure 7.16: Plot of the spectral window of the PD (plus filter), after a propagation distance of 50 microns. A CEP dependent structure can clearly be seen where the lowest curve (**black** +) corresponds to $\phi_{CE} = \pi$, and the upper (yellow) curve corresponds to $\phi_{CE} = \pi/20$. The range is divided into intervals of $\pi/20$. The black dashed line is ω_{pm}, and the red dashed line has been arbitrarily chosen to demonstrate a signal consisting of only ω_1. Integrating the area under the curves, allows a PD signal to be constructed, see fig. 7.17.

The spectral window of fig. 7.16 represents the bandwidth of the PD. By integrating the areas underneath the curves it is possible to map the PD reading to a specific ϕ_{CE} value. Fig. 7.17 shows the PD reading for each of the curves (black dots). Integrating above the red-dotted line gives the expected sinusoidal form, but without any ω_{pm} contribution (red dots).

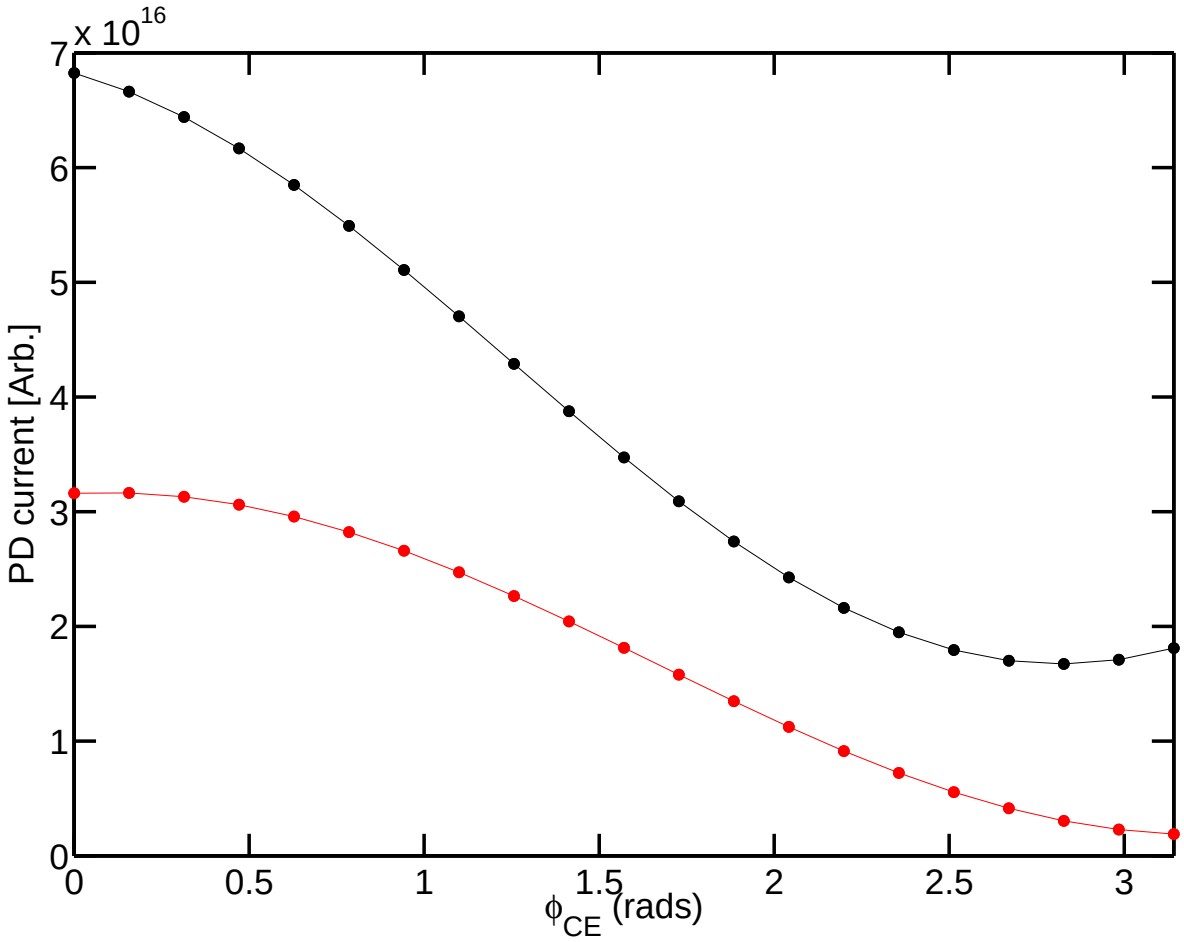

Figure 7.17: PD signal constructed from fig. 7.16. The black curve has been constructed using the entire PD spectrum, whereas the red curve has been constructed using frequencies above the dashed red line of fig. 7.16.

Necessary conditions

To ascertain absolute CEP by mapping the spectral interference the following conditions must be satisfied:

1. **Very accurate phase information.** For accurate determination of ϕ_{CE}, very precise knowledge of the initial chirp/phase is required. This ensures that ω_{pm}, ω_1 and ω_0 have a calculable phase. (SPIDER can measure the relative spectral phase of few-cycle pulses to within 0.04 rads [91].)

2. **Stable intensity.** The intensity of ω_1 and ω_{pm} must be insensitive to intensity fluctuations of the initial pulse ($\pm 1\%$ is sufficient).

3. **Necessary bandwidth.** For the process to accurately work, the pulse must have the necessary bandwidth for ω_1 to overlap with ω_{pm}, and their intensities be similar in magnitude.

4. **Crystal properties.** The crystal properties must be accurately known in order to build a reliable map. This includes the Sellmeier equation, nonlinear coefficients, crystal length etc.

5. **Computational stage.** A computational stage is needed to construct a map of the interference level to a CEP value.

To test the accuracy of the scheme to intensity fluctuations, an interference map was produced as in fig. 7.17, but for peak intensities in the range $\pm 1\%$. The linear change in intensity, produced a linear change in the intensity of ω_1 and ω_{pm}. More importantly, the interference map retained its original structure. Fig. 7.18 shows the original PD signal from fig. 7.17 (black) along with a similar reading for initial pulses $\pm 1\%$ (red 101%, green 99%). Differences due to intensity variations, are generally smaller than those produced by changing ϕ_{CE}, which is promising, considering that typical intensities can vary within that range.

Finally, the stability of the PD signal to propagation distance was measured. To confidently determine ϕ_{CE}, the PD current cannot drastically fluctuate over short distances. This would make the mapping unreliable and inaccurate. For large parts of the propagation, the change in the PD signal over distances ~ 0.1 microns, is no more than $\backsim 1\%$ of its average value. On the other hand, changing ϕ_{CE} on the original pulse produced a far greater effect. Fig. 7.19 plots the variation of the PD signal with distance for the following initial CEP values: $\phi_{CE} = 0$ (blue), $\phi_{CE} = -\pi/2$ (red), and $\phi_{CE} = -\pi$ (green). A large CEP dependent modulation is clearly exhibited at some points during the propagation (e.g. 50 microns). Thus, changes in the PD current due to propagation, can clearly be made smaller, than those due to CEP changes. This implies that an accurate map might be constructed in those regions. For maximum tolerance, a region of the crystal with a well defined interference structure, that is insensitive to small changes in intensity and propagation distance is optimum.

In theory, it is therefore possible to map a PD signal to ϕ_{CE} using numerical results. An advantage of this method is that it is possible to merely extend the use of current $0-f$ self-referencing methods. The challenge is to fix the absolute CEP to the phase of the oscillating PD signal. This technique is only accurate, if changes in the PD signal due to CEP are significantly greater than other factors that might influence the phase. If the relative phase information is available, along with accurate numerical simulations, the

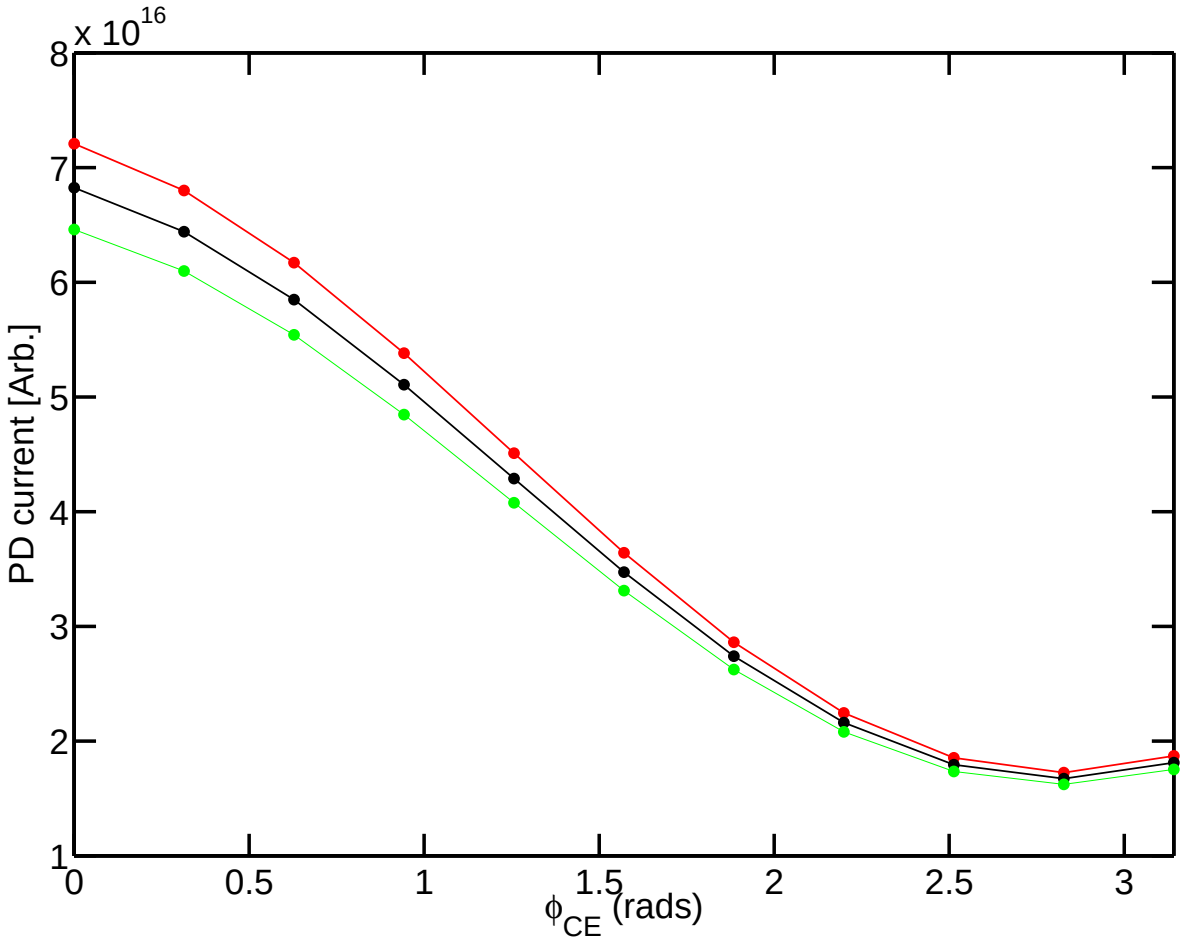

Figure 7.18: PD signal constructed for different intensities. Integrating the intensity reaching the PD, leads to a CEP varying signal. The red, black, and green plots, represent initial pulses of $101\%I_0$, $100\%I_0$ and $99\%I_0$ respectively. For $\phi_{CE} > 0.7$ rads, a change in phase produces a larger modulation than a change in intensity ($\pm 1\%$).

mapping becomes trivial. Another advantage of this method, is that it does not require strong field physics to operate, and can thus be applied to lower intensity pulses.

7.10 Conclusion

A novel $0 - f$ self-referencing scheme has been investigated. The scheme relies on a phase stable signal being passively stabilised through DFG. The signal can then be used to detect the CEP slip through self-referencing. Numerical simulations indicate that the DFG signal is stable to both intensity fluctuations ($\pm 1\%$), and CEP slip on the input pulse. A reconstructed PD signal supports the accuracy of the scheme, even when the effective nonlinearities are large. This is because the interfering regions reside in the tails

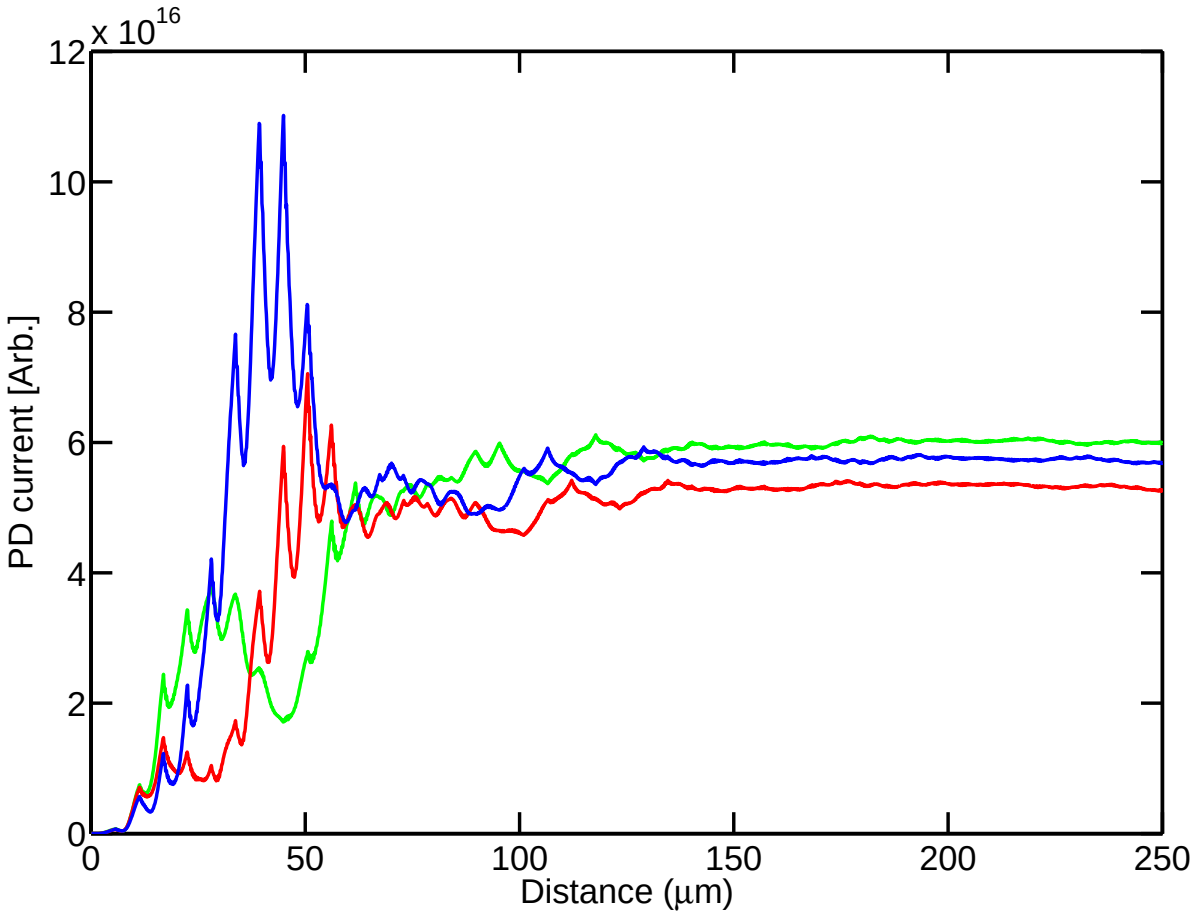

Figure 7.19: PD current during a 250 micron propagation through the crystal. The plots represent different initial ϕ_{CE} values; $\phi_{CE} = 0$ (blue), $\phi_{CE} = -\pi/2$ (red), and $\phi_{CE} = -\pi$ (green). At various distances during the propagation, large CEP dependent modulations can be seen e.g. 50 microns.

of the frequency distribution, and are thus of low intensity.

Robust definitions for sub-cycle CEP, which also obey the net-force condition, have been developed in this chapter. Deriving E from the vector potential (V) automatically satisfies the net-force condition, which is often overlooked. Powerful CEP definitions naturally arise, when defining fundamental pulse characteristics in the spectral domain. Understanding the spectral phase structure and CEP, is vital to the measurement of absolute CEP.

By extending the $0-f$ self-referencing scheme, we show that in principle it is possible to determine absolute CEP. This is because the spectral interference in the DFG region possesses an ordered structure that is sensitive to absolute CEP. The CEP dependence is considerably larger than other nonlinear effects, and crystal properties that might affect

the phase structure. By implementing computational models it is possible to map the level of interference (phase structure) to an absolute CEP value at the input crystal face. The scheme is underpinned by passive self-stabilisation, ensuring that the original DFG signal has a know phase structure produced by the relative phase of the initial pulse.

Chapter 8

General Conclusions

8.1 Modelling ultra-wideband pulses

This work has focused on the character of the ultra-wideband pulse, ranging from its history and description, to its spectral representation. Understanding the behaviour of such complex objects in nonlinear systems, requires the development of reliable and sophisticated computational models. The advances made in few-cycle pulse generation have demanded an equivalent progression in the parallel world of numerical methods, contrasting sharply with quasi-monochromatic approaches, whose underlying assumptions are now obsolete.

As pulses rapidly approach single-cycle in the visible, the interest in understanding the nature of these technological marvels is no longer a theoretical exercise, but a challenging reality. This level of detail generally requires some method of explicitly solving Maxwell's equations, which is unfortunately very computationally demanding. Pseudo-spectral methods can improve the functionality and efficiency of such calculations, but the speed-up is hardly enough to cope with multiple transverse dimensions over significant distances.

The use of *G-variables* provides one potential route through these difficulties. In the absence of interfaces, pulses tend to be uni-directional in nature. It is this aspect of their behaviour that promotes the division of the EM field into forward and backward components. By scaling the electric and magnetic fields, directional *G-variables* can be constructed, enabling a pulse to be separated into forward and backward fluxes. Accurate initial conditions combined with carefully chosen *reference parameters*, allow pulses to be described by a single PDE, making the *forward-only approximation*. This not only halves the number of equations solved, but also facilitates a moving frame transformation; it therefore has much in common with traditional envelope techniques. In short, *G-variables* provide a much needed bridge between direct Maxwell solvers and quasi-monochromatic

envelope methods.

G-variables also shed light on the magnitude of backward-propagating waves generated during nonlinear interactions. This is an important matter to consider, as these waves are routinely ignored in most numerical models because of the lack of phase-matching in the counter-propagating direction. This work justifies these common assumptions, showing that the only route to producing a noticeable backward-propagating field is through some highly unusual geometry (e.g. QPM in the backward direction). In the absence of such irregularities, backward-propagating waves can be comfortably ignored. Following this, a bandwidth unlimited envelope technique was developed, further supporting the idea that envelope techniques can describe arbitrarily large bandwidths. Indeed ultra-wideband envelope descriptions can even cope with sub-cycle phenomena, if the necessary bandwidth is allocated within the numerical model.

The phenomenon of Carrier Wave Shocking (CWS) has also been studied using a variety of numerical techniques. The process requires a vast bandwidth for its description, as extreme self-steepening forms multiple octaves in the frequency domain. Chapter V focused on understanding the CWS process, and the limitations that dispersion imposes. The distinctions between a mathematical, numerical and physical shock have been discussed, and reliable definitions that converge to analytical solutions were developed.

Chapter VI showed how CWS can be generalised to any nonlinear dispersionless medium, where the symmetry properties of the nonlinearity influence those of the propagating carrier. Thus, quadratic media break the inversion symmetry of the electric field because of their own asymmetry. Though CWS can be predicted mathematically, it does not occur in practice, as dispersion arrests the process making Carrier Wave Self-Steepening (CWSS) the closest one can approach to a shock. Applying these self-steepened profiles to a gas of atoms or molecules, may drive High Harmonic Generation (HHG) on an even faster timescale than the fundamental electric field oscillations. This is because, in HHG, the tunnel ionised electrons follow the profile of the electric field. Thus, steepened carriers constitute a faster timescale (than the fundamental carrier oscillation), and if realised would produce higher harmonic cut-offs leading to shorter attosecond pulses.

Unfortunately, the difficulty in CWSS proves to be the alignment of multiple harmonics in the presence of dispersion. Even small differences in the inter-harmonic phase-velocity significantly reduces CWSS. The only route to extreme CWSS appears to be through some form of synthesis, or multi-colour scheme.

8.2 Characterising ultra-wideband pulses

A crucial parameter in few-cycle pulses and coherent control is the Carrier Envelope Phase (CEP). The need to accurately stabilise and measure this quantity is of paramount importance, especially when probing fundamental physical processes or generating isolated attosecond pulses. Utilising the spectral methodology developed in earlier chapters, a novel $0-f$ self-referencing scheme was studied. Like other self-referencing techniques, spectral overlap can be used to measure CEP slip, and our numerical model clearly describes the process, explaining its robustness to intensity fluctuations.

By fully characterising a pulse in the frequency domain, fundamental issues, such as the net-force condition and sub-cycle CEP can be adequately addressed. To satisfy the net-force condition, the electric field should be derived from the vector potential, where the CEP can be unambiguously defined as the phase of the centre-of-gravity of the intensity spectrum. These descriptions help to convert the existing $0-f$ self-referencing method into one that can potentially determine absolute CEP.

The beat region describing the interference between the lower wing of fundamental spectrum, and the upper wing of the phase stable DFG signal, is highly CEP sensitive. By developing a numerical map based on the interefence structure of the region, it is possible to connect a photodiode reading to a unique CEP. Because CEP sensitivity is more significant than other linear and nonlinear processes taking place, the scheme appears to be practical. A photodiode reading can then be used to determine the absolute CEP of the initial pulse on entry to the crystal. Thus, low power absolute CEP measurements of ultra-wideband pulses may be possible for the first time.

8.3 Further work

Further work is possible in a number of areas that have been covered.

- The transverse G^+ model developed in chapter IV using the split-step operator method was not extensively used. Given the computational gains available from the forward-only approximation, this technique might be applied to wideband transverse problems within the paraxial limit. One potential application is filamentation. In filamentation, the self-focussing phenomenon that occurs within nonlinear optics is balanced by diffraction, and/or laser-plasma instability such as stimulated Raman or Brillouin scatter [92]. Because filamentation generally takes place over a distance of metres (in fluids), some other dispersive considerations would also need to be developed. This would further generalise the nonlinear response studied

within this thesis, to include finite nonlinear response. This generalisation would greatly increase the power and range of these numerical techniques as they could be applied to a host of new materials, further exploiting their directional and computational benefits.

- The application of carrier shaping/coherent control to HHG was investigated in chapter VI using the strong field approximation. Though two-colour schemes currently exist for maximising the harmonic cut-off, much research is also being carried out using polarisation gating techniques. Future work on light-matter interactions using the carrier gradient as a new parameter in coherent control might be investigated, as this significantly affects the HHG spectrum.

- Finally, the extension of $0-f$ self-referencing to the determination of absolute CEP, requires more extensive work. Though some details of the model have been addressed, e.g. sensitivity to intensity and crystal length, further analysis is necessary including the response of the photodiode, and the effect of chirp on the initial pulse. The temporal response of the nonlinearity might also be factored into the model, along with the tolerance of the scheme to crystal variations (e.g. Sellmeier equation, nonlinear coefficient). An important aspect of the model to consider is that of the background noise level. Thus, the scheme would have to be robust to background intensity variations in order to be feasible. Overall, such a potentially useful technique surely warrants further study.

References

[1] Maiman, T. H. *Nature* **187**, 493–494 (1960).

[2] Yariv, A. *Optical Electronics*. Holt Saunders, New York, USA, (1965).

[3] Gurs, K. and Muller, R. *Phys. Lett.* **5**, 179–181 (1963).

[4] Gurs, K. *Beats and modulation in optical ruby lasers*. New York: Columbia Univ. Press, (1964).

[5] Statz, H. and Tang, C. L. *Zeeman effect and nonlinear interactions between oscillating laser modes*. New York: Columbia Univ. Press, (1964).

[6] DiDomenico, M. *J. Appl. Phys.* **35**, 2870–2876 (1964).

[7] Hargrove, L. E., Fork, R. L., and Pollack, M. A. *Appl. Phys. Lett.* **5**, 4–5 (1964).

[8] Yariv, A. *J. Appl. Phys.* **36**, 388–391 (1965).

[9] W. E. Lamb, J. *Phys. Rev.* **134**(6A), A1429–A1450 June (1964).

[10] Mocker, H. W. and Collins, R. J. *Appl. Phys. Lett.* **7**, 270–272 (1965).

[11] DeMaria, A. J., Stetser, D. A., and Heynau, H. *Appl. Phys. Lett.* **8**, 174–176 (1966).

[12] Soffer, B. H. and Linn, J. W. *Journal Appl. Phys.* **39**, 5859–5860 (1968).

[13] French, P. M. W. *Reports on progress in physics* **58**, 169–262 (1995).

[14] New, G. H. C. *Rep. Prog. Phys.* **46**, 877–971 (1983).

[15] New, G. H. C. *Opt. Commun.* **6**, 188–192 (1972).

[16] New, G. H. C. *IEEE J. Quantum Electron* **QE-10**, 115–124 (1974).

[17] Ippen, E. P. *Appl. Phys. B.* **58**, 159–170 (1994).

[18] Fork, R. L., Greene, B. I., and Shank, C. V. *Appl. Phys. Lett.* **38**, 671 (1981).

[19] Haus, H. A. *IEEE Journal on Selected topics in Quantum Electronics* **6**, 1173–1185 (2000).

[20] Spence, D. E., Kean, P. N., and Sibbett, W. *Optics Lett.* **16**(1), 42–44 January (1991).

[21] Matsubara, E., Yamane, K., Sekikawa, T., and Yamashita, M. *J. Opt. Soc. Am. B* **24**, 985–989 (2007).

[22] Brabec, T. and Krausz, F. *Reviews of Modern Physics* **72**, 545–591 (2000).

[23] Cundiff, S. T., Ye, J., and Hall, J. L. *Rev. Sci. Instrum.* **72**, 3749–3771 (2001).

[24] T. Udem, J. R., Holzwarth, R., and Hansch, T. W. *Phys. Rev. Lett.* **82**, 3568 – 3571 (1999).

[25] Bloembergen, N. *Rev. Mod. Phys.* **71**, S283–S287 (1999).

[26] Brabec, T. and Krausz, F. *Physical Review Letters* **78**, 3282–3285 (1997).

[27] Porras, M. A. *Physical Review A* **60**(6), 5069–5073 December (1999).

[28] Blow, K. J. and Wood, D. *IEEE Journal of Quantum Electronics* **25**, 2665–2673 (1989).

[29] Kinsler, P. and New, G. H. C. *Phys. Rev. A* **67**, 0238131–8 (2003).

[30] Tafflove, A. and Hagness, S. C. *The finite-difference time-domain method.* Artech House, 2nd edition edition, (2000).

[31] Joseph, R. M. and Taflove, A. *IEEE Transactions on Antennas and Propagation* **45**, 364–482 (1997).

[32] Tyrrell, J. C. A., Kinsler, P., and New, G. H. C. *Journal Of Modern Optics* **52**(7), 973–986 May (2005).

[33] Fleck, J. A. *Phys. Rev. B* **1**, 84–100 (1970).

[34] Kinsler, P., Radnor, S. B. P., and New, G. H. C. *Phys. Rev. A* **72**, 063807 (2005).

[35] Genty, G., Kinsler, P., Kibler, B., and Dudley, J. M. *Optics Express* **15**, 5382–5387 (2007).

[36] Rosen, G. *Phys. Rev.* **139**, A539–A543 (1965).

[37] Flesch, R. G., Pushkarev, A., and Moloney, J. V. *Phys. Rev. Lett.* **76**, 2488–2491 (1996).

[38] Gilles, L., Moloney, J. V., and Vasquez, L. *Phys. Rev. E* **60**, 1051–1059 (1999).

[39] Kinsler, P., Radnor, S. B. P., Tyrrell, J. C. A., and New, G. H. C. *Phys. Rev. E* **75**, 0666031–9 (2007).

[40] Zeng, Z., Cheng, Y., Song, X., Li, R., and Xu, Z. *Phys. Rev. Lett.* **98**, 2039011–2039014 May (2007).

[41] Radnor, S. B. P., Chipperfield, L. E., Kinsler, P., and New, G. H. C. *Submitted to Phys Rev A.* (2007).

[42] Fuji, T., Rauschenberger, J., Gohle, C., Apolonski, A., Udem, T., Yakovlev, V. S., Tempea, G., Hansch, T. W., and Krausz, F. *New Journal of Physics* **7**, 116 Febuary (2005).

[43] Rauschenberger, J., Fuji, T., Hentschel, M., Verhoef, A.-J., Udem, T., Gohle, C., Hansch, T. W., and Krausz, F. *Laser Physics Letters* **3**(1), 37–42 September (2005).

[44] Radnor, S. B. P., Kinsler, P., and New, G. H. C. *In preparation* (2007).

[45] Agrawal, G. P. *Nonlinear fibre optics.* Academic Press, New York, USA, (1995).

[46] Grechin, S. G., Dmitriev, V. G., and Yurev, Y. V. *Quantum Electronics* **29**(2), 155–157 (1999).

[47] Ju, S., J., K.-Y., and Kim, H. *IEEE Microwave and Wireless Components Letters* **13**, 414–416 (2003).

[48] Gabor, D. *J. Inst. Elec. Eng. (Pt III)* **93**, 429 (1946).

[49] Milosevic, D. B., Paulus, G. G., Bauer, D., and Becker, W. *J. Phys. B: At. Mol. Opt. Phys.* **39**, R203–R262 July (2006).

[50] Bromage, J., Radic, S., Agrawal, G. P., C. R. Stroud, J., Fauchet, P. M., and Sobolewski, R. *Optics Lett.* **22**, 627–629 (1997).

[51] Kinsler, P. *arxiv.physics* **1**, 0611216 (2006).

[52] Yee, K. S. *IEEE Trans. Antennas Propagation and Propagation* **14**, 302–307 (1966).

[53] Kolesik, M., Moloney, V., J., and Mlejnek, M. *Physical Review Letters* **89**(28), 283902 December (2002).

[54] Kolesik, M. and Moloney, J. V. *Phys. Rev. E* **70**, 0366041–03660411 (2004).

[55] Sipe, J. E., Poladian, L., and de Sterke, C. M. *J. Opt. Soc. Am. A* **11**(4), 1307–1320 April (1994).

[56] de Sterke, C. M., Salinas, D. G., and Sipe, J. E. *Phys. Rev. E* **54**(2), 1969–1989 August (1996).

[57] Sanborn, J. Z., Hellings, C., and Donnelly, T. D. *J. Opt. Soc. Am. B* **20**, 152–157 (2003).

[58] Boyd, R. W. *Nonlinear Optics.* Academic Press, second edition, (1992).

[59] Press, W. H., Teukolsky, S. A., Vetterling, W. T., and Flannery, B. P. *Numerical Recipes in C.* Cambridge University Press, (1995).

[60] Siegman, A. E. *Lasers*. Oxford University Press, (1986).

[61] Demartini, F., Townes, C. H., Gustafson, T. K., and Kelly, P. L. *Phys. Rev.* **164**, 312–323 (1967).

[62] Ostrovskii, L. A. *Sov. Phys. JETP* **24**, 797 (1967).

[63] Jonek, R. J. and Landauer, R. *Phys. Lett.* **24A**, 288 (1967).

[64] Grischkowsky, D., Courtens, E., and Armstrong, J. A. *Phys. Rev. Lett.* **31**, 422 (1973).

[65] Pagendarm, H.-G. and Seitz, B. *Scientific Visualization Advanced Software Techniques*. Ellis Horwood Ltd., (1993).

[66] Pfeifer, T., Gellmann, L., Abel, M. J., Neumark, D. M., and Leone, S. R. *Optics Lett.* **31**(7), 975–977 April (2006).

[67] Liu, T. T., Kanai, T., Sekikawa, T., and Watanabe, S. *Phys. Rev. A* **73**, 0638231–8 June (2006).

[68] Oishi, Y., Kaku, M., Suda, A., Kannari, F., and Midorikawa, K. *Optics Express* **14**(16), 7230–7237 August (2006).

[69] Ilday, F. O., Beckwitt, K., Chen, Y.-F., Lim, H., and Wise, F. W. *J. Opt. Soc. Am. B* **21**(2), 376–382 Febuary (2004).

[70] Moses, J. and Wise, F. W. *Phys. Rev. Lett.* **97**, 0739031–0739034 August (2006).

[71] Moses, J. and Wise, F. W. *Optics Lett.* **31**(12), 1881–1883 June (2006).

[72] Hirlimann, C. and Morhange, J. F. *Applied Optics* **31**(17), 3263–3266 June (1992).

[73] Dmitriev, V. G., Gurzadyan, G. G., and Nikogosyan, D. N. *Handbook of Nonlinear Optical Crystals*. Springer, (1999).

[74] Schafer, K. J., Yang, B., DiMauro, L. F., and Kulander, K. C. *Phys. Rev. Lett.* **70**(11), 1599—-1602 March (1993).

[75] Krause, J. L., Schafer, K. J., and Kulander, K. C. *Phys. Rev. Lett.* **68**(24), 3535–3538 June (1992).

[76] Cao, W., Lu, P., Lan, P., Wang, X., and Yang, G. *Optics Express* **15**(2), 530–535 January (2007).

[77] Lewenstein, M., Balcou, P., Ivanov, M. Y., L'Huillier, A., and Corkum, P. B. *Phys. Rev. A* **49**(3), 2117–2132 March (1994).

[78] Haworth, C. A., Chipperfield, L. E., Robinson, J. S., Knight, P. L., Marangos, J. P., and Tisch, J. W. G. *New Journal of Physics* **3**, 52–54 (2007).

[79] Jones, D. J., Cundiff, S. T., Fortier, T. M., Hall, J. L., and Ye, J. In *Few-Cycle Laser Pulse Generation and Its Applications,* Kartner, F. X., editor, 316–342. Springer (2004).

[80] Fortier, T. M., Jones, D. J., and Cundiff, S. T. *Optics Lett.* **28**(22), 2198–2200 November (2003).

[81] Udem, T., Holzwarth, R., Zimmermann, M., Gohle, C., and Hansch, T. In *Few-Cycle Laser Pulse Generation and Its Applications,* Kartner, F. X., editor, 295–316. Springer (2004).

[82] Zheng, Z., Weiner, A. M., Parameswaran, K. R., Chou, M.-H., and Fejer, M. M. *J. Opt. Soc. Am. B* **19**(4), 839–848 August (2002).

[83] Vozzi, C., Cirmi, G., Manzoni, C., Bernedetti, E., Calegari, F., Sansone, G., Stagira, S., Svelto, O., Silvestri, S. D., Nisoli, M., and Cerullo, G. *Optics Express* **14**(21), 10109–10116 August (2006).

[84] Baltuska, A., Fuji, T., and Kobayashi, T. *Optics Lett.* **27**(14), 1241–1243 July (2002).

[85] Fang, X. and Kobayashi, T. *Optics Lett.* **29**(11), 1282–1284 June (2004).

[86] Apolonski, A., Dombi, P., Paulus, G. G., Kakehata, M., Holzwarth, R., Udem, T., Lemell, C., Torizuka, K., Burgdorfer, J., Hansch, T. W., and Krausz, F. *Phys. Rev. Lett.* **92**(7), 0739021–0739024 Febuary (2004).

[87] Kreß, M., Löffler, T., Thomson, M. D., Dörner, R., Gimpel, H., Zrost, K., Ergler, T., Moshammer, R., Morgner, U., Ullrich, J., and Roskos, H. G. *Nature* **2**(5), 327–331 (2006).

[88] Mehendale, M., Mitchell, S. A., Likforman, J.-P., Vielleneuve, D. M., and Corkum, P. B. *Optics Lett.* **25**(22), 1672–1674 November (2000).

[89] Kakehata, M., Takada, H., Kobayashi, Y., Torizuka, K., Fujihira, Y., Homma, T., and Takahashi, H. *Optics Lett.* **26**(18), 1463–1438 September (2001).

[90] Kobayashi, T., Shirakawa, A., and Fuji, T. *IEEE Journal of Quantum Electronics* **7**(4), 525–538 (2001).

[91] Anderson, M. E., de Araujo, I. E. F., Kosik, E. M., and Walmsley, I. A. *Appl. Phys. B.* **70**, S85–S93 May (2000).

[92] Schmitt, A. J. *Phys. Fluids B* **3**(1), 186–194 January (1991).